Technical Report Documentation Page

1. Report No. ABC-UTC-2016-C1-UW02-Final	2. Government Accession No.	3. Recipient's Catalog No.	
4. Title and Subtitle New Seismic-Resisting Connections for Concrete-Filled Tube Components In High-Speed Rail Systems		5. Report Date July 2020 6. Performing Organization Code	
7. Author(s) Dawn Lehman (https://orcid.org/0000-0002-0823-1167) , Charles Roeder and Muzi Zhao		8. Performing Organization Report No.	
9. Performing Organization Name and Address Department of Civil and Environmental Engineering University of Washington More Hall \Seattle WA 98195		10. Work Unit No. (TRAIS) 11. Contract or Grant No. 69A3551747121	
12. Sponsoring Organization Name and Address Accelerated Bridge Construction University Transportation Center Florida International University 10555 W. Flagler Street, EC 3680 Miami, FL 33174	US Department of Transportation Office of the Assistant Secretary for Research and Technology And Federal Highway Administration 1200 New Jersey Avenue, SE Washington, DC 201590	13. Type of Report and Period Covered Final Report (January 2018- January 2020) 14. Sponsoring Agency Code	
15. Supplementary Notes Visit www.abc-utc.fiu.edu for other ABC reports.			
16. Abstract In seismic design of transportation structures there are several competing demands that must be met: high strength and stiffness, large ductility, damage resistance and efficient construction. Prior research at the UW demonstrates that concrete-filled tubes (CFTs) can meet these competing demands. This research builds on the prior CFT research to develop connections specific for use in structural systems for high-speed rail (HSR) and other transportation system. While the FIU study focuses on the column-to-cap connection, this study will investigate a new, untested direct column-to-pile connection. This connection is critical to the structural performance and cost of the system, but few studies have focused on it, in particular for ABC. This study will advance design and construction of pile connections for HSR. The research investigated the connection for a bridge or HSR system response using advanced, nonlinear analysis methods. A thorough literature review identified types of connections and document their structural response; the UW team is working with the HSR team to identify one or more connections for further study. Using high-resolution finite element modeling, salient parameters of selected connections, including materials, geometry, and soil-structure interaction, are be studied. The results provide important initial guidelines for the connection design and seismic performance which will provide the basis for a future experimental research study to validate the work.			
17. Key Words Seismic, concrete filled steel tubes, bridges, substructures, accelerated bridge construction		18. Distribution Statement No restrictions.	
19. Security Classification Unclassified.	20. Security Classification Unclassified.	21. No. of Pages 82	22. Price

Form DOT F 1700.7 (8-72) Reproduction of completed page authorized

(this page is intentionally left blank)

NEW SESIMIC-RESISTING CONNECTIONS FOR CONCRETE-FILLED TUBE COMPONENTS IN HIGH-SPEED RAIL SYSTEMS

Final Report July 2020

Principal Investigator: Dawn Lehman

Department of Civil and Environmental Engineering
More Hall

Authors

Dawn Lehman, Charles Roeder, and Muzi Zhao

Sponsored by
Accelerated Bridge Construction University Transportation Center

ACCELERATED BRIDGE CONSTRUCTION
UNIVERSITY TRANSPORTATION CENTER

A report from
Department of Civil and Environmental Engineering
University of Washington
Box 352700, More Hall, Seattle WA 98195
https://www.ce.washington.edu

Submitted to Florida International University

DISCLAIMER

The contents of this report reflect the views of the authors, who are responsible for the facts and the accuracy of the information presented herein. This document is disseminated in the interest of information exchange. The report is funded, partially or entirely, by a grant from the U.S. Department of Transportation's University Transportation Program. However, the U.S. Government assumes no liability for the contents or use thereof.

CONTENTS

ACKNOWLEDGMENTS

This project was supported by the Accelerated Bridge Construction University Transportation Center (ABC-UTC at www.abc-utc.fiu.edu) at Florida International University (FIU), as lead institution, and Iowa State University (ISU), the University of Nevada-Reno (UNR), the University of Oklahoma, and the University of Washington as partner institutions. The authors would like to acknowledge the ABC-UTC support.

The authors would like to extend special appreciation to the ABC-UTC and the U.S. Department of Transportation Office of the Assistant Secretary for Research and Technology for funding this project.

The author would like to thank all the State DOTs that participated in the research; this work would not have been possible without their participation.

CHAPTER 1: INTRODUCTION

1.1. Project Motivation

In the seismic design of transportation structures, there are several competing demands that must be met such as high strength and stiffness, large ductility, damage resistance and efficient construction. Prior research at the UW demonstrates that concrete-filled tubes (CFTs) can meet these competing demands. For a given diameter, CFTs have larger strength and stiffness than an counterpart RC component. Testing of CFT connections demonstrates their ductility, with drift capacities larger than 8%. When used with precast components, CFTs facilitates ABC.

This research builds on the prior CFT research to develop connections specific for use in structural systems for high-speed rail (HSR). While the prior studies focused on the column-to-cap connection, this study investigated a new concept for a direct column-to-pile connection. This connection is critical to the structural performance and cost of the system, but few studies have focused on it, in particular for ABC. This study is the first phase of a multiple phase project that will advance design and construction of pile connections for transportation systems including elevated bridges and high-speed rail (HSR).

The research investigated the connection response using advanced, nonlinear analysis methods. The connection utilizes embedded reinforcement and supplemental mechanical bond mechanisms. This connection was investigated using high-resolution finite element modeling, salient parameters of selected connections, including materials, geometry, and soil-structure interaction, were studied. The results will provide important initial results for the connection design and seismic performance which will support the second phase of the project, a future experimental research study to validate the work

1.2. Research, Objectives, and Tasks

Objectives:

The overall goals of the proposed research are to investigate CFT connections and other column-to-pile connections including the seismic response and resilience, including damage, of selected CFT connections using high-resolution finite element analyses. The research was conducted to:

1. Identify experimental research to validate modeling
2. Develop guidelines for modeling RC and CFT components in LS-DYNA
3. Conduct a parametric study to evaluate impact of salient design parameters
4. Develop initial design expressions
5. Develop experimental test matrix

Scope:

The following describes the research tasks.

Task 1 – Literature Review

A comprehensive review of past experimental research was initially completed. Experimental results evaluating resistance, stiffness, and force-deflection of direct column-to-pile connections were compiled. Selected experiments were modeled for the model validation (Task 2).

Task 2 – Develop FEA modeling procedures

Using LS-DYNA, constitutive models for concrete, reinforcing steel, steel tube and the interface bond condition were investigated. Values for each of the parameters were calibrated using one set of experiments and validated using a separate set of experiments. This is described in Chapter 2 of this report.

Task 3 – Investigation of Design Parameters though Finite Element Analysis

The validated analytical model was used to conduct a parametric study. The study parameters include concrete strength, size of the reinforcing bar, diameter of the steel tube. These parameters will be studied for two types of connections. The first connection will have the reinforcement directly embedded from the reinforced concrete column to the CFT pile without any supplementary mechanical bond. The second connection used supplemental mechanical bond components in the form of a steel ring or ribs to minimize the required embedment depth. The study of the second connection investigates the geometry and placement (i.e., depth below the top of the tube). This is described in Chapter 3 of this report.

Task 4 – Design Expressions and Test Matrix

Although it is not possible to fully develop design guidelines for the connection without experimental results (this experimental program is proposed as a future task collaborative with PEER), initial design expressions were developed. These are also provided in Chapter 3 of the report as well as the conclusions.

1.3. Research Advisory Panel (RAP)

The project work was conducted in consultation with the Research Advisory Panel (RAP). The following people participated in the RAP:

- Bijan Khaleghi, WSDOT
- Amy Leland, WSDOT
- Geoff Swett, WSDOT

1.4. Report Overview

The report is presented in four chapters. This chapter is the introduction to the report. Chapter 2 describes the analytical modeling approach, including the calibration and validation. References for Chapter 2 are presented as numbers and directly follow the chapter. Chapter 3 provides the parametric study and resulting design expressions. References for Chapter 3 are presented as author name followed by publication year to differentiate them from Chapter 2. The references for Chapter 3 directly follow the chapter. Chapter 4 provides the summary, conclusions and future work.

CHAPTER 2. FINITE ELEMENT MODEL FOR RC TO CFST CONNECTIONS

2.1. Introduction

The behavior of members and connections with concrete subjected to large displacements and/or cyclic loading is complex. Large-scale experimental studies have provided important information, understanding and data but the number of study parameters and specimen sizes are limited. In bridge construction, it is common to use RC piers as ductile, energy-dissipating components and CFST as piles and drilled shafts as the deep foundation elements. To accelerate construction, there is an interest in an economical, direct connection between these two elements. Similar connections are being explored for high-rise buildings. CFST components also are being considered for use as bridge piers [1,2] and columns in buildings.

To improve the understanding and design of these components, large-scale testing has been conducted [2–4]. These tests provide valuable insight into behavior and design of components and connections, but valid analytical models are needed to better understand behavior, conduct parametric studies to develop design equations and project specific applications; this includes accurate modeling approaches for the RC members, CFST members and their connections.

Prior research has used the general-purpose finite element (FE) program ABAQUS to predict the seismic behavior of RC [5,6] and CFST members [7,8]. These ABAQUS models commonly used the concrete damage plasticity model [9,10] to simulate the behavior of concrete. Although prior research has used this approach, this model cannot simulate the pinching behavior resulting from opening and closing of cracks [8] and can result in a large residual opening cracks when unloading [11]. To mitigate these issues, prior studies have introduced explicit, discrete interfaces to simulate cracking at specified locations, such as the base of column, where large cracks are expected to occur. This method can predict the experimental response but only if the crack locations are known [12]. As such, this is not a universally applicable approach.

There have been recent advancements in the concrete models in LS-Dyna. Recent work [13] indicated that the current Winfrith model (MAT085 in LS-Dyna) can simulate crack-induced pinching behavior. The concrete damage plastic model (CDP model), denoted MAT273 in LS-Dyna [14,15], improves the prediction of the transition of tensile to compressive failure, which may occur for structural members under cyclic loading. Two other concrete models, the K&C model and CSC model, are also available in LS-Dyna with the capability to predict the mechanical behavior of concrete under complex stress states and had been evaluated [16,17] for simulation of the response of confined concrete. All four of these models were evaluated in this research.

Bond-slip behavior is critical to accurate simulation of RC, CFST and their connections. Reinforcing bars in RC is normally modeled by embedding bars into the concrete or steel bars sharing nodes with concrete elements, e.g., as used by Moon et al. [18,19], and Wang et al. [20]. This simulates perfect bond between reinforcement and concrete and ignores bond-slip. However, with perfect bond, the predicted results lead to less pinched hysteretic curves and reduced deformation [11]. Researchers have proposed bond-slip models for reinforcement-concrete interface, and one of the earliest studies modelled monotonic bond behavior of reinforcing bar in RC [21]. This model was characterized by its yield function and flow rule which consider the effect of normal stress as well as the shear dilation caused by ribs of

reinforcing bar. Another interface model for FE analysis simulated the cyclic behavior of bar-concrete interface with an iterative algorithm based on monotonic and cyclic pull-out tests [22,23]. Other researchers [24,25] developed bond-slip models to account for the influence of damage in the surrounding concrete. A bond-slip model that provides simple expressions to reasonably predict the monotonic and cyclic behavior of bar-concrete interface have also been developed [11,26], and damage of concrete, cross-section contraction of reinforcing bar and cyclic deterioration of bond were all considered. This report adopted this model due to ease of application and comprehensive approach [11,26].

Bond slip between the steel tube and concrete fill of CFST has been studied [e.g.,18, 27–29], and this behavior is normally modeled as Coulomb friction:

$$F_{\mathrm{f}} \leq \mu F_{\mathrm{n}} \tag{2.1}$$

where F_{f} is the interface force, F_{n} is the force normal to the interface and μ is the coefficient of friction, which has been between 0.3 and 0.6 [18,30–32]. However, bond-slip behavior in CFST members is not always accurately predicted using this method. Spiral-weld tubes develop mechanical bond at the welds and all tubes develop binding action that can increase the bond between concrete core and steel tube. As such, a more accurate approach to model the bond-slip behavior in CFST is required.

This report uses the commercially available LS-Dyna nonlinear analysis program to overcome the challenges observed in prior studies and develop modeling recommendations to accurately simulate the seismic behavior of RC and CFST members and connections. The research used three large-scale, well-vetted experiments to determine the modeling parameters: RC column tests [33], CFST component and connection tests [3] and CFST to RC direct connection tests [4]. For each specimen, the approach is as follows. First, the four previously discussed concrete models were initially evaluated. Next, the element type for concrete was evaluated, and the mesh size and aspect ratio of the concrete element were considered. Then, a full model is developed with bond-slip models for both the tube and the reinforcing steel. The values for the modeling parameters were determined by comparing predictions to the experimental results. Finally, the proposed modeling approach was verified using other test data, RC column tests [34] and embedded column base connection for CFST conducted by [35]. The comparison included force-displacement response data, observed yielding, concrete damage. A summary table of the recommended modeling parameters and element types is provided.

2.2. Concrete constitutive model

LS-Dyna has a number of models to simulate the mechanical behavior of concrete, four concrete constitutive models are most commonly used for structural analysis [20,36,37] (material designations used in LS-Dyna are given in parentheses): K&C model (MAT072R3), Winfrith model (MAT085), CSC model (MAT159) and a concrete damage plasticity model or CDP model (MAT273). The predictions of these four concrete models are compared to the cyclic curves of axially loaded, unconfined plain concrete specimens in the previous studies, shown in Fig. 2.1 [38–40]. In this figure, positive stress means tension, and negative stress means compression.

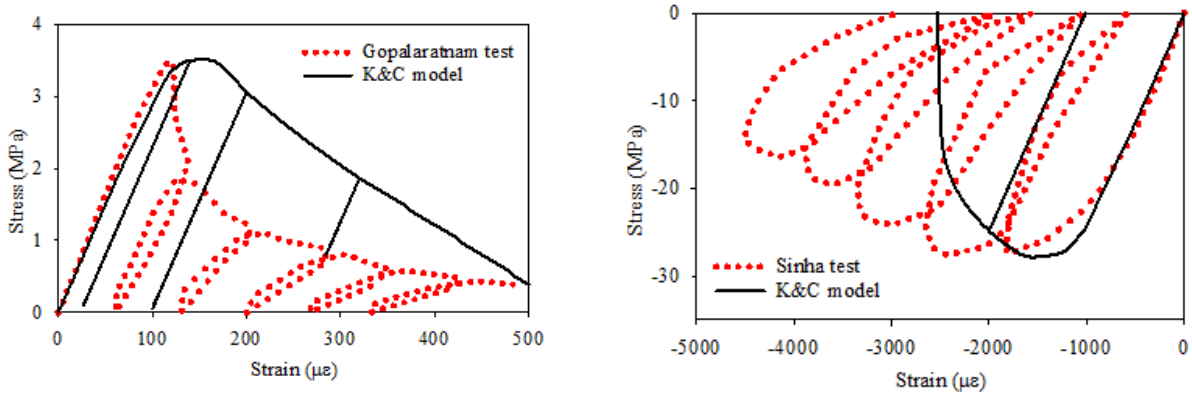

(a) K&C model

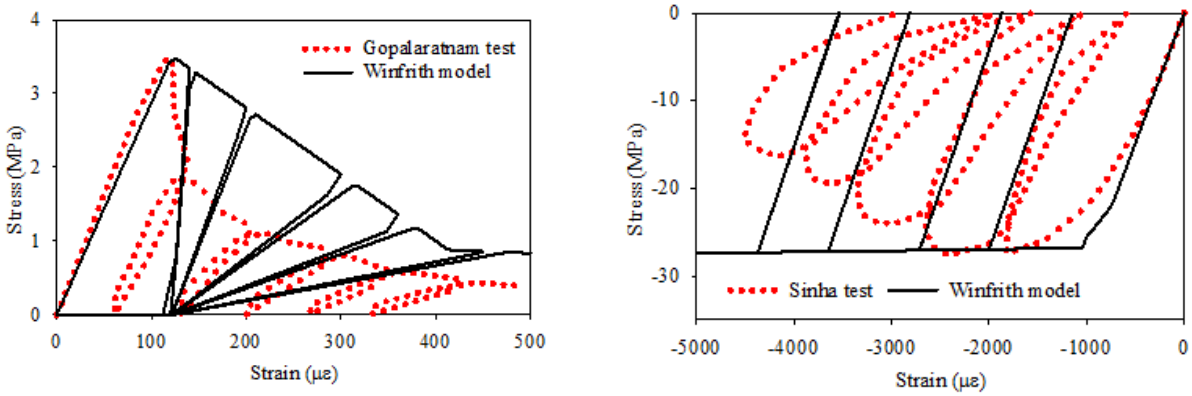

(b) Winfrith model

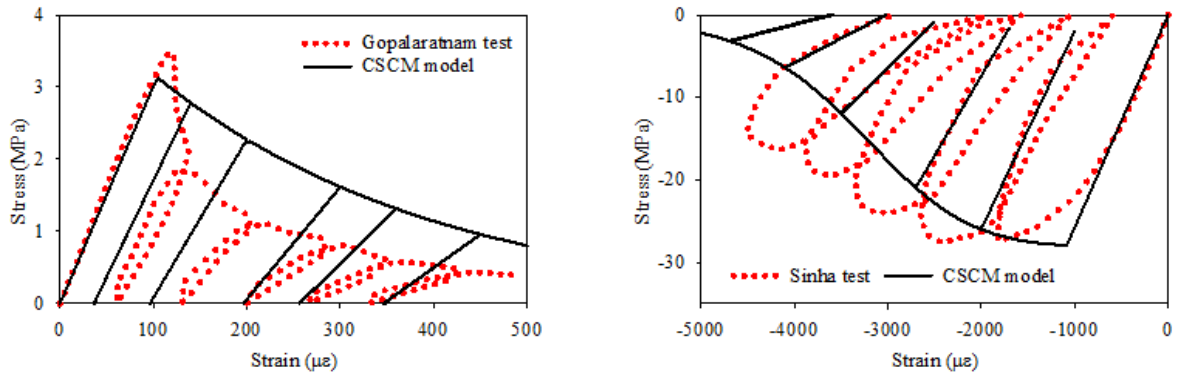

(c) CSC model

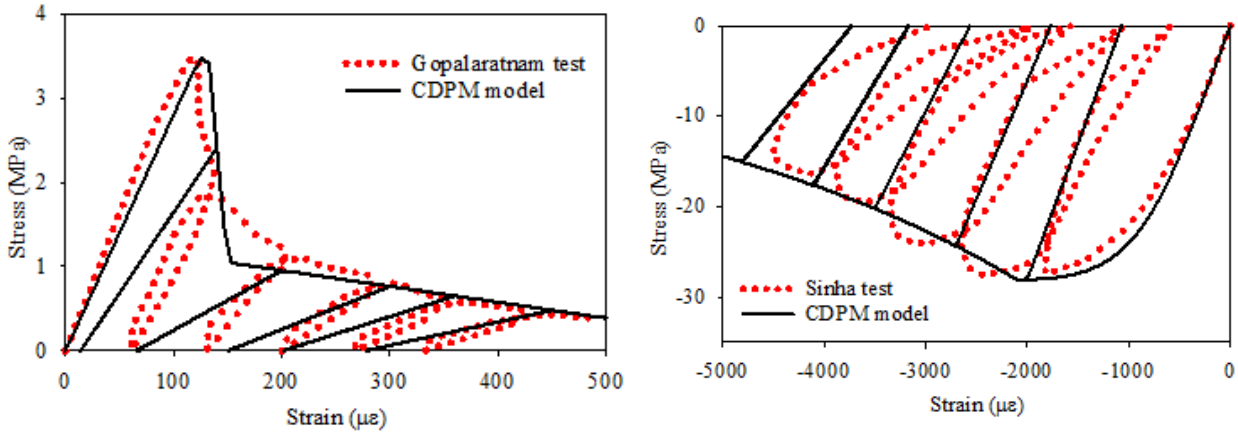

(d) CDP model

Figure 2.1 Comparison of concrete cyclic behavior between test and predicted results using different concrete models

2.2.1. K&C concrete model

The K&C model ("MAT_CONCRETE_DAMAGE_RELIII" in LS-Dyna) [41] uses simple functions to characterize three independent failure surfaces (i.e., the yield, the maximum and the residual strength surfaces), which are each expressed as:

$$F_i(p) = a_{0i} + \frac{p}{a_{1i} + a_{2i}\,p} \tag{2.2}$$

where i donates the failure surface and a_{0i}, a_{1i} and a_{2i} are parameters calibrated for each failure surface from experimental data.

Beyond the yield-strength surface, the current failure surface is linearly interpolated between the yield strength surface and maximum strength surface:

$$F_i(I_1, J_2, J_3) = r(J_3)[\eta(\lambda)(F_m(p) - F_y(p)) + F_y(p)] \tag{2.3}$$

where I_1 is the first invariant of stress tensor; J_2 and J_3 are the second and third invariant of deviatoric stress tensor, respectively; the term $r(J_3)$ is the scale factor in the form of William-Warnke equation [42]; the term λ is the modified effective plastic strain, which is between 0 and λ_m in Eq 2.3; the term η is a function of λ with $\eta(0)=0$ and $\eta(\lambda_m)=1$. The λ_m and the relationship between η and λ is required to be input by users.

The current failure surface after reaching the maximum strength surface is also determined as Eq 2.3, while the λ is between λ_m and λ_{max}. The η is equivalent to zero when $\lambda>\lambda_{max}$.

The K&C concrete model requires a_{0i}, a_{1i} and a_{2i} parameters and a series of λ and η values to simulate the hardening and softening behavior of concrete. However, these parameters are auto-generated in LS-Dyna based solely on the unconfined compression strength of concrete (f'_c). In this context, as recommended by the LS-Dyna User Manual-Volume II [43], the maximum shear

failure surface parameter A0 (a_{0m} in the Eq 2.2) is taken as $-f'_c$ and the rest variables are kept as default values.

Figure 2.1a shows that the K&C model tends to overestimate the degradation of concrete compressive strength and underestimate the strength decrease in tension, and the stiffness reduction in both directions is not observed in the prediction. Accordingly, K&C concrete model may not be appropriate to estimate the cyclic behavior of concrete.

2.2.2. Winfrith model

The Winfrith model ("MAT_WINFRITH_CONCRETE" in LS-Dyna) is based on a smeared-crack model [44]. This model assumes an elastic-perfectly plastic behavior in compression and its yield surface is developed based on the four-parameter plastic surface [45] presented in Eq. 2.4 and Eq. 2.5.

$$F_i(I_1, J_2, \cos 3\theta) = a\frac{J_2}{(f'_c)^2} + \lambda\frac{J_2}{f'_c} + b\frac{I_1}{f'_c} - 1 \tag{2.4}$$

$$\lambda = \begin{cases} k_1 \cos[\frac{1}{3}\cos^{-1}(k_2 \cos 3\theta)] & (\cos 3\theta \geq 0) \\ k_1 \cos[\frac{\pi}{3} - \frac{1}{3}\cos^{-1}(-k_2 \cos 3\theta)] & (\cos 3\theta < 0) \end{cases} \tag{2.5}$$

where θ is Lode angle; a, b, k_1, k_2 are parameters which are a function of (f_t/ f'_c), which can be auto-generated in LS-Dyna; f_t donates the tensile strength of concrete.

In the Winfrith model, the post-cracked behavior of concrete under tension can be defined by 1) linear strain softening without strain-rate effect or 2) bilinear strain softening including strain-rate effects. The linear strain softening option was selected for the simulation because the experiments used in this paper were quasi-static; strain-rate effects are ignored. The crack width, w, at which the normal tensile stress is zero, is given by:

$$w = \frac{2G_f}{f_t} \tag{2.6}$$

where G_f is the fracture energy which can be determined as Eq 2.7 [46]

$$G_f = 73 f'^{0.18}_c \tag{2.7}$$

Figure 2.1b shows no degradation of concrete strength in compression and the decrease of tensile strength is significantly smaller than that in the experiment. Therefore, the Winfrith concrete model cannot reasonably estimate the performances of concrete under cyclic loading.

2.2.3. CSC model

The CSC model was developed for LS-Dyna by the U.S. Department of Transportation [16] and is a continuous surface-cap model which combines the shear failure surface with a hardening compaction surface. The yield function is developed based on three invariants (i.e., I_1, J_2 and J_3) and ca-hardening parameter, κ:

$$f(I_1, J_2, J_3) = J_2 - \Re(J_3)^2 F_f^2(I_1) F_c(I_1, \kappa) \tag{2.8}$$

where F_f is the shear failure surface, as given by Eq (2.10); $\Re(J_3)$ *is the invariant reduction factor [47]; and* $F_c(I_1, \kappa)$ *is the hardening cap, as given by Eqs 2.9–2.12.*

$$F_f(I_1) = \alpha - \lambda \exp^{-\beta I_1} + \gamma I_1 \tag{2.9}$$

where α, λ, β, γ are parameters determined by fitting the model surface to strength measurement from triaxial compression tests.

$$F_c(I_1, \kappa) = \begin{cases} 1 - \dfrac{(I_1 - L(\kappa))^2}{(X(\kappa) - L(\kappa))^2} & I_1 \geq L(\kappa) \\ 1 & I_1 < L(\kappa) \end{cases} \tag{2.10}$$

$$L(\kappa) = \begin{cases} \kappa & \kappa \geq \kappa_0 \\ \kappa_0 & \kappa < \kappa_0 \end{cases} \tag{2.11}$$

$$X(\kappa) = L(\kappa) + RF_f(I_1) \tag{2.12}$$

where the R is the input parameter; and κ_0 is the value of J_1 at the initial intersection of the cap and shear surfaces before hardening is engaged (before the cap surface expands or shrinks). After reaching the yield surface, the cap adjusts to simulate plastic volume change. The cap expends ($X(\kappa)$ and κ increase) to simulate plastic volume compaction; while the cap shrinks ($X(\kappa)$ and κ decrease) as the plastic volume expansion occurs. The adjustment of cap is based on the hardening rule given in Eq. 2.13.

$$\varepsilon_v^p = W(1 - \exp^{-D_1(X - X_0) - D_2(X - X_0)^2}) \tag{2.13}$$

where the ε_V^p is the plastic volume strain, W donates the maximum plastic volume strain, D_1 and D_2 are parameters, and X_0 is the initial location of cap surface for $\kappa=\kappa_0$.

The parameters in Eqs. 2.12 and 2.13 (i.e., X_0, W, D_1, D_2 and R) are determined by fitting to the pressure-volumetric strain curves in hydrostatic compression and uniaxial strain experiment.

The damage formation in CSC model is presented as Eq. 2.14.

$$\sigma_{ij}^d = (1 - d)\sigma_{ij}^{vp} \tag{2.14}$$

where σ_{ij}^d and σ_{ij}^{vp} are stress tensors with and without consideration of damage, respectively, and d is a scalar damage parameter. The value of d increases from zero (undamaged) to one (fully damaged) and accumulates with brittle and ductile damage threshold, τ_b and τ_d. Brittle damage accumulates only when the pressure is tensile and depends on maximum principle strain, ε_{max}:

$$\tau_b = \sqrt{E\varepsilon_{max}^2} \tag{2.15}$$

Ductile damage accumulates only when the pressure is compressive and depends on the total strain components, ε_{ij}:

$$\tau_{\mathrm{d}}=\sqrt{\frac{1}{2}\sigma_{ij}\varepsilon_{ij}} \tag{2.16}$$

In this context, the damage accumulation during strain softening can be calculated as:

$$d(\tau)=\begin{cases}\dfrac{0.999}{D}\left(\dfrac{1+D}{1+D\exp(-C(\tau-r_{0b}))}-1\right) & \text{for brittle damage } \tau=\tau_b\\ \dfrac{D_{\max}}{B}\left(\dfrac{1+B}{1+B\exp(-A(\tau-r_{0d}))}-1\right) & \text{for ductile damage } \tau=\tau_d\end{cases} \tag{2.17}$$

The default values of the above parameters, which describe the material properties of normal strength concrete [43], are used in LS-Dyna in Fig. 2.1c. The CSC model slightly overestimates the compressive strength degradation and the predicted fracture energy in tension is somewhat higher than that in the test. The modest difference between prediction and test results indicates that this model may be acceptable for evaluation of the cyclic behavior of concrete.

2.2.4. CDP model

The damage plastic concrete model (CDP model, MAT273 in LS-DYNA) [14,15] characterizes the failure process of concrete under multi-axial loading. The yield function depends on the volumetric effective stress (σ_{v}), the norm of deviatoric effective stress (ρ), Lode angle (θ) and the hardening variable (k_{p}), which is given by Eq 2.18. The details of flow rules and hardening laws are presented elsewhere [15].

$$\begin{aligned}f_{\mathrm{p}}=(\sigma_{\mathrm{v}},\rho,\theta,\kappa_{\mathrm{p}})=&\left\{[1-q_1(\kappa_{\mathrm{p}})]\left(\frac{\rho}{\sqrt{6}f'_{\mathrm{c}}}+\frac{\sigma_{\mathrm{v}}}{f'_{\mathrm{c}}}\right)^2+\sqrt{\frac{3}{2}}\frac{\rho}{f'_{\mathrm{c}}}\right\}^2\\&+m_0q_1(\kappa_{\mathrm{p}})^2q_2(\kappa_{\mathrm{p}})\left[\frac{\rho}{\sqrt{6}f'_{\mathrm{c}}}r(\cos\theta)+\frac{\sigma_{\mathrm{v}}}{f'_{\mathrm{c}}}\right]-q_1(\kappa_{\mathrm{p}})^2q_2(\kappa_{\mathrm{p}})^2\end{aligned} \tag{2.18}$$

where m_0 is the friction parameter given by Eq 2.19, $r(\cos\theta)$ is the function controlling the shape of the deviatoric section given by Eq 2.20.

$$m_0=\frac{3(f'^{\,2}_{\mathrm{c}}-f_{\mathrm{t}}^2)}{f'_{\mathrm{c}}f_{\mathrm{t}}}\frac{e}{e+1} \tag{2.19}$$

$$r(\cos\theta)=\frac{4(1-e^2)\cos^2\theta+(2e-1)^2}{2(1-e)^2\cos\theta+(2e-1)\sqrt{4(1-e^2)\cos^2\theta+5e^2-4e}} \tag{2.20}$$

where e is the eccentricity parameter, which can be calculated by Eq 2.21 [43].

$$e=\frac{f_{\mathrm{t}}(f_{\mathrm{bc}}^{\,2}-f_{\mathrm{t}}^2)}{f_{\mathrm{bc}}(f'^{\,2}_{\mathrm{c}}-f_{\mathrm{t}}^2)} \tag{2.21}$$

where f_{bc} is the biaxial compressive strength of concrete, which is equal to $1.16f'_{\mathrm{c}}$. The damage function in CDP model is:

$$\sigma=(1-w_t)\sigma_t+(1-w_c)\sigma_c \qquad (2.22)$$

where σ is the effective stress tensor, σ_c and σ_t are the positive and negative parts of the effective stress, w_t and w_c are tensile and compressive damage parameters varying from 0 (undamaged) to 1 (fully damaged). The compressive damage is described by the exponential stress-inelastic displacement law as seen in Fig. 2.2, and ε_{fc} controls the strain softening behavior and is the intersection between the tangential line of the compressive strain softening curve and the x-axis.

There are three tensile damage models in the CDP model: linear, bilinear and exponential. The bilinear damage model illustrated in Fig. 2.3 was used for this study due to its reasonable estimation of experimental data [15]. In the figure, G_f is the fracture energy represented by the shadowed area under the strain softening curve; and w_f is the maximum tensile inelastic strain, which can be determined as $w_f = 4.444G_f/f_t$ [15].

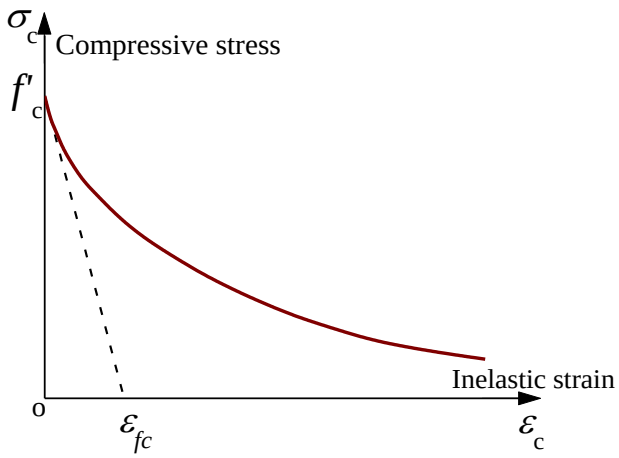

Figure 2.2 Strain softening behavior of compression for CDP model

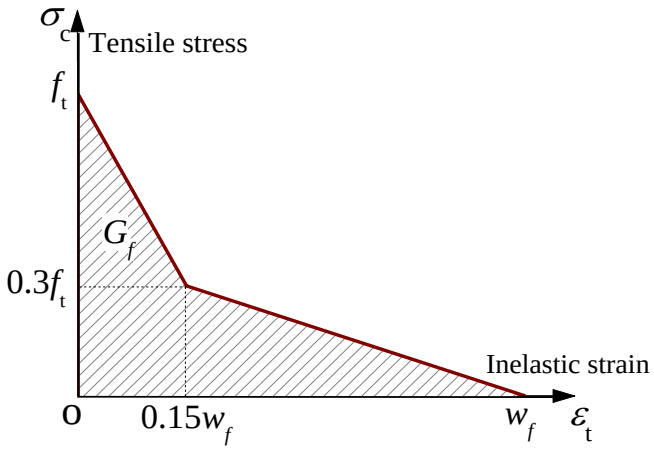

Figure 2.3 Strain softening behavior of tension for CDP model

The default value of ε_{fc} (0.0001) was used in the comparison of Fig. 2.1d, and the CDP model shows good agreement with the test results and provides the best prediction of the four concrete models. Accordingly, the CDP model can be used to evaluate cyclic loading of concrete.

2.3. Selection of concrete element and mesh size

For the modeling, 8-node reduced integrated solid element was used to simulate the concrete behavior. There are 4 commonly-used solid element types in LS-Dyna: the constant stress solid element (ELFORM=1), fully integrated S/R solid element (ELFORM=2), and fully integrated S/R solid element for poor aspect ratio with efficient and accurate formulations, respectively (ELFORM=-1 and -2). The predictions for these 4 element types are compared with the RC column experimental data [33] in Fig. 2.4.

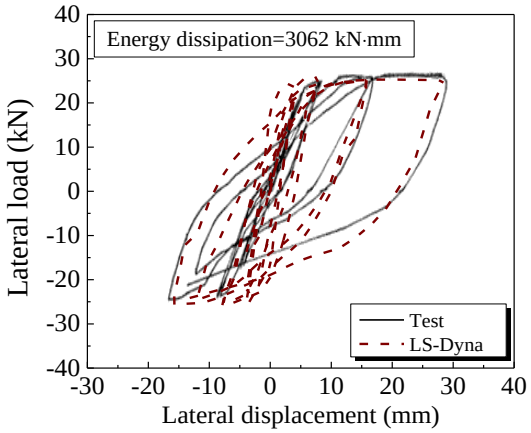

(a) Constant stress solid element

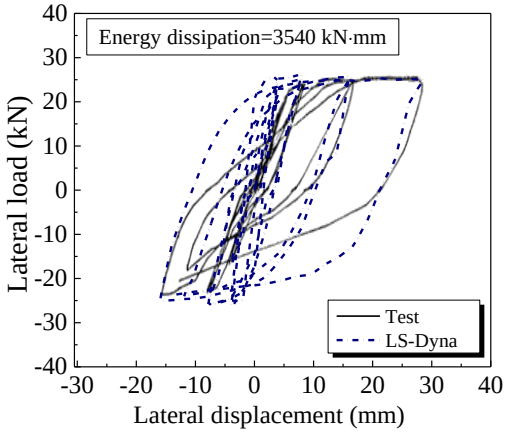

(b) Fully integrated S/R solid element

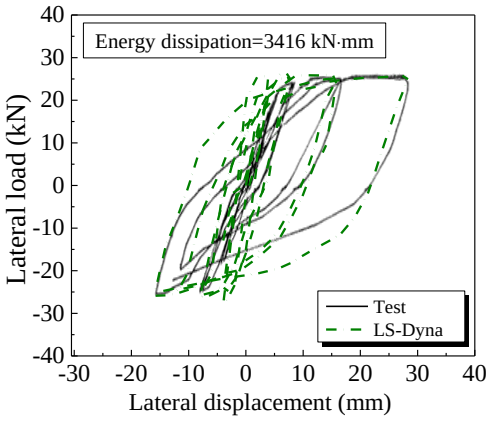

(c) Fully integrated S/R solid element for poor aspect ratio with efficient formulation

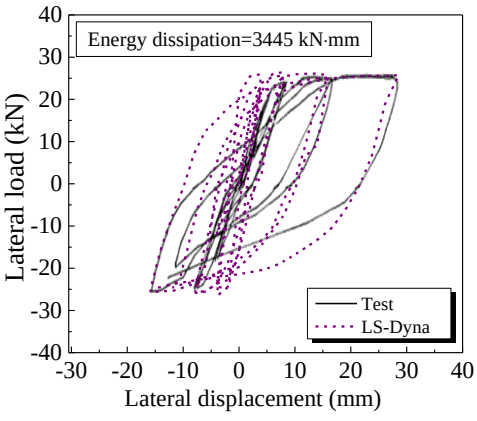

(d) Fully integrated S/R solid element for poor aspect ratio with accurate formulation

Figure 2.4 Predicted load-displacement curve for RC column with different element type

The comparison shows that all of the models predicted specimen resistance with acceptable accuracy, but the constant stress solid element provided the best estimation of the hysteretic

behavior of the test specimen. Further, Fig. 2.5 shows that constant stress solid element provided the best relative calculation time of the four models. The calculation time for the simulation with fully integrated S/R solid element was at least 2.6 times the calculation with constant stress solid element. This element has both accuracy and computational efficiency. Therefore, the constant stress solid element was used in this study.

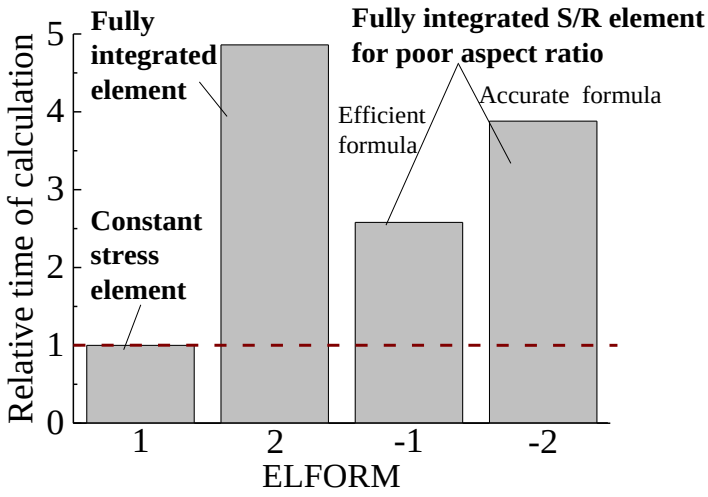

Figure 2.5 Relative time of calculation versus element type

The mesh size depends on the dimension and shape of specimen, but computation time will be large if the mesh is too fine, while an excessively large mesh would adversely affect the accuracy of the prediction. On average, the mesh size used in this study is B/7 where B is the length of short side in concrete column (see Fig. 2.6) and the concrete sections in the regions of expected nonlinear action in the steel were more densely meshed to accurately simulate the stress states and crack patterns of concrete. With this approach, the calculation time can be less than 3 hours using the supercomputer Stampede2 in Texas Advanced Computing Center. The prediction with a mesh size of *B*/14 had a very small difference (0.4%) in predicted results from the B/7 mesh size. Further, the aspect ratio (*h*/*b*) of each element was less than 1.5 to minimize its influences on the predicted results.

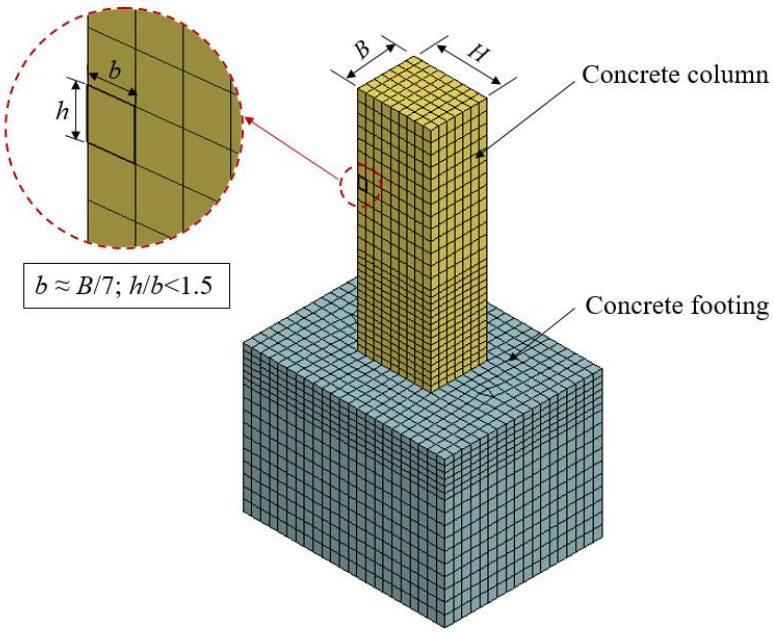

Figure 2.6 Concrete components in simulation

2.4. Model Development for RC Components

2.4.1. Experimental Specimen for Model Development: RC column test [33]

Low and Moehle [33] tested five rectangular column specimens with dimensions of 127×165×514.4 mm subjected to uni- and bi-directional, cyclic loading. The loading history and direction were the study parameters. Specimen I, which was subjected to uniaxial loading about the weak axis, was analyzed (shown in Fig. 2.6). The specimen reinforcement is shown in Fig. 2.7. The yield strengths of No. 3 and No. 2 reinforcing bars were 448 MPa and 444 MPa, respectively. The transversal rebar was No. 9 wire with the yield strength of 414 MPa. The specimen had a concrete uniaxial compressive strength of 35.6 MPa. A constant axial load of 44.5 kN was applied to column.

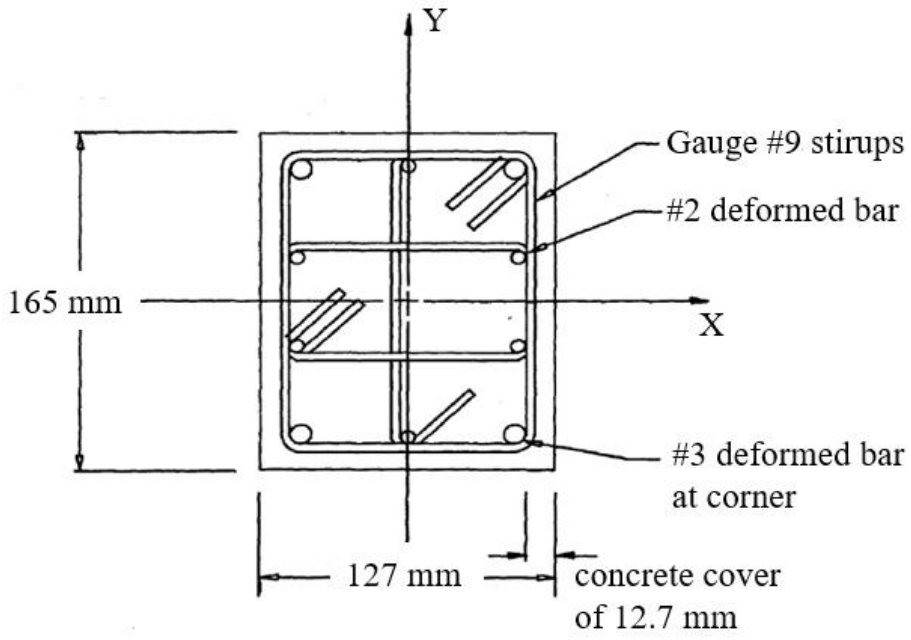

Figure 2.7 Reinforcement configuration [33]

2.4.2. Analytical model

Both CSC and CDP models may predict the behavior of unconfined concrete under cyclic loading with acceptable accuracy. However, most of the concrete in RC column is confined by transverse reinforcement, and the predictions of the four concrete models for confined concrete in RC column under cyclic loadings was evaluated. The comparison of predictions of different concrete models with experimental results are shown in Fig 2.8. The K-C model does not provide a reasonable prediction of the cyclic behavior of RC column, because the predicted initial stiffness and degradation of ultimate strength were notably higher than test results. The Winfrith model accurately predicted the resistance but did not capture deterioration in concrete strength loss. The CSC concrete model prediction exhibited less pinching than the experimental data and degradation of strength was higher. The CDP model prediction matched the experimental data well, and the CDP model was used in the simulation of RC members.

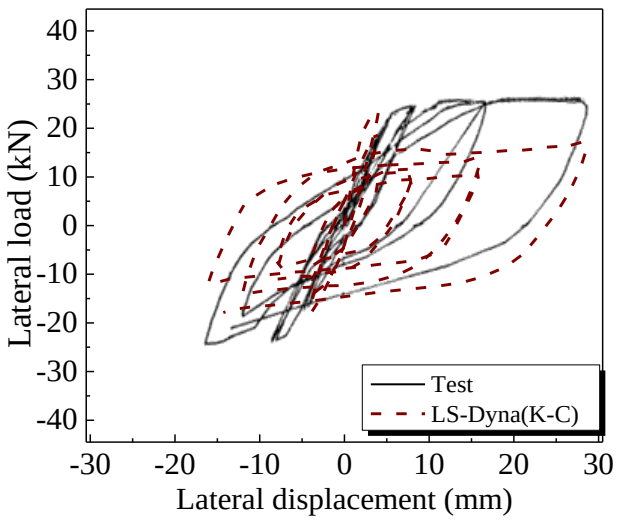

(a) K-C model

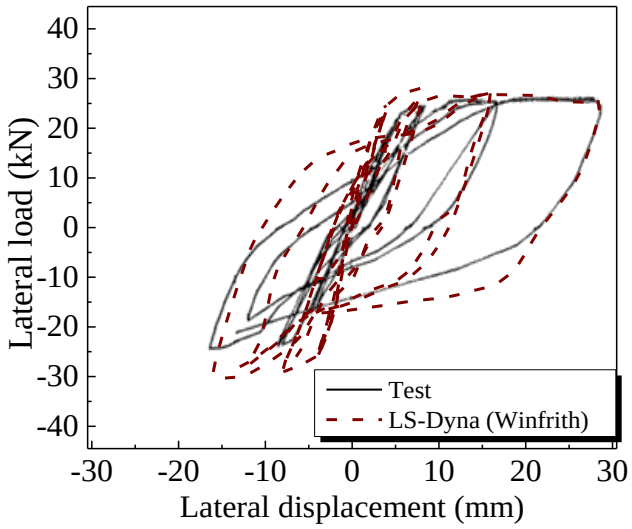

(b) Winfrith model

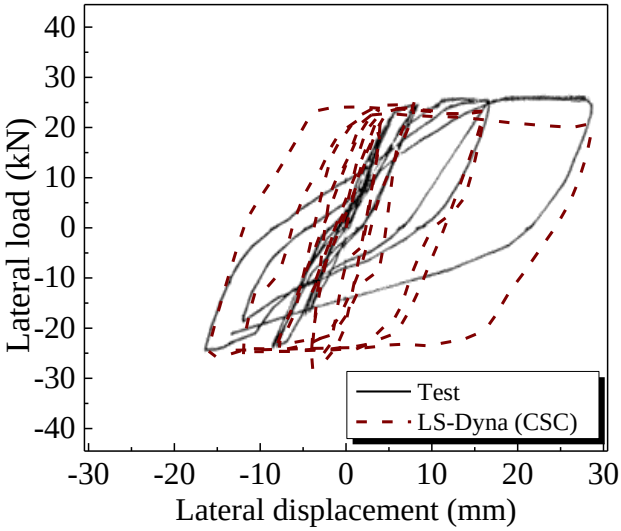

(c) CSC model

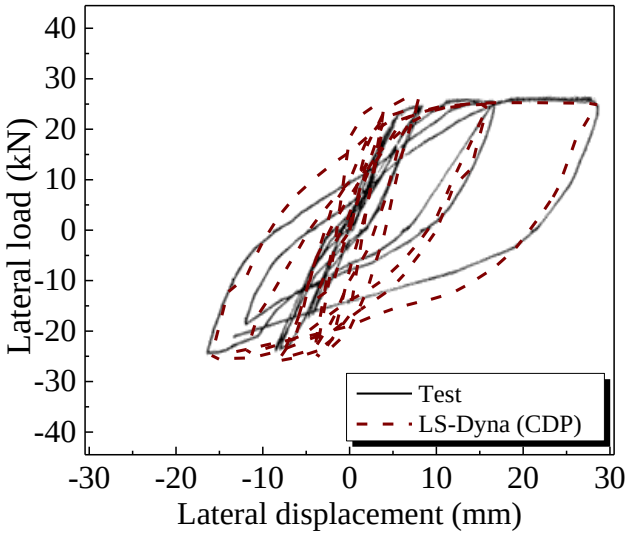

(d) CDP model

Figure 2.8 Predicted load-displacement curve for RC column with various concrete model

The default values for hardening and flow-rule parameters in the CDP model were used, and a bilinear damage model for concrete behavior in tension was selected. Figure 2.9 shows the results of a study to determine the optimal damage parameter in compression, ε_{fc}, and the figure shows that the predicted results that the prediction with ε_{fc} between 0.0005 and 0.05 matched well with the experimental data, with the maximum difference of 0.9% of ultimate strength. Predicted results were not sensitive to the value of ε_{fc} within this range, and the damage parameter in compression was taken as 0.01 for confined concrete.

Considering different conditions of confinement in the concrete core and concrete cover, different values of ε_{fc} were used in the reinforcement-confined concrete core ($\varepsilon_{fc,core}$) and the concrete cover ($\varepsilon_{fc,cover}$). The concrete core confined by transverse reinforcement had the ε_{fc} value of 0.01 as determined above. Figure 2.10 shows the simulation results with various $\varepsilon_{fc,cover}$ values. The figure shows that the prediction with $\varepsilon_{fc,cover}$ higher than 0.0001 can reasonably estimate the cyclic behavior of RC column. Predicted results were not sensitive to the value of $\varepsilon_{fc,cover}$ between 0.001 and 0.01, and the damage factor for concrete cover was taken in the range as 0.005.

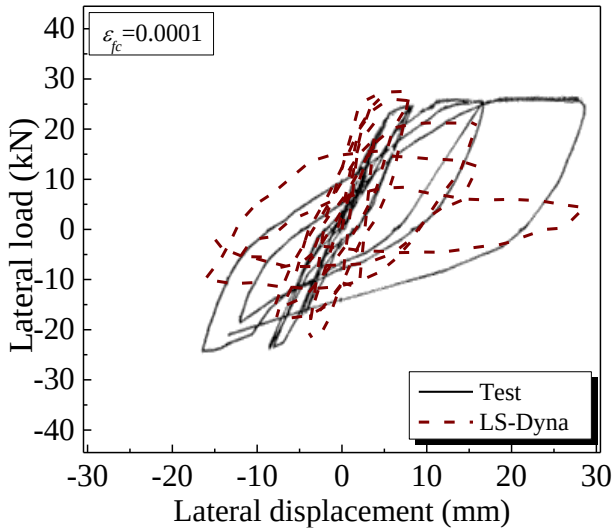

(a) ε_{fc}=0.0001 (default value)

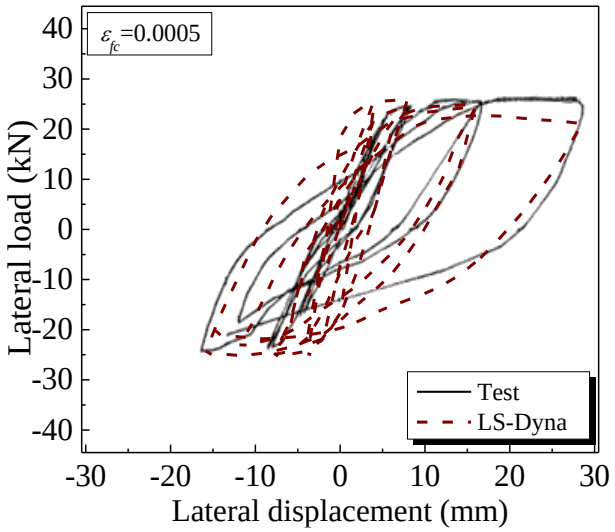

(b) ε_{fc}=0.0005

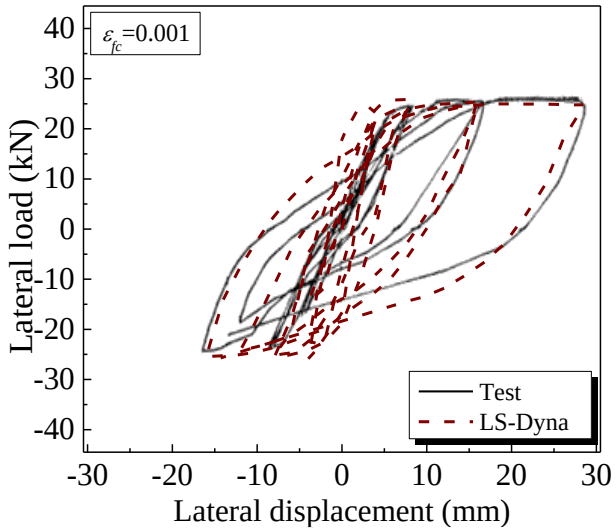

(c) ε_{fc}=0.001

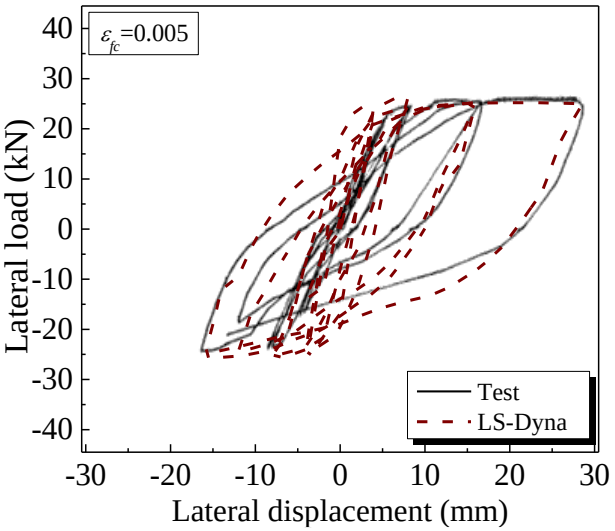

(d) ε_{fc}=0.005

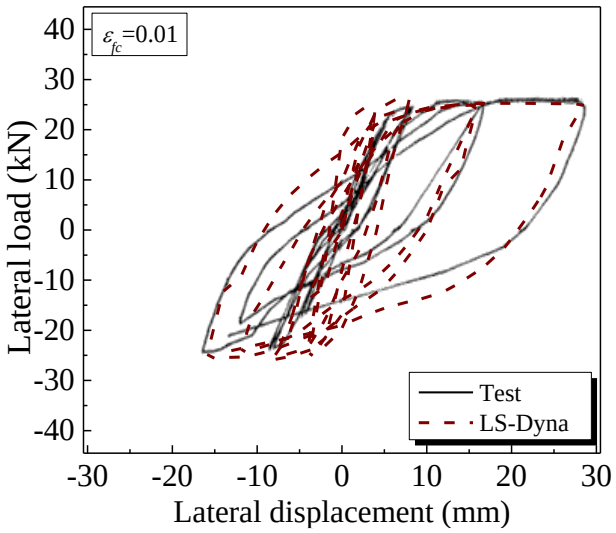

(e) ε_{fc}=0.01

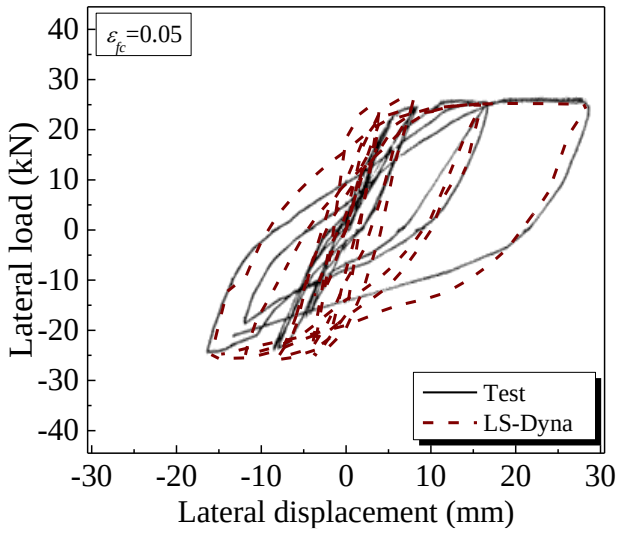

(f) ε_{fc}=0.05

Figure 2.9 Predicted load-displacement curve for RC column with different damage parameters of concrete

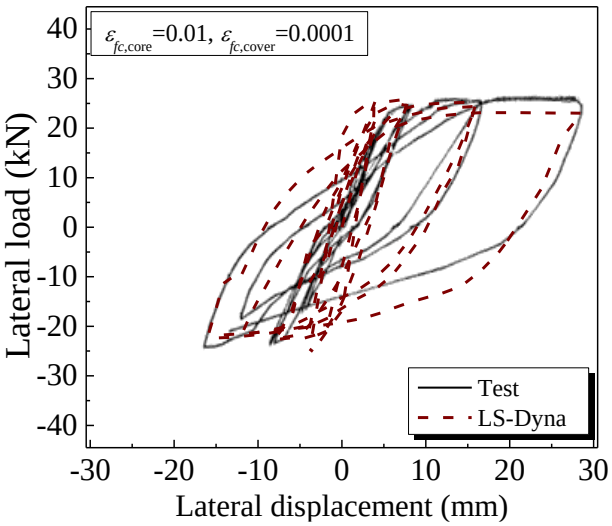

(a) $\varepsilon_{fc,cover}$=0.0001 (default value)

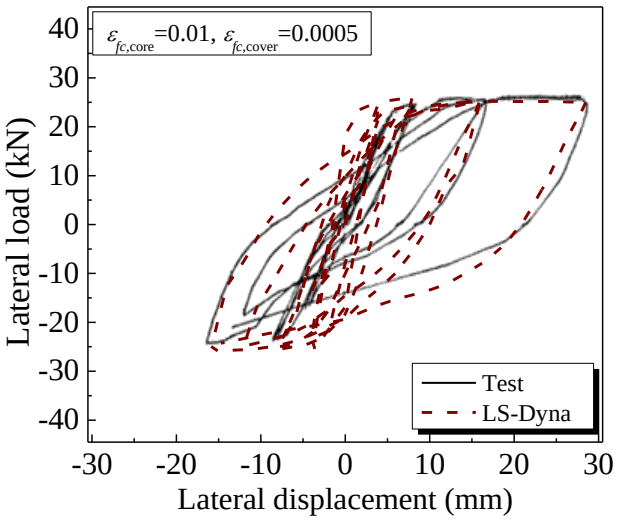

(b) $\varepsilon_{fc,cover}$=0.0005

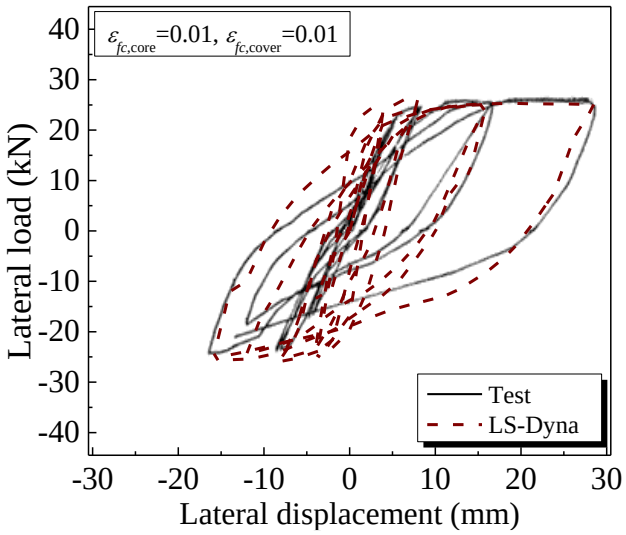

(c) $\varepsilon_{fc,cover}$=0.01

Figure 2.10 Predicted load-displacement curve for RC column with different damage parameters of concrete cover

The reinforcement in RC columns was modeled with the Hughes-Liu beam element with four integration points and the "PLASTIC_KINEMATIC" steel constitutive model [43] shown in Fig. 2.11. The l_0 and l designate undeformed and deformed reinforcement lengths, E_p is the hardening stiffness of the bilinear stress-strain relationship, and β is the hardening parameter varying from zero to one (kinematic hardening if β=0) and isotropic hardening if β=1). Figure 2.12 shows comparisons of computed and measured responses using different β values. The difference of the ultimate strength between the three β values was less than 4%, and the dissipated energy for the specimen with β=1 was only 1.2% higher than that with β=0. Therefore, the simulation results are not sensitive to β and thus the hardening parameter β was taken as 0.1.

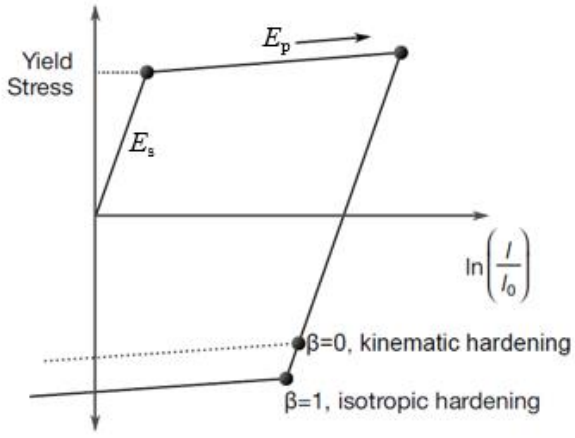

Figure 2.11 Elastic-plastic behavior with kinematic and isotropic hardening [43]

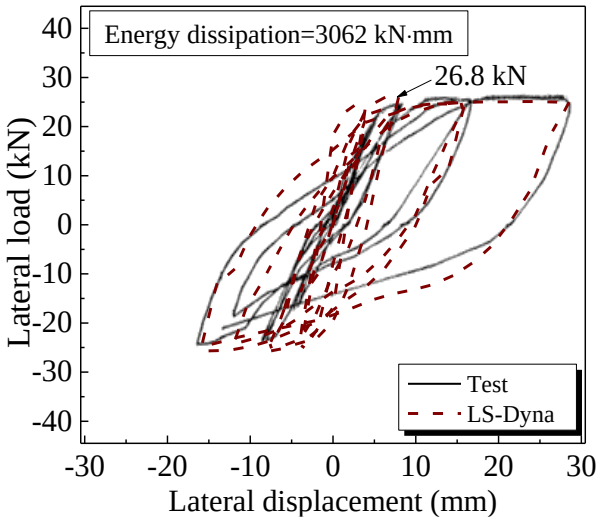

(a) β=0 (default value)

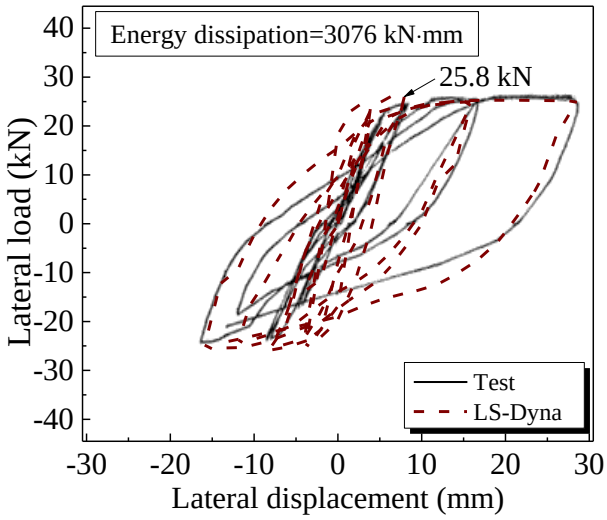

(b) β=0.1

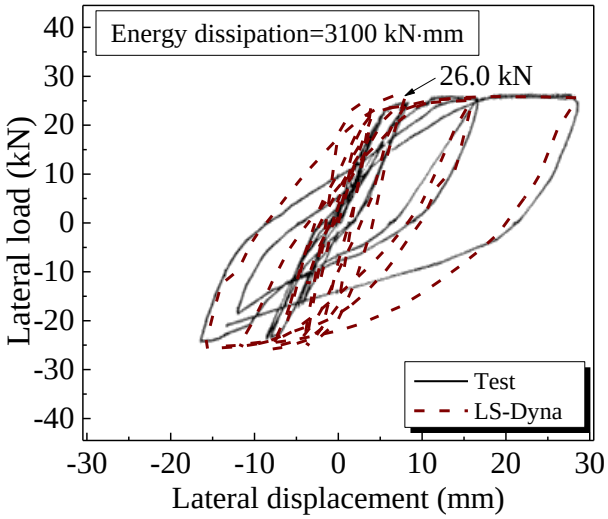

(c) β=1

Figure 2.12 Predictions of RC column with hardening parameters of 0 and 1

The constant stress solid element may cause the hourglass problem when the element is subjected to bending moment [48]. The solid element with a reduced integration cannot detect strain when the element is in pure bending, leading to a zero-energy deformation mode in simulation results. An hourglass-like element shape can be observed in the bottom of the RC column as shown in Figures. 2.13(a) and (b). The Flanagan-Belytschko hourglass control [43] model was used to control this phenomenon. The hourglass coefficient was set as 0.03 to effectively inhibit hourglass modes, while minimizing the nonphysical stiffening of the cyclic

response. The shape at the bottom of RC column using the Flanagan-Belytschko hourglass control is presented as Figure 2.13(c):

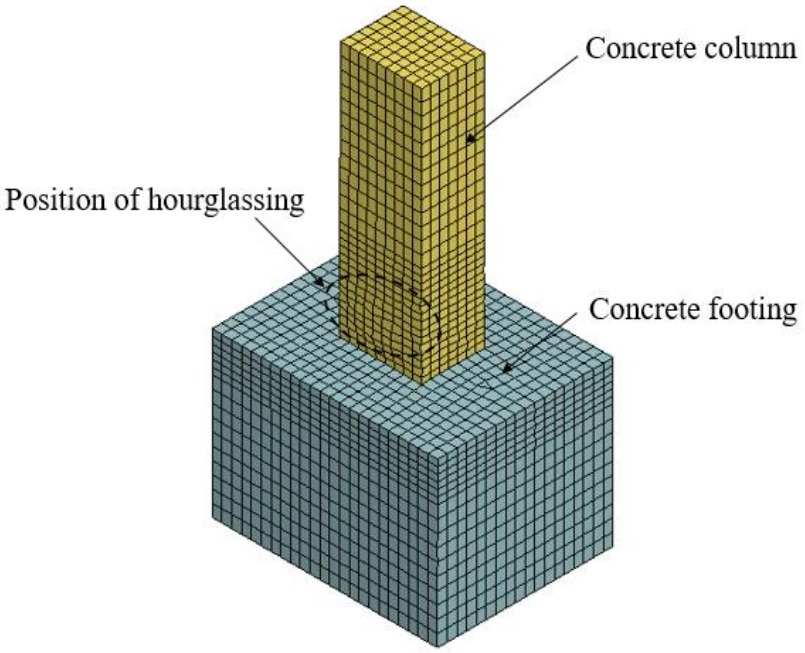

(a)Position of hourglassing

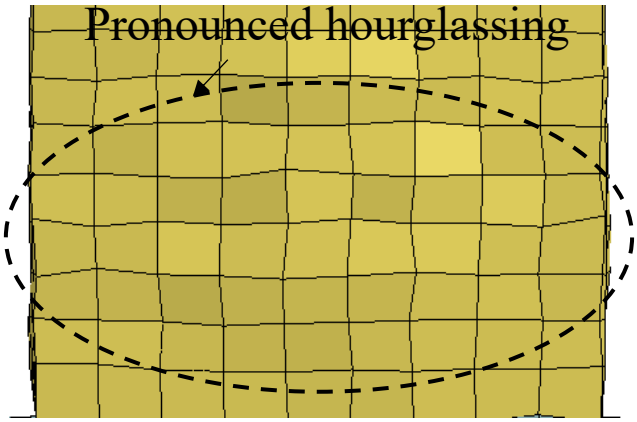

(b)without hourglass control

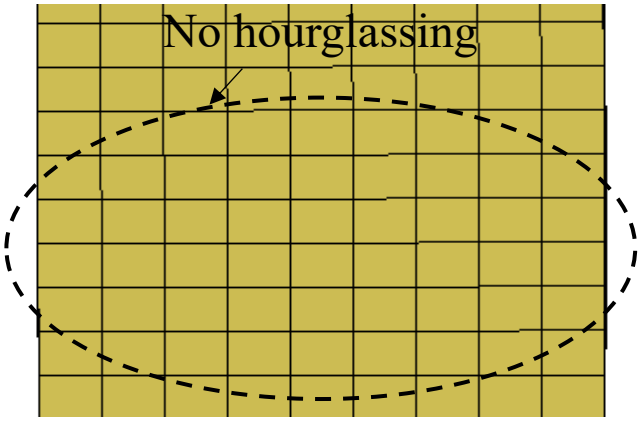

(c)with hourglass control

Figure 2.13 Hourglass pattern in the bottom of RC column

The bond-slip model proposed by Murcia-Delso et al. [26] was used to simulate response of the RC reinforcement embedded in concrete. In LS-Dyna, this model is established by using the constrained "BEAM_IN_SOLID" with defining the required function expressions. Figure 2.14 illustrates the parameters of this model where τ_{max} is the bond strength, s_{peak} is the slip at the peak

bond strength, and s_R is the clear rib spacing of reinforcement (usually a distance between 40% and 60% of the bar diameter). In absence of experimental data, τ_{max} and s_{peak} can be determined as:

$$\tau_{max} = 1.163 f_c^{3/4} \quad (2.23)$$

$$s_{peak} = 0.07 d_b \quad (2.24)$$

where f'_c is the compressive strength of concrete and d_b is bar diameter.

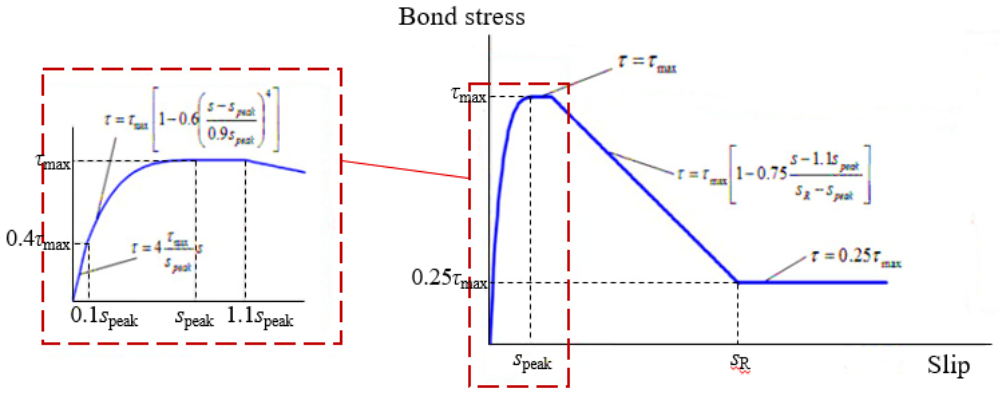

Figure 2.14 Bond-slip behavior proposed by Murcia-Delso et al. [26]

2.4.3. Validation

The resulting model was further validated by comparison with experimental result from Specimen HC4-8L19-T10-0.2P [34], shown in Fig. 2.15. The model captured the load-displacement behavior of RC column with a maximum strength difference of 14.7%. Due to the accurate modeling of concrete and bond-slip of reinforcement, the shape of the predicted load-displacement curve is similar to the measured response, leading to similar energy dissipation between the predicted and measured results.

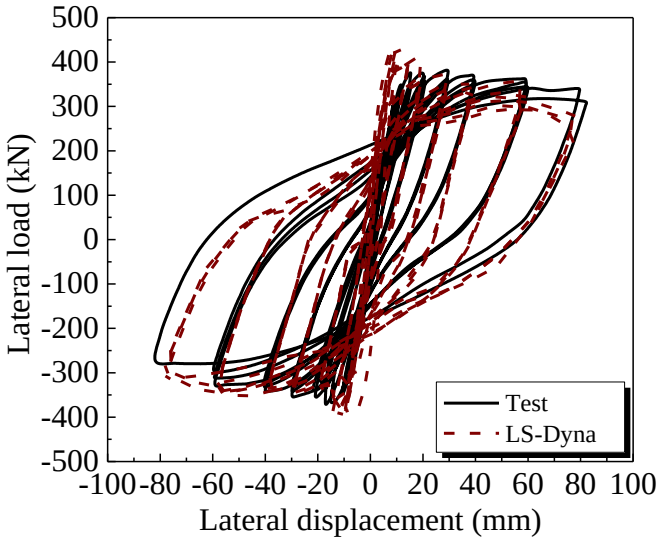

Figure 2.15 Comparison between the predicted and test results from Xiao's experiment

2.5. Model Development for Concrete Filled Steel Tubes

2.5.1. Experimental Specimens for Model Development: CFST tests [3–4]

Han et al. [4] investigated the seismic performance of hexagonal CFST columns encased in RC base as illustrated in Fig. 2.16. The height of RC base, axial load level, connection between the RC base and the CFST column, and the specimen size (scaled vs. full scale) were studied. The full-scale specimen with the lower height of RC case (CBL-2-0.3-2) was selected to evaluate modeling method. The hexagonal CFST had a sectional width (B) of 180 mm, tube thickness of 7.5 mm, effective length (L) of 1550 mm, outer component width (w_r) of 110 mm and outer component height of 600 mm. The cube compressive strength of RC base and concrete fill concrete (f_{cu}) were 52.3 MPa and 65.6 MPa, respectively. The yield strength for the steel tube was 262 MPa (note that this steel strength is not uncommon for tubes).

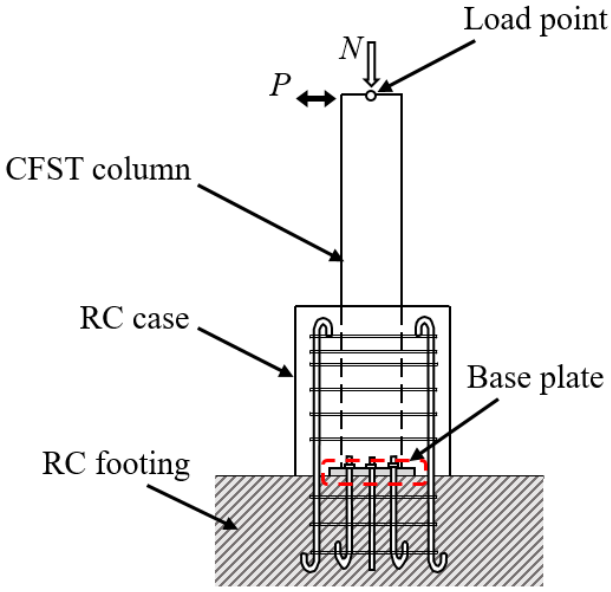

Figure 2.16 Composition of concrete-encased column base [4]

To determine the parameters for the tube to concrete bond model, the measures response of four bond CFST specimens were used, shown in Fig. 2.17 [3]. All specimens had circular tubes with outside diameter of 508 mm and wall thickness of 6.35 mm. The height from the concrete fill was 1.524 m, and there was a 50mm and a 25mm gap between the end of the steel tube and concrete fill to allow slip, respectively. The steel tubes were either straight-seam or spiral-weld and the concrete fill was either conventional or with a low-shrinkage admixture. The straight-seam tube and spiral-weld tube without low shrinkage admixture were used to develop the modeling method. As shown in the figure, a universal testing machine was used to apply the vertical load to the concrete fill; external vibrating wire gages were used to determine the response of the steel tube, which, in turn, were used to determine the bond stress. As a basis of calibration, the test results are presented in Fig. 2.17b. (The comparison with the analytical model is in shown in Fig. 2.22)

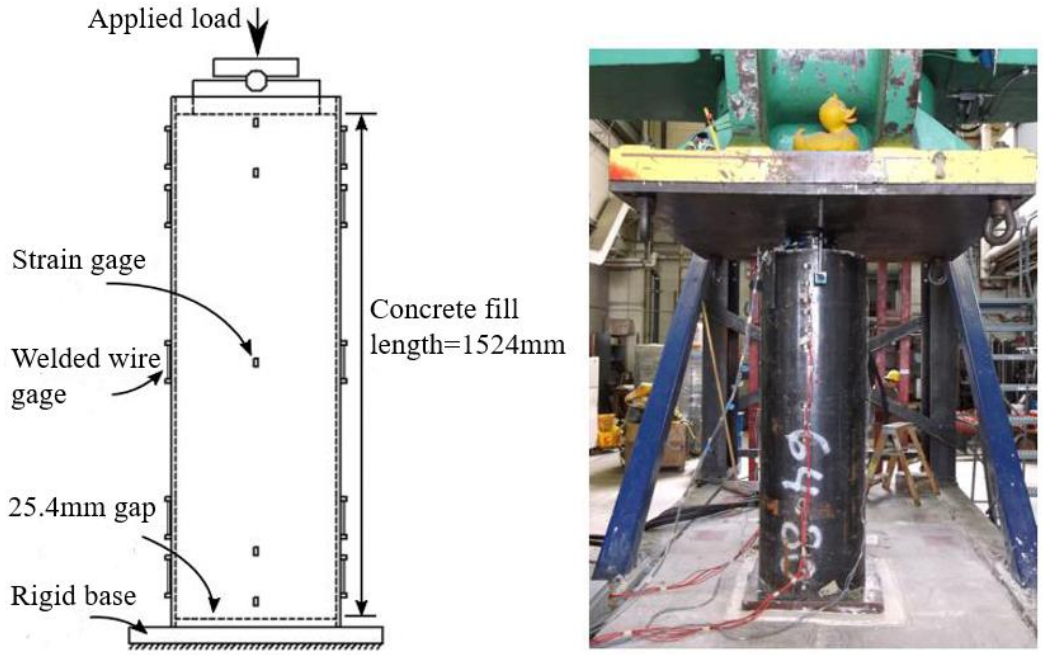

(a) Test aparatus

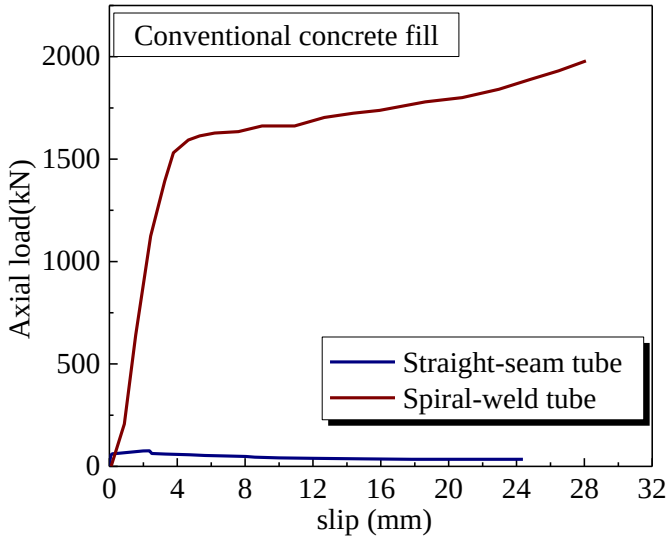

(b) Measured responses

Figure 2.17 Test information [3]

2.5.2. Analytical model

The CFST column to RC base connection was analyzed with the four different concrete models with comparisons between analyses and experiment shown in Fig. 2.18. Buckling of the steel

tube as observed in the experiment [4] was predicted by the models using the CSC and CDP models, but was not predicted by the models using the other two concrete models. The CDP model had much better agreement with the experimental results than the CSC model, and so the CDP model was selected to simulate the behavior of CFST.

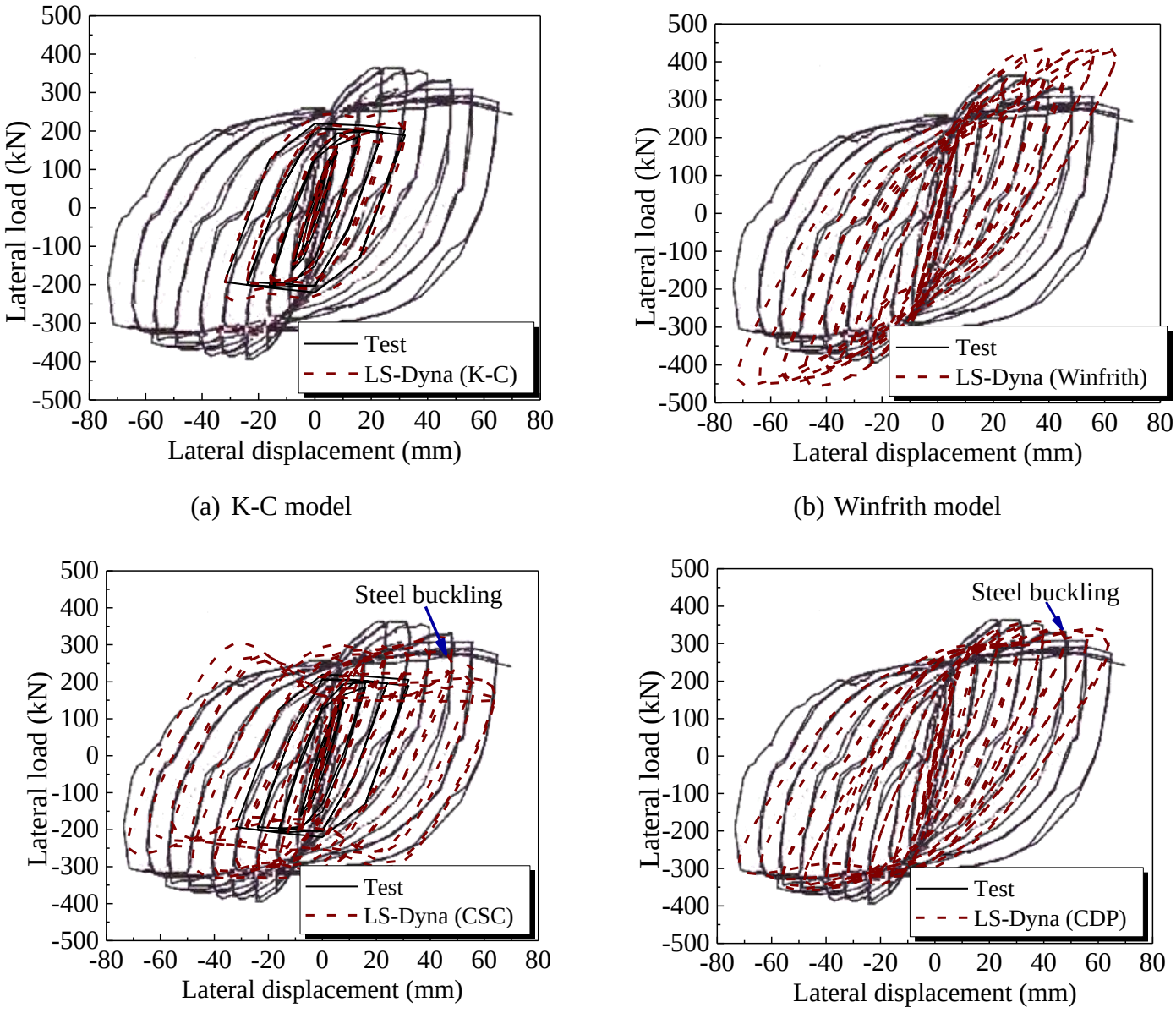

Figure 2.18 Predicted load-displacement curve with various concrete model

The steel tube was modeled using the Belytschko-Tsay shell element [49,50] with two integration points through the shell thickness with the PIECEWISE_LINEAR_PLASTICITY (MAT024) constitutive model with isotropic hardening [19]. This material type can define arbitrary stress vs. strain curve and failure based on a plastic strain. In this context, a trilinear

stress-strain relationship (see Figure 2.19) is used to predict the behavior of steel tube. In the figure, the f_u and f_y represented ultimate strength and yield strength of steel tube. The ε_y, ε_c and ε_u donated the yielding strain, strain at the maximum stress and ultimate strain, respectively. Young's modulus of the steel (E_s) and Poisson's ratio were 207 GPa and 0.3, respectively, as established from a coupon test for research compared to the analysis [4]. The strain corresponding to the ultimate steel strength and failure strain were set as 0.1 and 0.25, respectively.

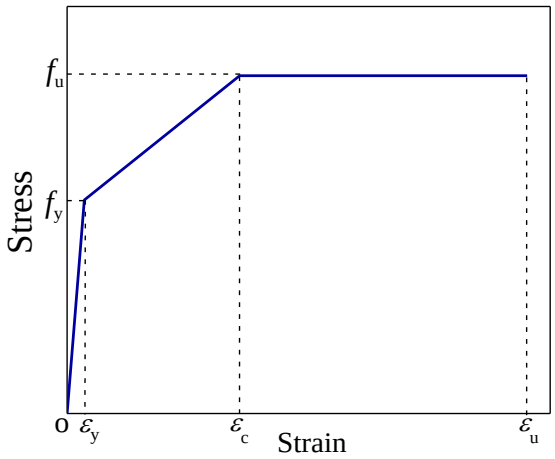

Figure 2.19 Stress-strain relationship for steel tube

A separate study was performed to determine the compressive damage parameter, ε_{fc}, for CFST. Figure 2.20 shows the simulated vs. measured response for ε_{fc} values ranged from 0.0001 (default value) to 0.05 (all other modeling parameter kept constant). It can be seen lower ε_{fc} values of 0.0001 to 0.001 predicted sudden degradation not seen with the experimental data (see Figures 2.20a and b). Models with ε_{fc} between 0.002 and 0.01 predicted the cyclic behavior with reasonable accuracy. An ε_{fc} value of 0.01 was adopted because its simulation results were closest to the measured response in both loading directions.

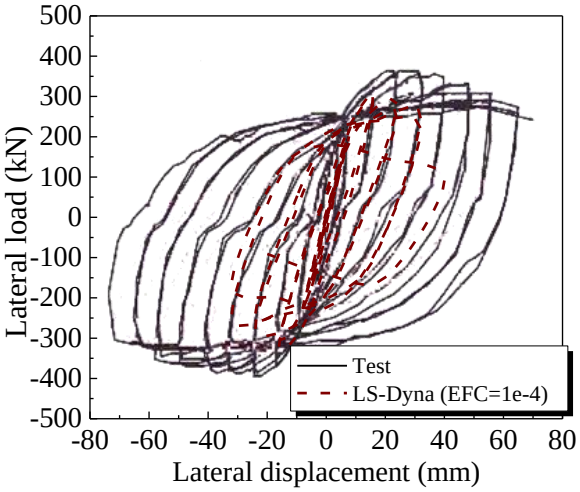

(a) ε_{fc}=0.0001 (default value)

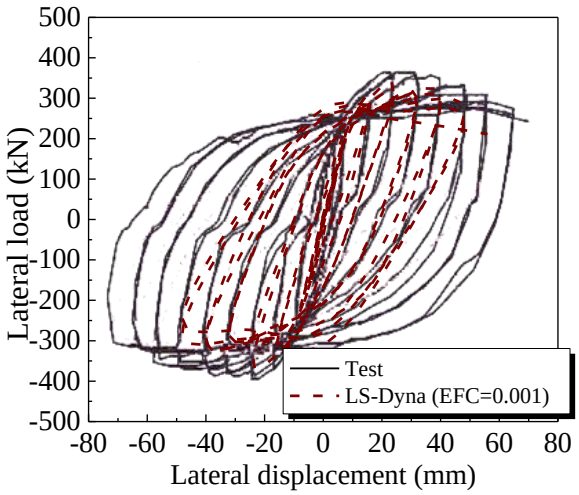

(b) ε_{fc}=0.001

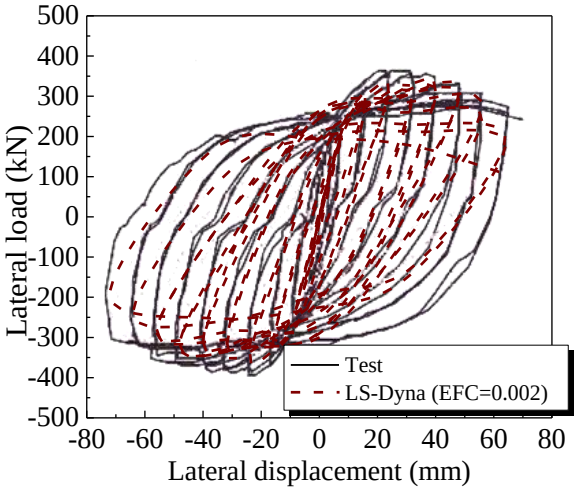

(c) ε_{fc}=0.002

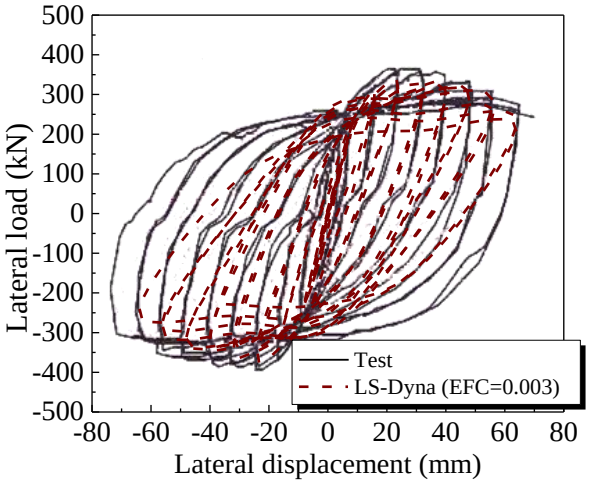

(d) ε_{fc}=0.003

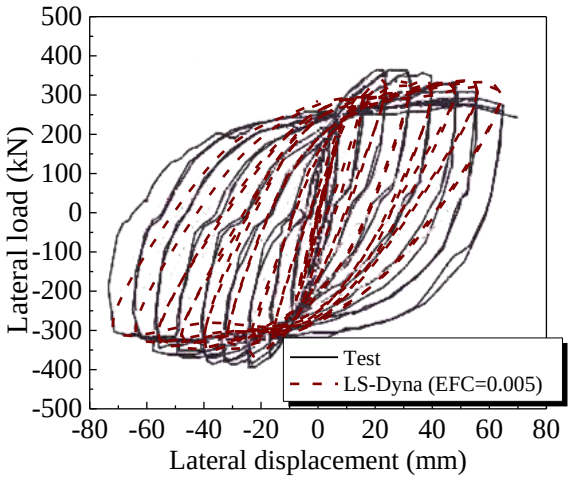

(e) ε_{fc}=0.005

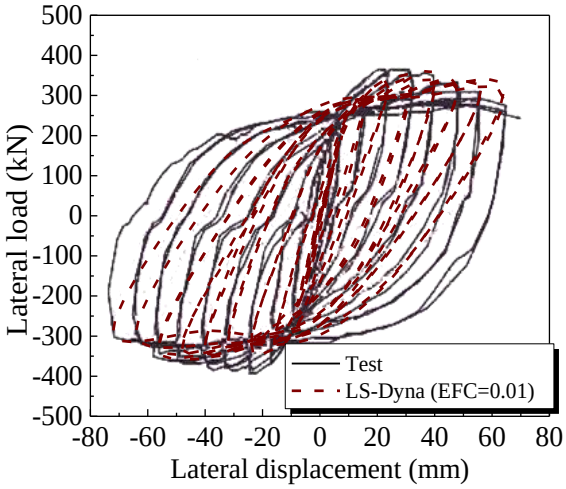

(f) ε_{fc}=0.01

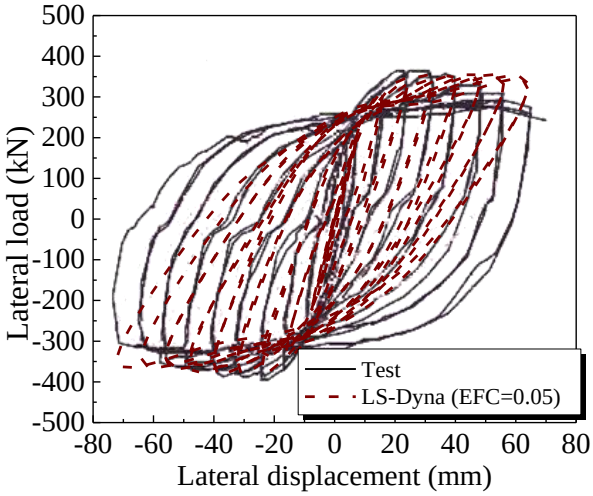

(g) ε_{fc}=0.05

Figure 2.20 Predicted load-displacement curve with different damage parameters for the CDP model

Unlike the RC column, the hourglass effect was not pronounced in CFST analysis. This was determined by comparing hourglass energy to the internal energy and was less than 2.8% of the internal energy. As a result, it was ignored.

Nonlinear springs between steel tube and concrete are a feasible method for modeling bond-slip behavior. However, this method was relatively expensive in calculation time and complicated for modeling. As a result, the fracture model for the cohesive material model "MAT_COHESIVE_MIXED_MODE" (MAT138 in LS-Dyna) was used to model bond-slip based on "AUTOMATIC_SURFACE_TO_SURFACE_TIEBREAK" contact in LS-Dyna with Option=9. The details of this cohesive model are presented in Figure 2.21.

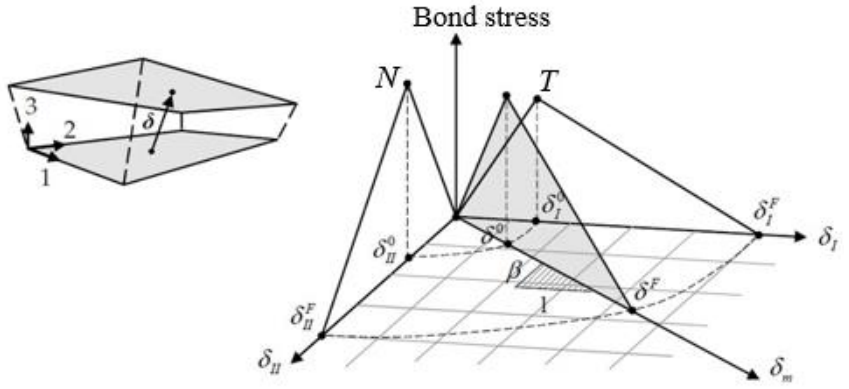

Figure 2.21 Mixed-mode traction-slip law [43]

In this figure, the δ_I and δ_{II} were the slips in the tangential and normal directions, respectively; δ_I^0 and δ_{II}^0 were the slips at the maximum bond stress; δ_I^F and δ_{II}^F were the ultimate slips in both directions; *T* and *N* represented the peak stress in tangential and normal direction, respectively. In this cohesive model, the ultimate slip was defined by:

$$\delta^F = \frac{2(1+\beta^2)}{\delta^0}\left[\left(\frac{EN}{GIC}\right)^{XMU} + \left(\frac{ET\times\beta^2}{GIIC}\right)^{XMU}\right]^{-\frac{1}{XMU}} \tag{2.25}$$

When XMU>0. This equation can be expressed as B-K model when (XMU<0):

$$\delta^F = \frac{2}{\delta^0\left(\frac{1}{1+\beta^2}EN^{\gamma} + \frac{\beta^2}{1+\beta^2}ET^{\gamma}\right)^{1/\gamma}}\left[GIC + (GIIC - GIC) + \left(\frac{ET\times\beta^2}{EN+ET\times\beta^2}\right)^{|XMU|}\right] \tag{2.26}$$

where *EN* and *ET* are the normal and tangential stiffness, respectively; *GIC* and *GIIC* donate the energy releasing rate at normal and tangential directions; and β is the "mode mixity", which is defined as $\beta=\delta_{II}/\delta_I$.

The parameters in tangential direction in the contact model were calibrated using the results of the push-out test of CFST specimen (Fig. 2.17). The experiments by Stephens et al. [3] were used to determine *ET*, *T* and *GIIC*. In the normal direction, parameters of *EN*, *N* and *GIC* were set as approximately zero to simulate the initial slip condition between concrete core and steel tube [51,52]. The calibrated parameter values used in this paper are specified in Table 2.1. The comparison between the simulation results and experimental data was presented in Fig. 2.22. The comparative results showed that the LS-Dyna prediction had good agreement with the experiment data.

Table 2.1 Parameters of bond-slip model for different steel tube types for all concretes

Tube type	*EN* (MPa)	*ET* (MPa)	*N* (MPa)	*T* (MPa)	*GIC*	*GIIC*
Straight-seam tube	6.5e-5	0.065	1e-5	0.032	0.01	0.44
Spiral-weld tube	2e-6	0.2	1e-5	0.75	0.01	1e6

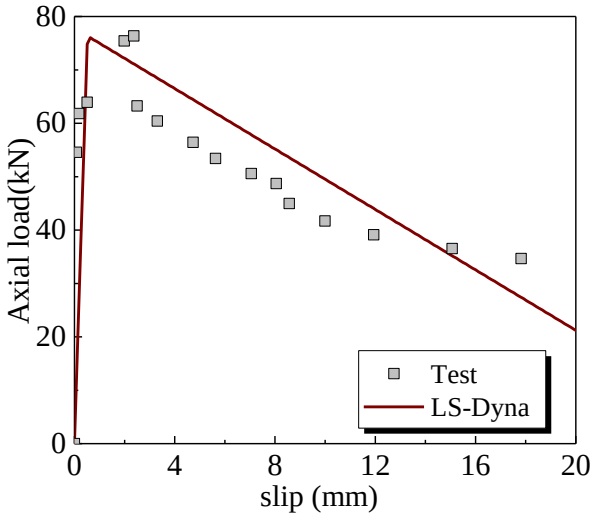

(a) Straight-seam tube

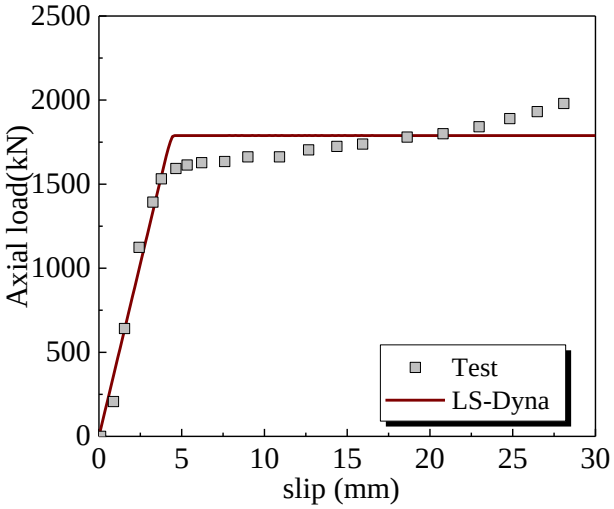

(b) Spiral-weld tube

Figure 2.22 Comparison of bond stress-slip response between predicted and test results

It should be noted that the bond strength in the tangential direction for the straight-seam tube was very low (0.032 MPa) [3]. This bond strength value would increase with the decreasing *D*/*t* of tube due to the decreasing size of gap, which is induced by concrete shrinkage [24,53]. The linear relationship between bond strength and *D*/*t* proposed by Roeder et al. [53] can be used to predict CFST bond behavior with lower *D*/*t* (see Eq. 2.27). It is reasonable to assume that the *D*/*t* ratio can significantly affect the bond behavior of CFST with spiral-weld tube, but the experimental evidence to support this assumption is not available. Thus, more experiments are

still needed to be performed to investigate the influence of D/t ratio on the bond behavior of CFST using spiral-weld tube.

$$f_{\text{bond}} = 2.109 - 0.026(D/t) \text{ MPa} \quad (2.27)$$

2.6. Validation

Figure 2.23 compares the predicted and observed steel-tube buckling and cracking in the RC base [4]. The FE model provides reasonably accurate estimates of the observed behavior.

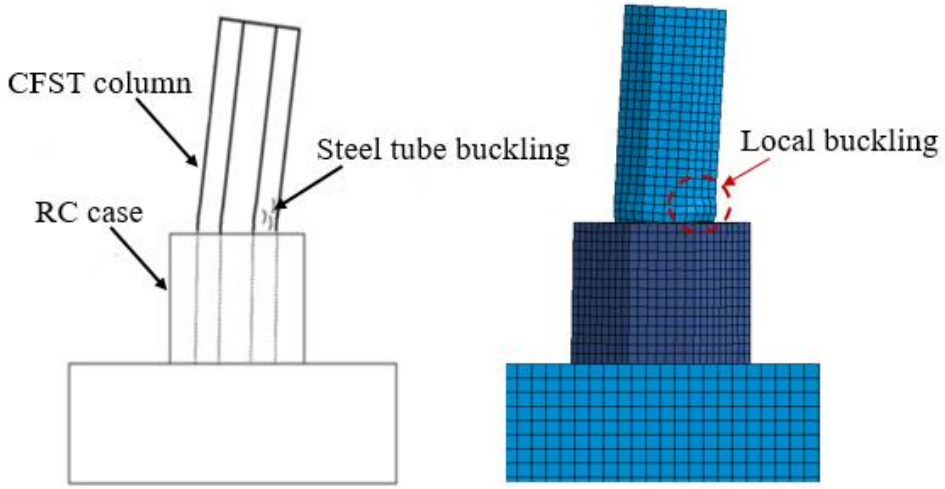

(a) Local buckling by the end of test (drift ratio=6.7%)

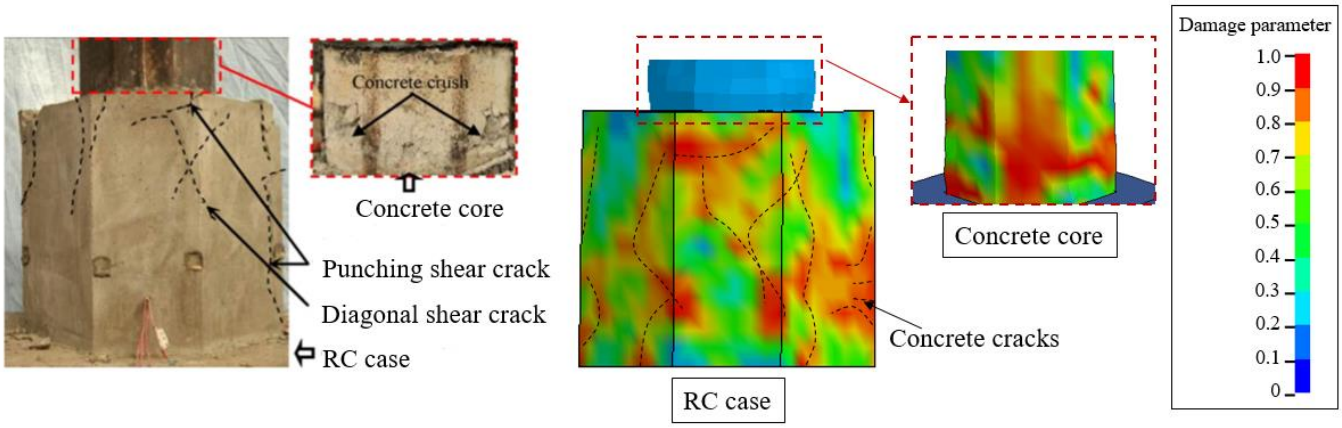

(b) Crack pattern

Figure 2.23 Comparison of failure pattern between the predicted and test results from Han's experiment

Figures 2.24 and 2.25 compare the predicted and measured or observed experimental results from another study [35]. In this study, Specimen II was designed with an inadequate embedment; this specimen was selected because it sustained significant damage to the concrete footing and is challenging to model. Specimen III was selected because it has adequate embedment and a

ductile response. These show the FE model predicts the load-displacement curves with the maximum strength difference of 4.3% and 0.5% for Specimens II and III, respectively. The cracking in the footing, concrete crushing and steel tube buckling are also accurately simulated in the model, and the predicted behavior accurately reflects differences in failure mode and performance.

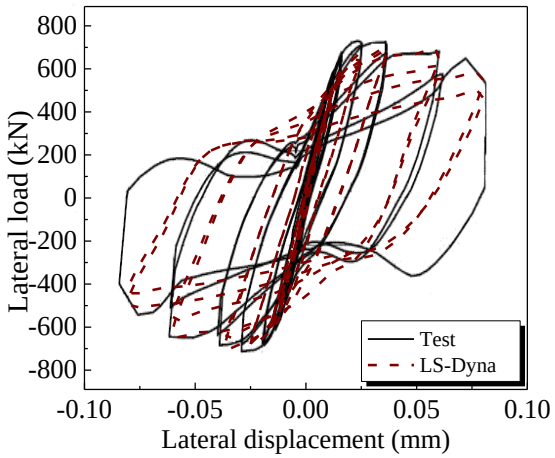

(a) Load-displacement curve

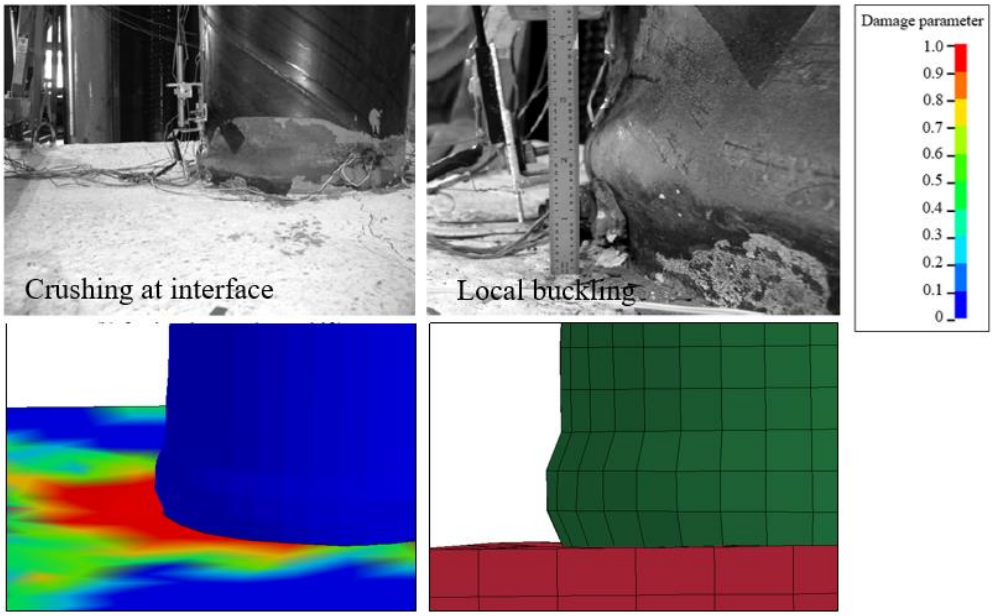

(b) Failure pattern

Figure 2.24 Comparison between the predicted and test results from Roeder et al. 2012 (Specimen III)

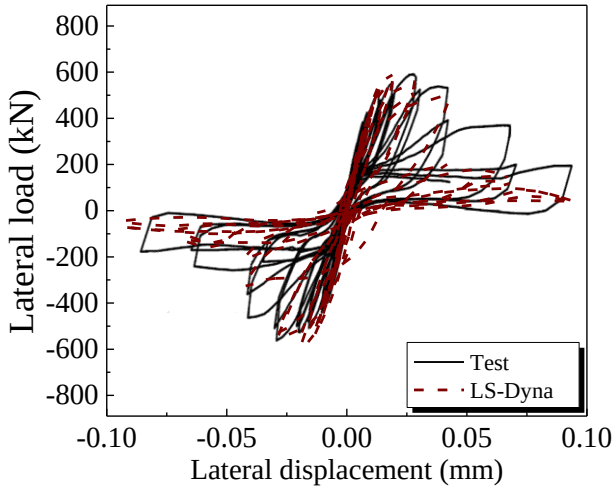

(a) Load-displacement curve

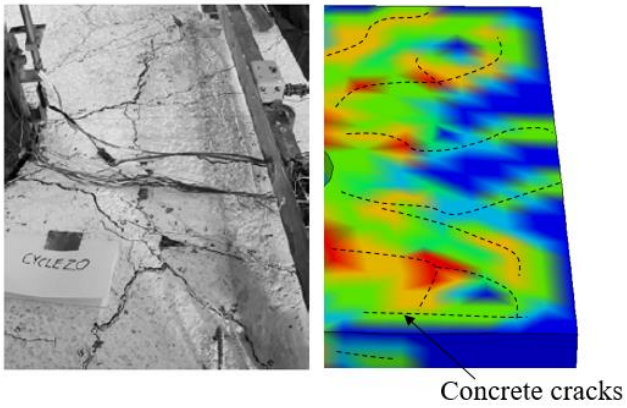

(b) Failure pattern (cracking in foundation)

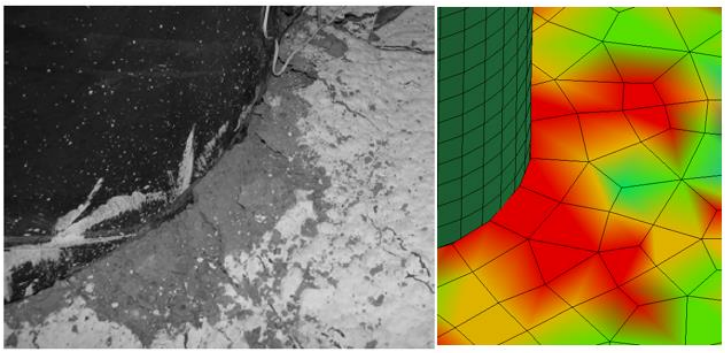

(c) Failure pattern (crushing at interface)

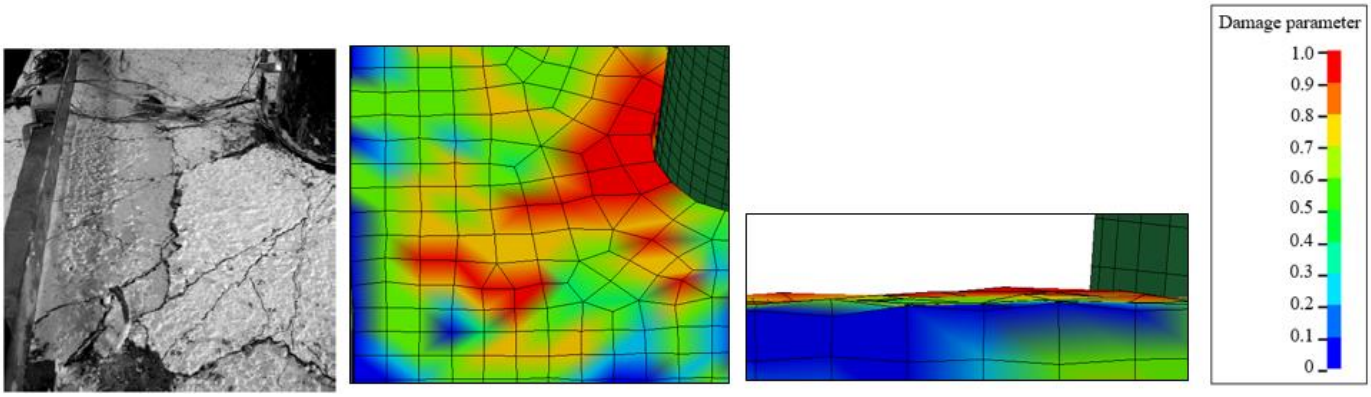

(c) Failure pattern (uplifting of foundation)

Figure 2.25 Comparison between the predicted and test results Roeder et al. 2012 (Specimen II)

2.7. Summary of Recommendations

This report provides a general method to establish a FE model for RC and CFST specimens. All of the recommendations are summarized：

Table 2.2 Summary of modelling recommendations

Components	Constitutive model	Parameters	Values
Concrete	CDP model	Compressive damage model	Exponential
		Tensile damage model	Bilinear
		Compressive damage parameter (ε_{fc})	0.005 (concrete cover) 0.01 (concrete core)
		Tensile damage parameter (w_f)	$4.444G_f/f_t$.
		Hardening parameters	Default values in LS-Dyna
Reinforcement	"PLASTIC_KINEMATIC" (MAT003 in LS-Dyna)	Combination parameter (β)	0.1
Steel tube	"PIECEWISE_LINEAR_PLASTICITY" (MAT024 in LS-Dyna)		
Bar-concrete interface	Bond-slip model proposed by Murcia-Delso et al. [26]		
	"MAT_COHESIVE_MIXED_MODE" (MAT138 in LS-Dyna)	Normal stiffness (EN)	6.5e-5
		Tangential stiffness (ET)	0.065

Tube-concrete interface (straight-seam tube)		Normal bond strength (*N*)	1e-5
		Tangential bond strength (*T*)	0.032 or Eq. 2-25
		Normal energy releasing rate (*GIC*)	0.01
		Tangential energy releasing rate (*GIIC*)	0.44
Tube-concrete interface (spiral-weld tube)	"MAT_COHESIVE_MIXED_MODE" (MAT138 in LS-Dyna)	Normal stiffness (*EN*)	2e-6
		Tangential stiffness (*ET*)	0.2
		Normal bond strength (*N*)	1e-5
		Tangential bond strength(*T*)	0.75
		Normal energy releasing rate (*GIC*)	1e6

4

This chapter has described nonlinear FE model recommendations in LS-Dyna for predicting the cyclic behavior of RC and CFST members and connections using the commercially available LS-Dyna nonlinear analysis software. Three groups of typical experimental results were selected to calibrate the important parameters in the model.

To select the most accurate concrete model, the predicted results with four commonly used concrete models were compared against the measured responses for plain concrete, RC and CFST. The results showed that the prediction with concrete damage plastic model (CDP model) agreed well with the test results. In the CDP model, the compressive damage factor (ε_{fc}) for confined concrete core was selected as 0.01 according to the comparative results, while the ε_{fc} value for concrete cover was taken as 0.005. The isotropic hardening model (MAT024) was used to simulate the constitutive behavior of steel tube. The combined hardening model (MAT003) was utilized for the reinforcement. The predicted results were not sensitive to the hardening parameter (β) in the model, and thus the β was selected as 0.1.

The FE model using constant stress solid element type (ELFORM=1) to simulate the cyclic behavior of both RC and concrete fill in CFST. This choice resulted in the shortest calculation time and acceptable accuracy. The hourglass energy of the prediction in the concrete-encased CFST member was only 2.8% of the internal energy, indicating that hourglass effect can be ignored in the model. However, the hourglass-like element shape was observed in the analysis of RC members. Thus, Flanagan-Belytschko hourglass control was adopted in the simulation of RC columns, and the corresponding hourglass coefficient was set as 0.03.

The bond-slip behavior between the concrete fill and steel tube was reasonably modeled using the cohesive material model in LS-Dyna (MAT138). The key parameters in the tangential direction of the model were calibrated by comparison to test data. The bond stiffness, strength and energy releasing rate in the normal direction were set around zero to simulate the normally separation between concrete core and steel tube. In addition, the bond-slip behavior of reinforcement in RC member was modelled by the available bond-slip expression for bar-concrete interface.

Finally, the accuracy of the recommended FE model was evaluated. The modeling method in this paper predicted the load-displacement curves of RC and concrete-encased CFST columns with the maximum errors of 14.7% and 4.3% in resistance, respectively. The FE models also captured general behavior and failure modes.

2.8. Chapter 2 References

[1] Stephens M T, Lehman D E, Roeder C W. Seismic performance modeling of concrete-filled steel tube bridges: Tools and case study. Eng Struct. 2018;165:88–105.

[2] Bruneau M, Kenarangi H, Murphy T P. Contribution of steel casing to single shaft fundation structural resistance. Report for National Cooperative Highway Research Program. Report Number 872;2018.

[3] Stephens M T, Berg L M, Lehman D E, Roeder C W. Seismic CFST column-to-precast cap beam connections for accelerated bridge construction. ASCE J Struct Eng 2016.

[4] Xu W, Han LH, Li W, Seismic performance of concrete-encased column base for hexagonal concrete-filled steel tube: experimental study, J Constr Steel Res 2016;121: 352–369.

[5] Dong YR, Xu ZD, Zeng K, Cheng Y, Xu C, Seismic behavior and cross-scale refinement model of damage evolution for RC shear walls, Eng Struct 2018;167:13–25.

[6] Demir A, Caglar N, Ozturk H, Sumer Y, Nonlinear finite element study on the improvement of shear capacity in reinforced concrete T-section beams by an alternative diagonal shear reinforcement, Eng Struct 2018;120:158–165.

[7] Ding FX, Yin GA, Jiang LZ, Bai Y, Composite fram of circular CFST column to steel-concrete composite beam under lateral cyclic loading, Thin-Wall Struct 2018;122:137–146.

[8] Han LH, Hou CC, Xu W, Seismic performance of concrete-encased column base for hexagonal concrete-filled steel tube: numerical study, J Constr Steel Res 2018;149:225–238.

[9] Lubliner J, Oliver J, Oller S, Oñate E, A Plastic-Damage Model for Concrete, Int J Solids Struct 1989; 25:299–329.

[10] Lee J, Fenves GL, Plastic-damage model for cyclic loading of concrete structures, J Eng Mech 1998;124(8):892–900.

[11] Murcia-Delso J, Shing PB, Bond-slip model for detailed finite-element analysis of reinforced concrete structures, J Struct Eng 2015;141(4):04014125.

[12] Goto Y, Kumar GP, Kawanishi N, Nonlinear finite-element analysis for hysteretic behavior of thin-walled circular steel columns with in-filled concrete, J Struct Eng 2010;136(11):1413-1422.

[13] Imani R, Post-Earthquake Fire Resistance of Ductile Concrete Filled Double-Skin Tube Columns, PhD thesis, Buffalo, NewYork: University at Buffalo; 2014.

[14] Grassl P, Jirasek M, Damage-plastic model for concrete failure, Int J Solids Struct 2006;43:7166–7196.

[15] Grassl P, Xenos D, Uystrom U, Rempling R, Gylltoft K, CDPM2: A damage-plasticity approch to modeling the failure of concrete, Int J Solids Struct 2013;50:3805–3816.

[16] Murray YD. User Manual for LS-DYNA Concrete Material Model 159, May 2007.

[17] Youssf O, EIGawady MA, Mills JE, Displaement and plastic hinge length of FRP-confined circular reinforced concrete columns, Eng Struct 2015;101:465–476.

[18] Moon JH, Lehman DE, Roeder CW, Lee HE, Evaluation of embeded concrete-filled tube (CFT) column-to-foundation connections, Eng Struct 2013;56:22–35.

[19] Moon J, Lehman DE, Roeder CW, Lee HE, Lee TH, Analytical evaluation of reinforced concrete pier and cast-in-steel-shell pile connecion behavior considering steel-concrete interface, Adv Mater Sci Eng 2016, 2016:4159619.

[20] Wang JJ, Wang W, Qian XD, Progressive collapse simulation of the steel-concrete composite floor system considering ductile fracture of steel, Eng Struct 2019;200:109701.

[21] Cox JV, Herrmann LR, Development of a plasticity bond model for steel reinforcement, Mech Cohesive-Frict Mater 1996;3(2):155–180

[22] Lundgren K, Pull-out tests of steel-encased specimens subjected to reversed cyclic loading, Mater Struct 2000;33(7):450–196.

[23] Lundgren K, Gylltoft K, A model for the bond between concrete and reinforcement, Mag Concr Res;52(1):53–63.

[24] Eligehausen R, Popov EP, Bertero VV, Local bond stress–slip relationships of deformed bars under generalized excitations, UCB/EERC-83/23, Earthquake Engineering Research Center, 1983, University of California, Berkeley, CA.

[25] Lows LN, Moehle JP, Govindjee S, Concrete-steel bond model for used in finite element modeling of reinforced concrete structures. ACI Struct J;101(4):501–511.

[26] Murcia-Delso J, Stavridis A, Shing B. Modeling the bond-slip behavior of confined large-diameter reinforcing bars. III ECCOMAS Thematic Conference on Computational Methods in Structural Dynamics and Earthquake Engineering, Corfu, Greece. 2011. p. 25–28.

[27] Tao Z, Song TY,Uy B, Han LH, Bond behavior in concrete-filled steel tubes, J Constr Steel Res 2016;120:81–93.

[28] Lyu WQ, Han LH, Investigation on bond strength between recycled aggregate concrete (RAC) and steel tube in RAC-filled steel tubes, J Constr Steel Res 2019;155:438–459.

[29] Guan MS, Lai ZC, Xiao Q, Du HB, Zhang K, Bond behavior of concrete-filled steel tube columns using manufactured sand (MS-CFT), Eng Struct 2019;187:199–208.

[30] P.Baltay,A.Gjelsvik,Coefficient of friction for steel on concrete at high normal stress, J Mater Civ Eng 1990;2(1):46–49.

[31] Han LH, Wang WD, Zhao XL, Behavior of steel beam to concrete-filled SHS column frames:Finite element model and verification, Eng Struct 2008;30:1647–1658.

[32] Peng Z, Dai SB, Pi YL, Li DX, Zhang YC, Huang J, Seismic behavior of innovative ring-bar reinforced connections composed of T-shaped CFST columns and RC beams with slabs, Thin-Wall Struct 2018;127:1–16.

[33] Low SS, Moehle JP, Experimental study of reinforced concrete columns subjected to multi-axial cyclic loading, EERC Report 87/14, Earthquake Engineering Research Center, University of California, Berkeley, USA, 1987.

[34] Xiao Y, Martirossyan A, Seismic performance of high-strength concrete columns, J Struct Eng 1998;124(3):241–251.

[35] Lehman D E, Roeder C W. Foundation connections for circular concrete-filled tubes. J Constr Steel Res. 2012;78:212–225.

[36] Liu B, Fan W, Guo W, Chen BS, Liu R, Experimental investigation and improved FE modeling of axially-loaded circular RC columns under lateral impact loading, Eng Struct 2017;152:619–642.

[37] Epackachi S, Whittaker AS, A validated numerical model for predicting the in-plane seismic response of lightly reinforced, low-aspected ratio reinforced concrete shear walls, Eng Struct 2018;168:589–611.

[38] Sinha B P, Gerstle K H, Tulin L G. Stress-strain relations for concrete under cyclic loading. ACI Journal, 1964, 61(2): 195-212.

[39] Gopalaratnam V S, Shah S P. Softening response of plain concrete in direct tension. ACI Journal. 1985, 82(3): 310-323.

[40] Wang, Junjie, Personal Communication 2020.

[41] Malvar LJ, Crawford JE, Wesevich JW, Simons D, A plasticity concrete material model

for DYNA3D, Int J Impact Engng 1997,19:847–873.

[42] Chen W F, Plasticity in Reinforced Concrete, McGraw Hill, New York, 1982.

[43] LSTC. Keyword User's Manual, Volume II. Livermore, CA, USA: Version 11 R11.0.0; 2019.

[44] Broadhouse BJ, Neilson A, Modeling reinforced concrete structures in DYNA3D, Report:DYNA3D user group conference, London, 1987.

[45] Ottosen NS. A failure criterion for concrete. J Eng Mech Divis 1977;103:527–35.

[46] International Federation for Structural Concrete (fib). CEB-FIP model code 2010 (MC2010). Berlin, Germany: Ernst & Sohn; 2013.

[47] Rubin M. A simple, convenient isotropic failure surface. ASCE J Eng Mech 1991;117:348-369.

[48] Belytschko T, Ong JSJ, Liu WK, Kennedy JM, Hourglass control in linear and nonlinear problems, Comput Methods Appl Mech Eng 1984; 43(3):251-276.

[49] LSTC. Keyword User's Manual, Volume I. Livermore, CA, USA: Version 11 R11.0.0; 2019.

[50] LSTC. Theory Manual. Livermore, CA, USA: r10859; 2019.

[51] Nguyen DH, Hong WK, Ko HJ, Kim SK, Finite element model for the interface between steel and concrete of CFST (concrete-filled steel tube), Eng Struct 2019;185:141–158.

[52] Zhang YB, Han LH, Zhou Kan, Yang ST, Mechanical performance of hexagonal multi-cell concrete-filled steel tubular (CFST) stub columns under axial compression, Thin-Wall Struct 2019;134:71–83.

[53] Roeder CW, Cameron B, Brown CB, Composite action in concrete filled tubes. J Struct Eng 1999;125(5):477–484.

CHAPTER 3. PARAMETRIC STUDY

3.1. Introduction

In the seismic design of bridge structures, RC piers are commonly used as ductile, energy dissipating members, and the superstructure and deep foundation components are expected to remain elastic. It is common to connect the pier and piles using a pile cap. With the advent of accelerated construction methods, directly connecting the pier to the pile or drilled shaft is appealing. In addition, although RC piles and drilled shafts are common, used of cased shafts, also termed concrete-filled steel tube (CFST) piles, is becoming more common. CFST piles offer distinct advantages in terms of flexural and shear strength relative to RC piles (Roeder et al. 2010; Lehman et al. 2016). In terms of constructability, CFST piles avoid placement of slender, spindly reinforcing cages. In addition, they may be the appropriate solution for challenging soil conditions as well as sites susceptible to liquefaction or lateral spreading.

To encourage the use of CFST piles and shafts while facilitating construction, a robust, direct connection is needed. An example of this type of connection is shown in Figure 3.1. This connection must satisfy the structural robustness as well as sufficient strength and stiffness, large ductility, damage resistance and efficient construction. This connection is the focus of this research study.

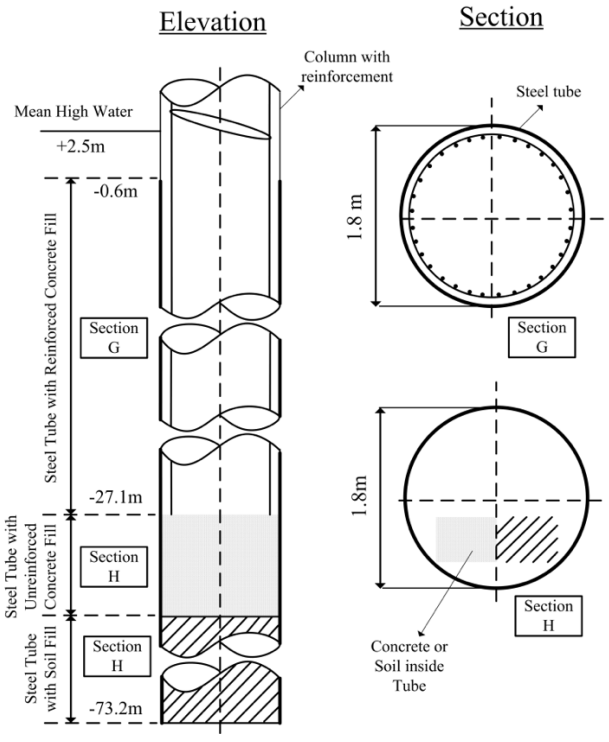

Figure 3.1 Typical configuration RC pier-to-CFST pile connection (courtesy of WSDOT)

Prior research has investigated the response and design of CFST components [e.g., Han et al. 2004, 2010, 2016; Roeder et al. 2009; Lehman et al. 2016; Kowalsky et al. 2012, 2015, 2018; Kenarangi and Brunea 2019]. The experimental work has been extended by conducting parametric studies using experimentally verified, high-resolution FEA [e.g., Kowalsky et al. 2014, Roeder et al. 2012, Lehman et al. 2016, Han 2009, 2018]. This experimental and analytical research has resulted in new design expressions and code equations for axial, flexural, and shear strength of CFST [e.g., Hajjar et al. 1996, Wang et al. 2015, Ding et al. 2011, Lai et al. 2016, Ma et al. 2018, Han 2016, Lehman et al. 2019].

Other research has focused on connections between a CFST components and RC foundations [e.g., Roeder et al. 2012, Stephens et al. 2018, Han et al. 2016, 2018, Pecce et al. 2013, Hitaka et al. 2003, Hsu et al. 2003, Marson et al. 2004], and others have used advanced, high-resolution nonlinear FE model for connections to evaluate monotonic [e.g., Moon et al. 2013, 2016] or cyclic loading behaviors [e.g., Zhu et al. 2017]. This connection modeling experimentally and computationally resulted in new connection design methods.

Although this prior work has significantly advanced the understanding, design and use of CFST components as a structural solution, there are still gaps in design methods. One significant gap is a structurally robust, direct connection between a RC component to a CFST component. This connection is important for bridges and buildings with deep foundations.

Figure 3.2 presents a general schematic of the salient components of a direct RC pier-to-CFST pile or drilled shaft connection. In the figure, d, D, l_R and l_d indicate the diameter of RC pier, the diameter of CFST pile, the location of steel rib inside the pile, and the embedment depth of reinforcement, respectively. The connection must be capable of transferring the full plastic resistance (moment, axial and shear) of the RC component to the composite CFST pile. The pile must distribute the resistance between the steel tube and concrete fill; this requires that the bond stress between the tube and concrete fill is adequate and that the RC reinforcement extends a sufficient length into the CFST pile.

Steel tubes are manufactured by several different methods, and research [Stephens et al. 2016] shows that the method of manufacture has significant effect on the bond stress capacity. Straight welded seam tubes are commonly used and research [Stephens et al. 2016] shows that these tubes has less bond stress capacity than spirally welded tubes, and therefore forces from the reinforcement are unlikely to be effectively transferred to these straight seam steel tube without supplemental mechanical bond or excessively long bar lengths. The steel ribs welded to the interior of tube as shown in Fig. 3.2 is one proposed mechanical bond mechanism.

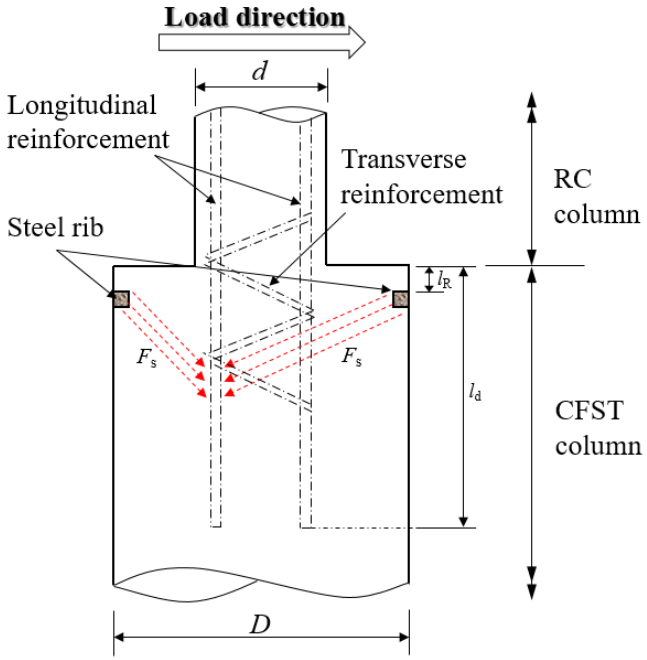

Figure 3.2 Schematic of RC pier-to-CFST pile connection

There are two key design parameters for the rib: 1) the rib size and 2) location of the rib relative to the top of the tube, $l_{R,}$ as shown in Fig. 3.2. The rib provides a reaction point on the tube for the concrete struts originating at the reinforcement and/or the compression region in the RC pier. Determining the size and location of the rib was a primary focus of this research study.

Another important design consideration for the connection is the embedment depth of reinforcement. The AASHTO LRFD design provisions [2010] suggests that the strength of reinforcement can be fully developed if it is embedded to its full development length. However, the bars in the proposed connection have an additional constraint in that the bar also must be embedded for a sufficient length, l_d, to develop composite action and the resulting stress in the steel tube of the CFST, and l_d may depend upon the diameter of the steel tube (D).

A parameter study was undertaken using high-resolution finite element models to better understand the effect of these design requirements. This research utilized the experimentally-validated modeling recommendations for concrete, reinforcing steel, steel tube and bond of RC and CFST components and connections in LS-Dyna presented in Chapter 2.

The proposed connection uses ribs which have not been investigated using experimental or analytical methods. Still, the interface between the steel rib and concrete fill must be properly modeled to meet basic physics. Three method for modeling this interface were investigated. The first used the "AUTOMATIC_SURFACE_TO_SURFACE_TIEBREAK" contact element, which is the approach used for the concrete fill-tube interface [Zhao et al. 2020]. The second approach used shared nodes of rib elements and the concrete elements. The last used the "AUTOMATIC_SURFACE_TO_SURFACE" contact element with the coefficient of friction (COF) of 0.3, which follows the recommendations of Baltay et al. 1990 and Moon et al 2013.

These three contact models of the steel rib and concrete fill interface were compared and evaluated through an initial parameter investigation.

This chapter presents the results of the parametric study. First the analytical model is described. The different approaches for modeling the steel rib are evaluated. The final model is used to investigate the study parameters including: (a) rib size, (b) location of steel rib (the distance from the top of steel tube to the top of rib), (c) reinforcement type, (d) tube diameter (D), (e) the embedment depth of reinforcement (l_d). The results are used to make initial design recommendations. The next phase of the research program will include testing the best configurations based on these recommendation using large-scale experiments.

3.2. Description of Analytical Model: Modeling of Steel Rib

The LS-Dyna finite element (FE) computer program using experimentally validated modeling recommendations for concrete, reinforcing steel, steel tube and bond of RC and CFST components and connections [Zhao et al. 2020] was employed to study the proposed connection. The model considered different concrete constitutive models and included bond-slip between the tube and concrete fill and the reinforcement and the concrete. The reader is referred to the Chapter 2 for addition information on the accuracy and reliability of the modeling approach.

The reference model for the parametric study is illustrated in Figure 3.3. The element type and constitutive model used in each part of the model are given in parenthesis in the figure. The model has three structural components: a RC pier, a CFST pile, and a transfer beam or foundation. The unstudied portion of the model is the rib. This is the focus of this section.

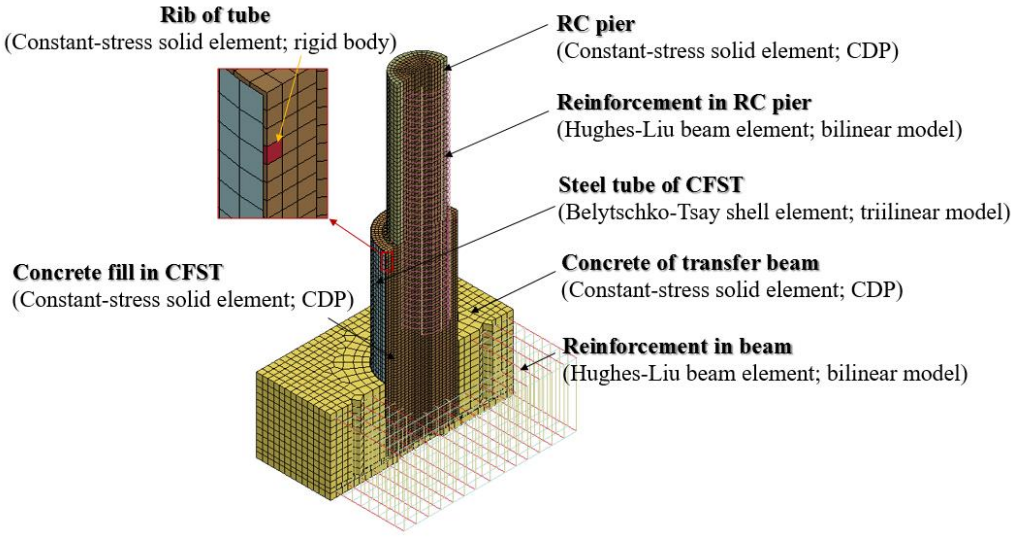

Figure 3.3 FE model of RC pier-to-CFST pile connection

The interface between the rib and the concrete fill was modeled by three different available methods, as noted earlier. The results from the three different models were compared to determine the most accurate method. First the "AUTOMATIC_SURFACE_TO_SURFACE_TIEBREAK" contact was used. This method resulted in element penetration, as shown in Figure 3.4. In the figure, Δ is the lateral displacement at the top of RC column and Δ_y is the displacement at the yield strength of the model, which determined using ATC-24 [ATC 1992]. As such, this contact method was not acceptable to model the rib-concrete interface.

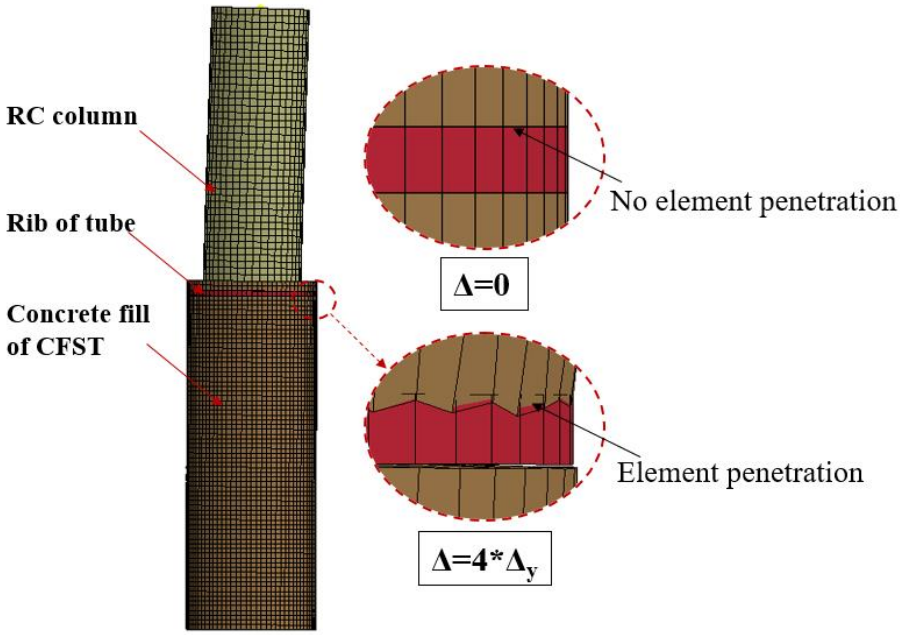

Figure 3.4 Element penetration exhibited for the interface using "AUTOMATIC_SURFACE_TO_SURFACE_TIEBREAK" contact

The second modeling approach investigated was to use shared nodes. This method caused unexpected damage pattern of concrete. To study this, the damage pattern in the middle section for the concrete in RC pier and concrete fill in Fig. 3.5, which shows the contours of the tensile damage parameter (w_t) in CDP model. The tensile damage parameter varied from zero (undamaged) to one (fully damaged). In this chapter, the concrete elements with w_t less than 0.2 were regarded as undamaged (gray sections in Fig. 3.5(b)), the values of w_t between 0.2 and 0.8 indicated moderate damage, and those elements with w_t values higher than 0.8 was significantly damaged (red sections in Fig. 3.5(b)). Significant concrete damage is located above the rib when the displacement is between Δ=1*Δ_y and Δ=4*Δ_y, indicative of unexpected tensile stress above the steel rib. Thus, shared nodes modeling approach is not accurate.

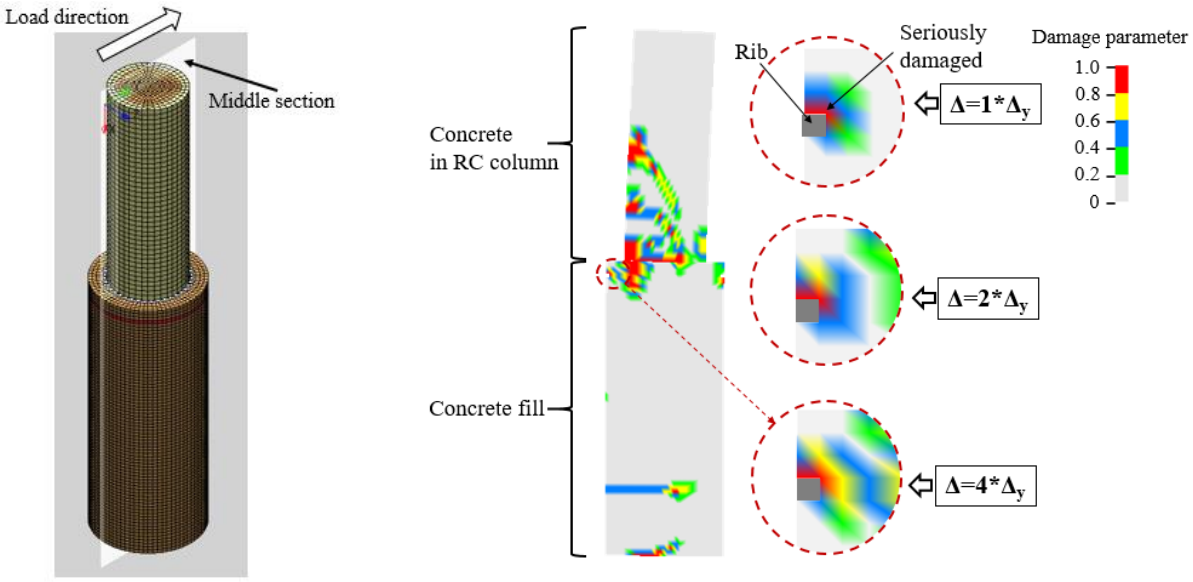

(a) Position of middle section (b) Damage pattern for concrete fill and concrete of RC column

Figure 3.5 Concrete damage pattern for sharing nodes of rib elements with the concrete elements

The third method investigated used the "AUTOMATIC_SURFACE_TO_SURFACE" contact with a coefficient of friction (COF) of 0.3 [Baltay et al. 1990, Moon et al 2013]. This approach is a "two-way treatment contact", which checks all of the nodes on both slave and master surfaces for penetration. Tensile strength in the normal direction was defined as zero for the rib-concrete fill interfaces to allow separation of the rib and concrete. This method both reduced tensile damage above the rib and element penetration (see Figure 3.6), resulting in acceptable estimation of the interface behavior based on the assumed response of this interface and fundamental behavior of concrete and steel. As such, this method was selected for the remainder of the modeling.

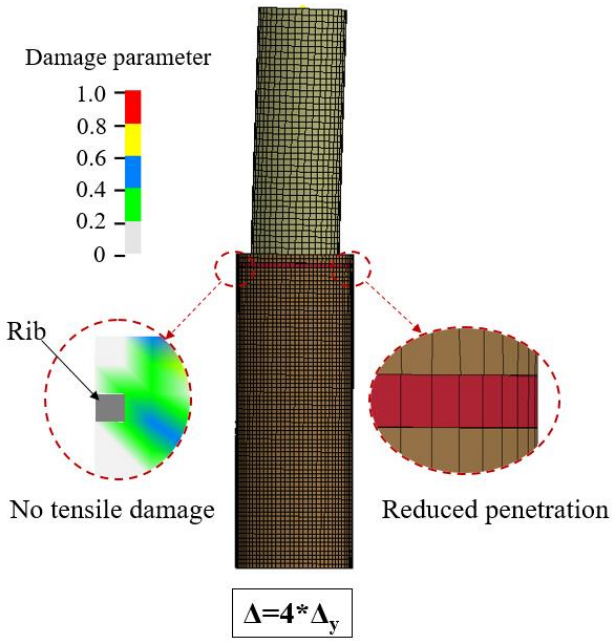

Figure 3.6 Results at concrete-rib interface using "AUTOMATIC_SURFACE_TO_SURFACE" contact

The typical continuum element sizes were 35mm×35 mm for the concrete in RC column and concrete fill, 25 mm×25 mm for the contact area and steel rib, 40 mm×40 mm for the steel tube, 60 mm×60 mm for the concrete of transfer beam. The aspect ratio (h/b) of each element was less than 1.5. With this mesh size, the solution time varied from 15 to 20 hours using the Stampede2 supercomputer at the Texas Advanced Computing Center.

The bottom surface of the transfer beam was fixed in the x, y and z directions. All nodes on the top of RC column were constrained to move together and axial load was applied to the center of the top surface, which was adopted to avoid the stress concentration at the loading point.

3.3. Parametric study

A detailed parametric study was conducted to investigate the nonlinear behavior of RC pier-to-CFST pile or drilled shaft connections shown in Fig. 3.1. The objective of the study was to determine the appropriate embedment depth of reinforcement if supplemental mechanical bond is not included as well the requirements for the rib geometry and location for bars embedded only the required development length. In addition, the simulation results were used to design an experimental study for the next phase of the research. To satisfy both objectives, the model approximated a half-scale bridge pier-pile connection (or a full-scale building column-pile connection) with boundary conditions representative of the laboratory specimen and setup.

To achieve these objectives, a typical geometry for the connection was adopted as shown in Figure 3.7 and Table 3.1 where, the N_0 is the axial load, d is the diameter of RC column, and D is the diameter of the steel tube (pile). The height variables h_{RC}, h_{CFST} and h_{Beam} are the heights of RC column, the CFST pile and the transfer beam, respectively (note the transfer beam is needed

for the testing and therefore simulate here). The embedment depth of the tube into the transfer beam is l_T which was 660.4 mm for the tube diameter of 762 mm and 990.6 mm for the tube diameter of 1219.2 mm. The focus of the analysis and the future experimental research program is the RC pier-to-CFST pile connection. The transfer beam is needed for the experimental research, and its size and depth were chosen to develop the resistance of the connection rather than the resistance of the CFST pile [Lehman and Roeder 2012]. The value of l_T was determined based on the expression proposed by Stephens et al. 2016. The compressive strength of concrete, yield strength of tube and yield strength of reinforcement were kept constant in this study with values of 41.4 MPa, 380 MPa and 413.7 MPa, respectively. The concrete cover for reinforcement is 38.1 mm (1.5 in.). American standard A706 Grade 60 reinforcing steel was used in this simulation.

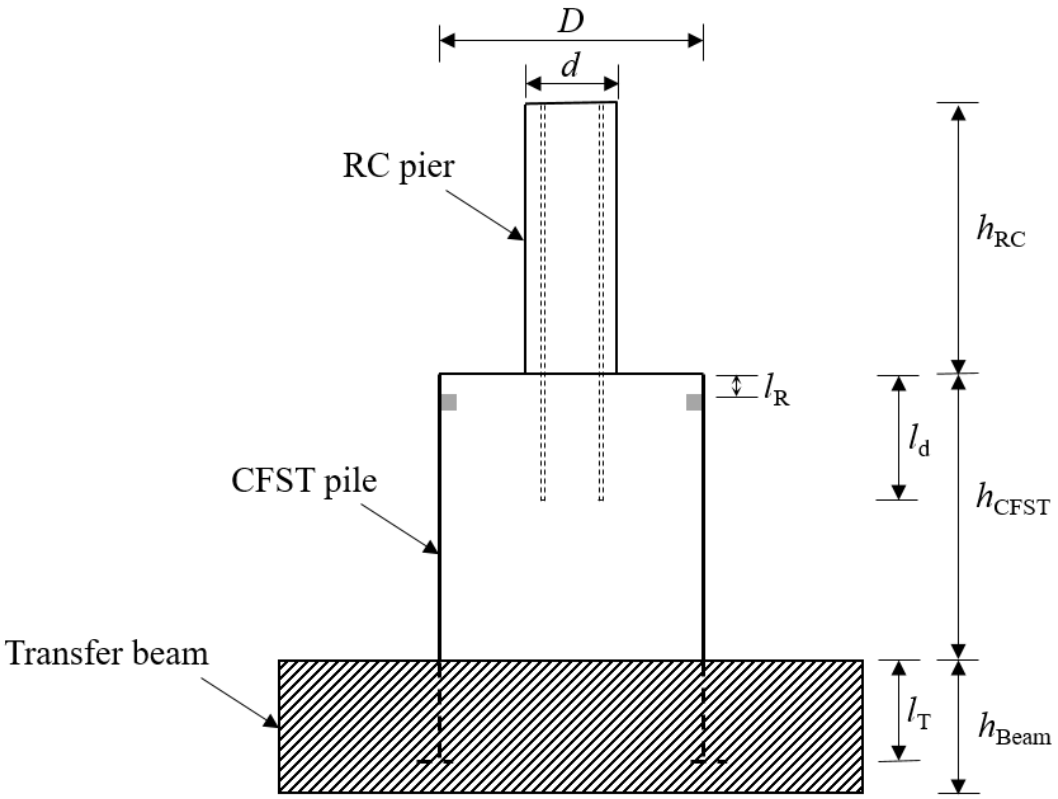

Figure 3.7 Typical connection for parametric study

Table 3.1 Typical dimension of the models in parametric study

N_0 (kN)	d (mm)	Transverse (mm)	D/t	h_{RC} (mm)	h_{CFST} (mm)	h_{Beam} (mm)	l_T (mm)
889.6	508	Spiral #3@50.8	60	1422.4	1168.4	762	660.4 (990.6)

Table 3.2 Simulation matrix in parametric study

Model label	*D* (mm)	Bar size	Embedment depth of reinforcement (mm)	Rib size (mm)	Rib location (mm)
C-30-7-0.5D-NR	762	#7	381 (0.5*D*)[a]	N/A	N/A
C-30-7-0.75D-NR	762	#7	571.5 (0.75*D*)	N/A	N/A
C-30-7-1.0D-NR	762	#7	762 (1.0*D*)	N/A	N/A
C-30-7-1.5D-NR	762	#7	1143 (1.5*D*)	N/A	N/A
C-48-7-0.5D-NR	1219.2	#7	609.6 (0.5*D*)	N/A	N/A
C-48-7-0.75D-NR	1219.2	#7	914.4 (0.75*D*)	N/A	N/A
C-48-7-1.0D-NR	1219.2	#7	1219.2 (1.0*D*)	N/A	N/A
C-48-7-1.5D-NR	1219.2	#7	1828.8 (1.5*D*)	N/A	N/A
C-30-9-1L-NR	762	#9	762 (1*l_{AASHTO})[b]	N/A	N/A
C-30-9-1L-R1-6	762	#9	762 (1*l_{AASHTO})	25.4	152.4
C-30-9-1L-R2-6	762	#9	762 (1*l_{AASHTO})	50.8	152.4
C-30-9-1L-R2-2	762	#9	762 (1*l_{AASHTO})	50.8	50.8
C-30-9-1L-R2-18	762	#9	762 (1*l_{AASHTO})	50.8	457.2
C-30-7-1L-NR	762	#7	533.4 (1*l_{AASHTO})	N/A	N/A
C-30-7-1L- R2-2	762	#7	533.4 (1*l_{AASHTO})	50.8	50.8
C-30-7-1L- R2-6	762	#7	533.4 (1*l_{AASHTO})	50.8	152.4
C-30-7-1L- R2-18	762	#7	533.4 (1*l_{AASHTO})	50.8	457.2
C-48-7-1L-NR	1219.2	#7	533.4 (1*l_{AASHTO})	N/A	N/A
C-48-7-1L- R2-2	1219.2	#7	533.4 (1*l_{AASHTO})	50.8	50.8
C-48-7-1L- R2-2	1219.2	#7	533.4 (1*l_{AASHTO})	50.8	152.4
C-48-7-1L- R2-2	1219.2	#7	533.4 (1*l_{AASHTO})	50.8	457.2

Note: [a] the value in bracket represents that the l_d of the corresponding model is equal to n**D*; where n is 0.5, 0.75, 1 and 1.5;

[b] the value in bracket represents the corresponding l_d is equal to the minimum l_d required in "AASHTO LRFD Bridge Design Specifications" [2010]

The specific study parameters included: (a) absence or use of a rib and rib size, (b) location of steel rib (the distance from the top of steel tube to the top of rib), (c) size of reinforcement , (d) tube diameter (D), (e) the embedment depth of reinforcement. The simulation models are summarized in in Table 3.2. The naming for each model is of form "C-30-9-1L-R1-6", where, 'C' donates RC pier-to-CFST pile connection; '30' is the diameter of tube in inches (30 in.); '9' is the size of reinforcement (# 9); '1L' is the embedment depth of reinforcement normalized to 'l_A', which is the minimum development length in the "AASHTO LRFD Bridge Design Specifications" [2010] represented as l_{AASHTO} in the table; 'R1' is the dimensions of the cross section of the steel rib (R1 indicates 1 in.×1 in.); '6' is the location of steel rib in inches below the top of the tube in inches (6 in.). Table 3.2 shows the details for all analyses included in this study.

The loading history was determined with the consideration of the solution time and the maximum drift ratio in this study as shown in Figure 3.8. The following sections describe the impact of each of the study parameters using the global load-displacement response, with a focus on strength deterioration, equivalent viscous damping factor (ξ_{eq}) as well as the tensile damage parameter (w_t).

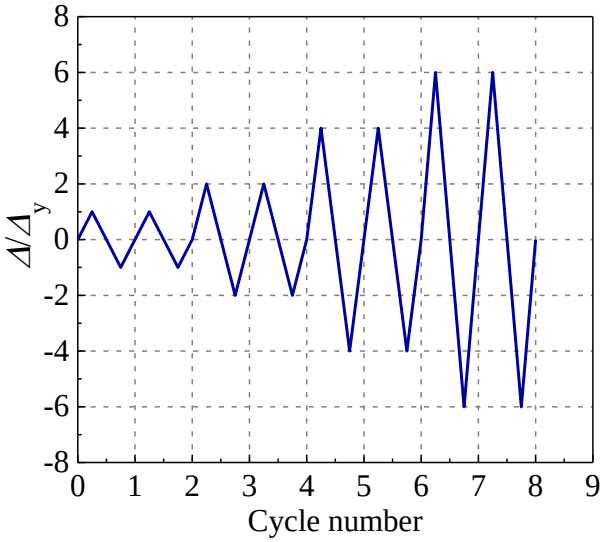

Figure 3.8 Cyclic load history

3.4. Embedment depth of reinforcement as function of tube diameter

The column reinforcement is embedded into the pile for a minimum length equal to the required embedment depth (l_{AASHTO}) required in "AASHTO LRFD Bridge Design Specifications" [2010]. However, the embedment length also needs to be sufficient to transfer the forces to the composite CFST. Without supplemental mechanical bond mechanisms, it is expected that this length may depend on the tube diameter. This is the focus of the first phase of the study.

Figure 3.9 compared the hysteretic curves for models with different tube diameters, where the embedment depth of reinforcement (l_d) is normalized to the tube diameter (D). Two tube

diameters were studied, 762 mm and 1219 mm. For each ratio of l_d/D, the response curves of both tube diameters are shown.

Figure 3.9a shows that an embedment length of 0.5D is not sufficient; there is significant pinching in the response for the smaller diameter tube model and loss of strength for the larger diameter tube. The response is improved for an embedment depth of 0.75D but the strength is not sustained (see Fig. 3.9b). In contrast the hysteretic response is full and the strength is sustained for embedment depths equal to or greater than D.

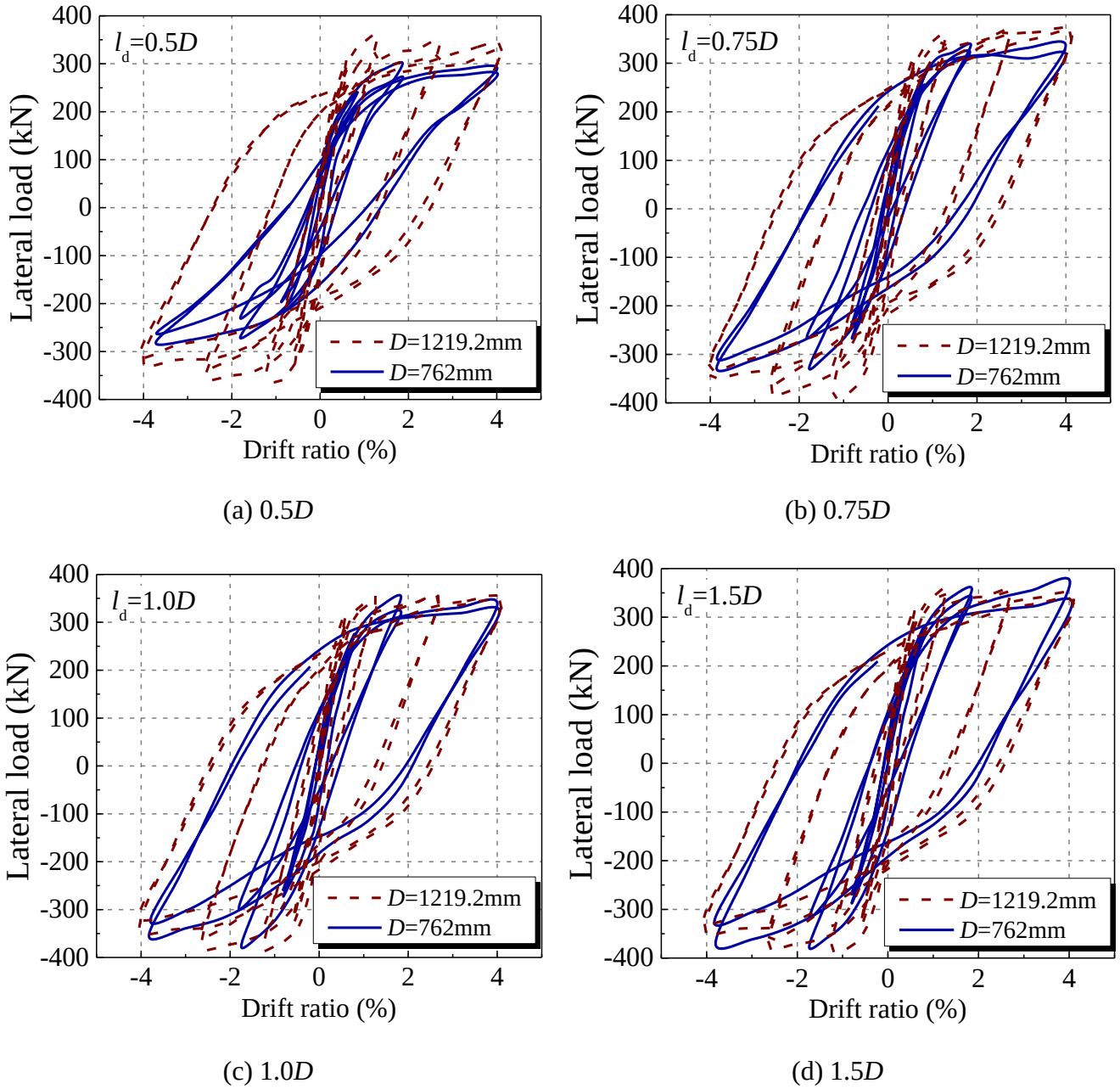

(a) 0.5D (b) 0.75D

(c) 1.0D (d) 1.5D

Figure 3.9 Response curves for models with different embedment depth and tube diameter

Figure 3.10 illustrates the variation in V_{max} with l_d. The two vertical lines on the graph indicate l_{AASHTO} for each tube diameter. For the two models with l_d=0.5D, the strength of the model with D=762mm is 16.0% lower than the larger diameter tube because the embedment depth is less than l_{AASHTO} for D = 76mm. The strength of the models with D = 762 increases as the embedment depth increases with embedment depth. However, l_d did not have significant influence on V_{max} for the model with D of 1219.2mm, with the maximum difference of 3.4%.

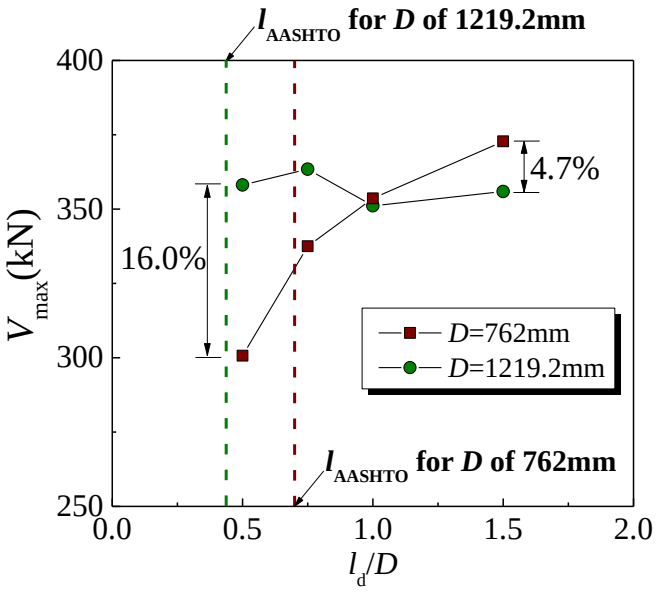

Figure 3.10 Variation of V_{max} with D and l_d

Figure 3.11 compares the equivalent viscous damping factor ξ_{eq} [Blandon et al. 2005, JGJ/T 101-2015] for the different models. A higher ξ_{eq} values normally indicates less pinching and higher energy dissipation capacity. The ξ_{eq} value was calculated using all cycles up to a drift ratio of approximately 4%.

Figure 3.11 shows that the ξ_{eq} for D=762mm was lower than that for D=1219.2mm, for all embedment lengths, when the embedment length is normalized to the tube diameter. Increasing l_d greatly improved the energy dissipation of models with the smaller diameter tube; the energy dissipation was similar for all of the models with the larger diameter tube. For the model with the smaller diameter, the difference between the specimen with l_d=1.0D and l_d=1.5D was only 5.2%. This result is similar to those discussed previously, indicating that a minimum embedment depth of 1D is needed if supplemental bond mechanisms are not provided.

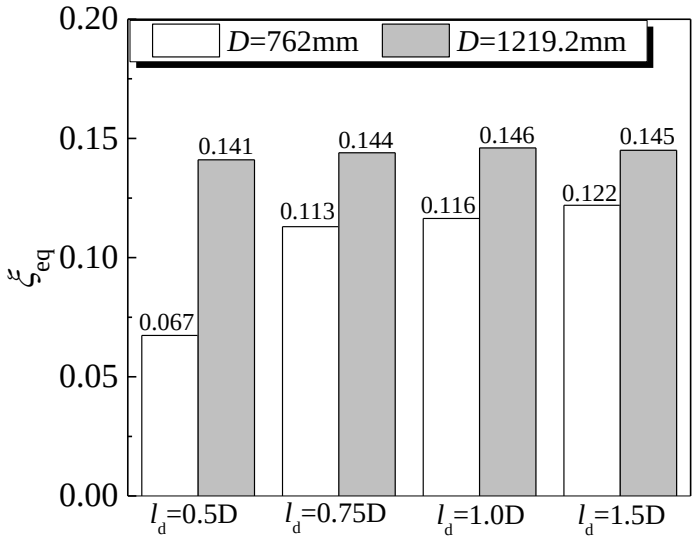

Figure 3.11 Variation of ξ_{eq} with D and l_d

Additional insight into the behavior of the models is provided by investigating the concrete damage using the value of the compressive damage parameter in the CDP model. Figures 3.12 and 3.13 show the concrete damage of the models with different values of D and l_d.

The damage sustained by the concrete of the models with larger diameter was less severe than that for smaller diameter for all embedment depths. This is likely due to the increase concrete area between the bars and the tube which stresses the importance of the ratio of the column to pile diameter. For the models with the smaller tube diameter, the figures show that increasing l_d can significantly reduce the damage of concrete fill for l_d less than or equal to 1.0D.

Overall, the models indicate that l_d should be the greater of 1.0D and l_{AASHTO}. For larger ratios of D_{pile}/D_{col} the concrete damage is reduces even for l_d less than 1.0D; this deserves further study. In addition, because the amount of concrete surrounding the reinforcing bar impacts the response, any offset in the placement of the column cage could also impact the response. Therefore it is recommended that for all configurations the reinforcement is extended into the CFST pile with the maximum of l_{AASHTO} and 1.0D, unless supplemental mechanical bond mechanisms are provided. This issue is studied hereinafter.

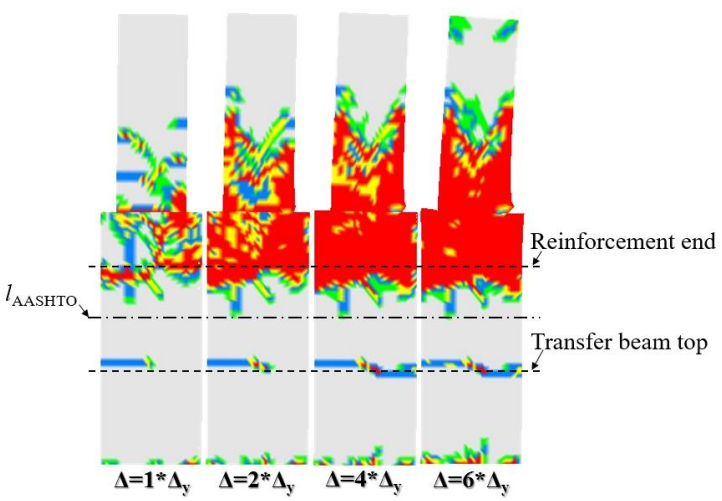

(a) 0.5*D*

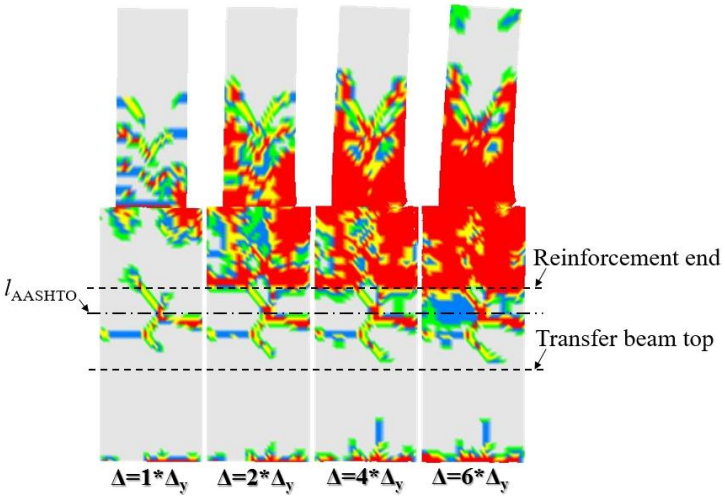

(b) 0.75*D*

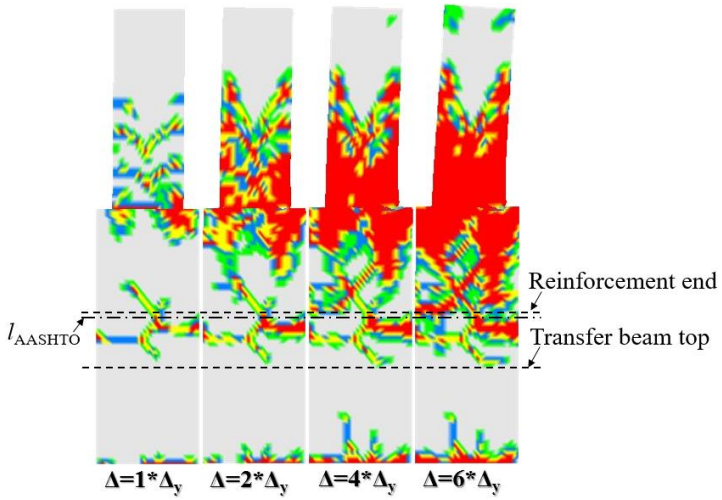

(c) 1.0*D*

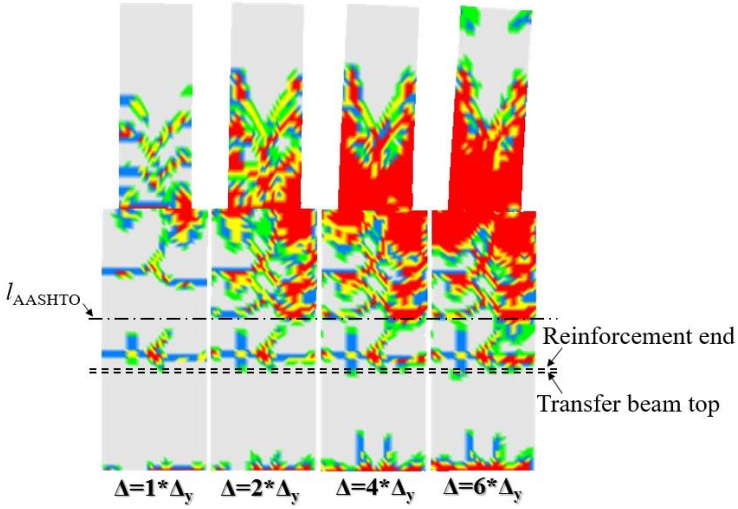

(d) 1.5*D*

Figure 3.12 Concrete damage patterns for the models with different l_d and *D*=762mm

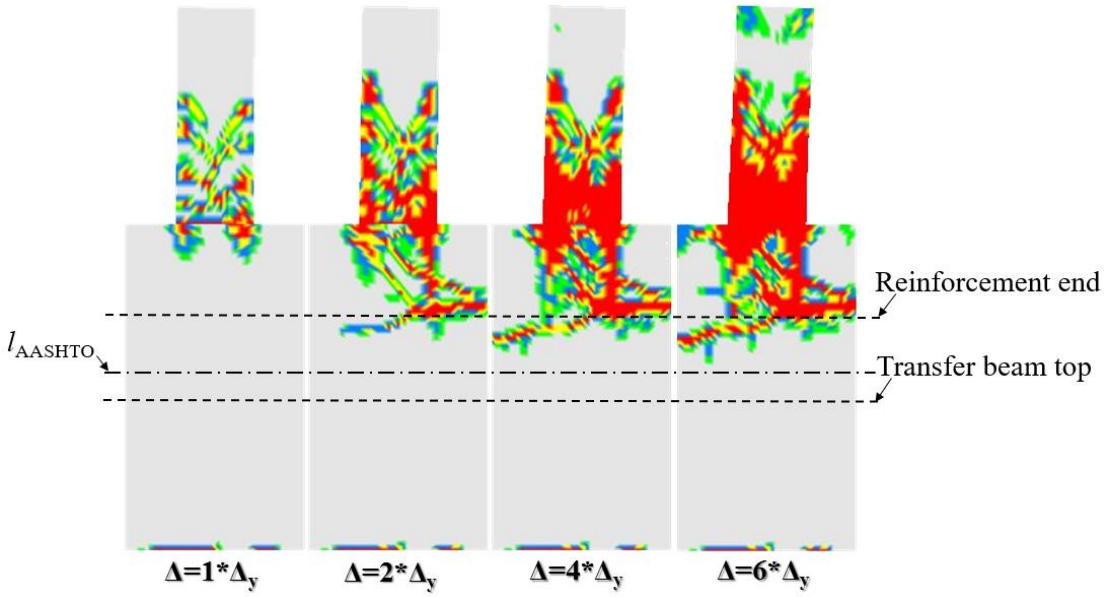
Reinforcement end
l_{AASHTO}
Transfer beam top
Δ=1*Δy
Δ=2*Δy
Δ=4*Δy
Δ=6*Δy

(a) 0.5*D*

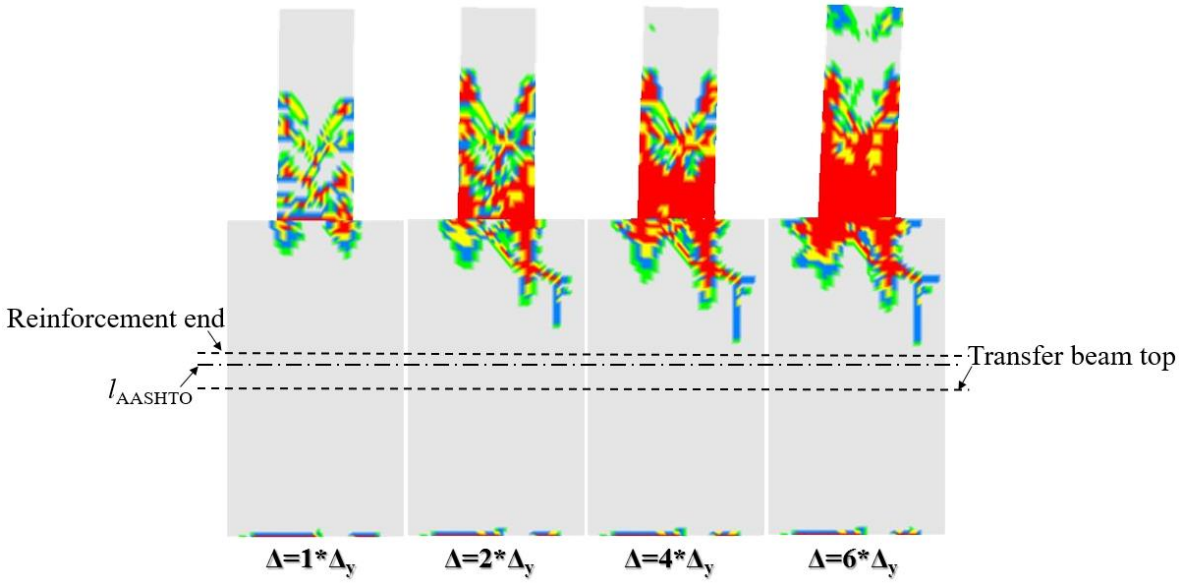
Reinforcement end
l_{AASHTO}
Transfer beam top
Δ=1*Δy
Δ=2*Δy
Δ=4*Δy
Δ=6*Δy

(b) 0.75*D*

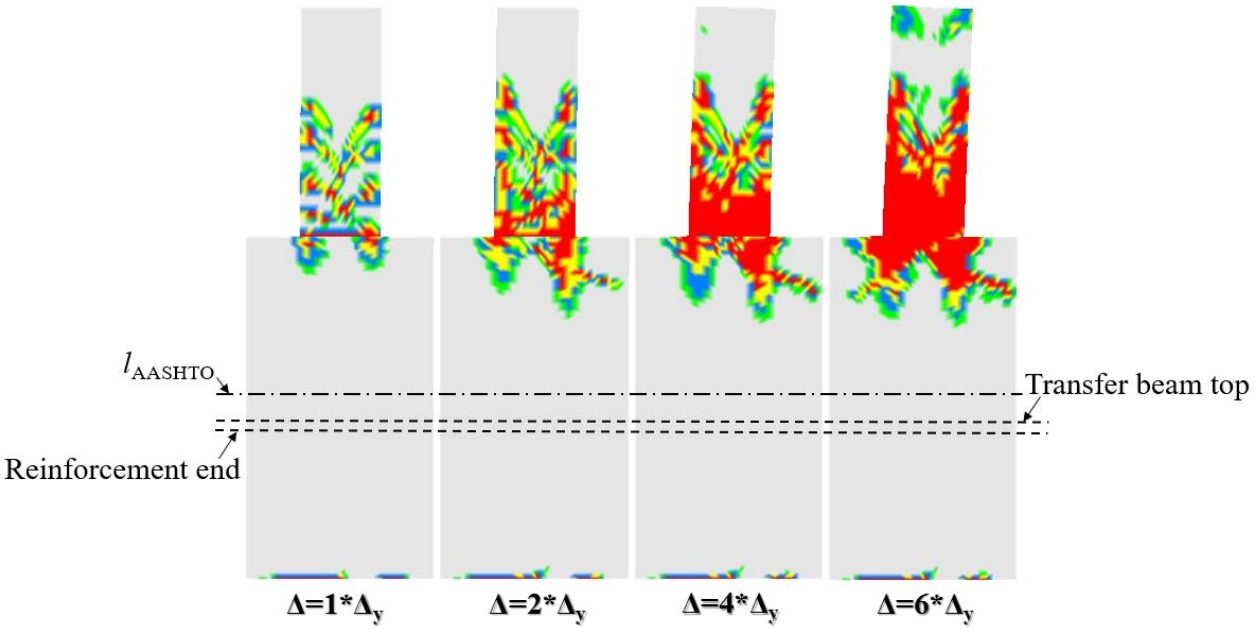

(c) 1.0*D*

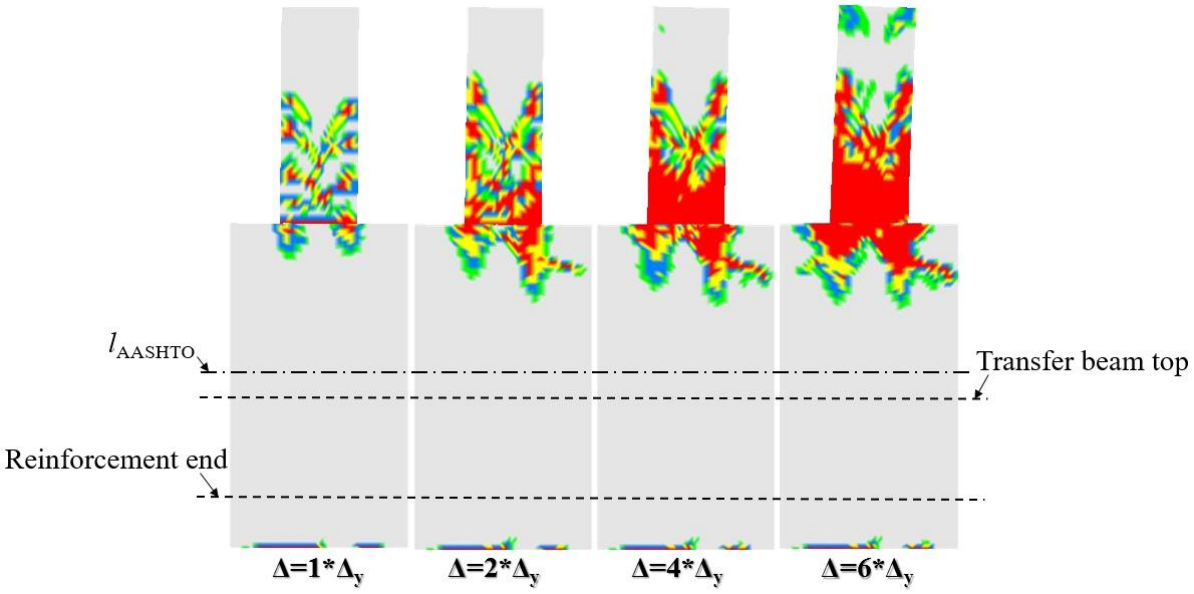

(d) 1.5*D*

Figure 3.13 Concrete damage patterns for the models with different l_d and *D*=1219.2mm

3.5. Rib size

In design practice, there is an interest in supplementing bond with a rib. The remaining parameters studied investigated the rib size and placement. The response of the models with and without ribs are compared in Fig. 3.14. Two different rib sizes were considered: 25.4 mm (1 in.)

and 50.8 mm (2 in.). The models with the rib size of 25.4 mm had the highest strength; the strength was approximately 10% (9.3% and 10.9%) higher than the model without a rib and the models with a 50.8-mm rib.

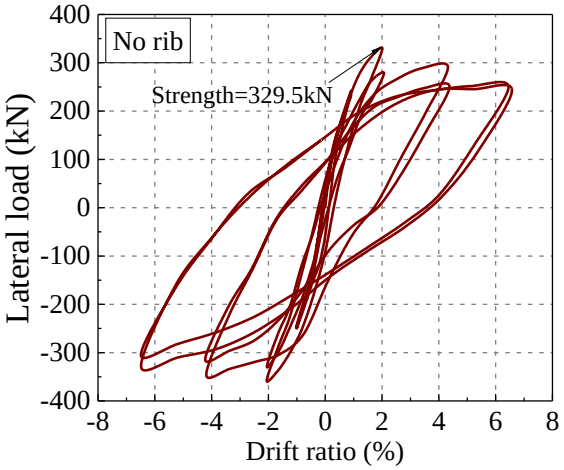

(a) No rib (C-30-9-1L-NR)

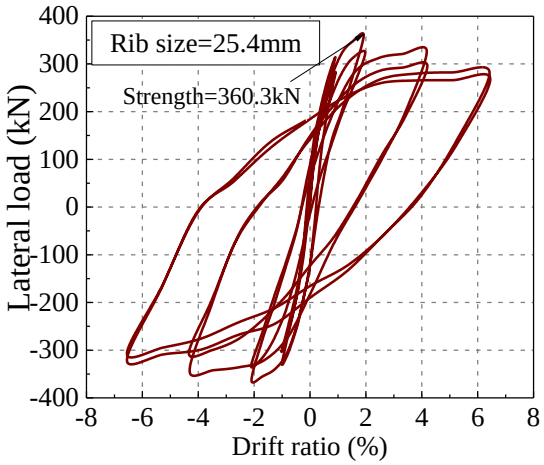

(b) Rib size=25.4mm (C-30-9-1L-R1-6)

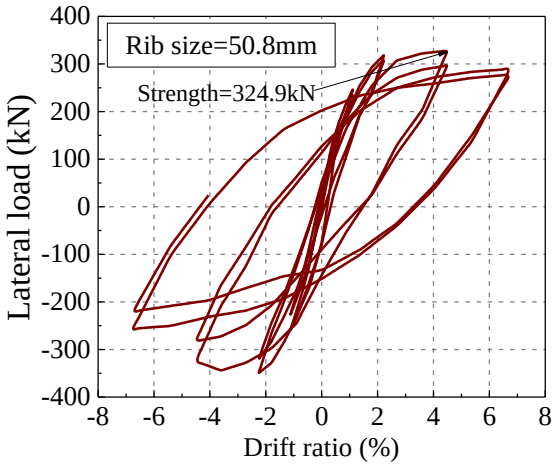

(c) Rib size=50.8mm (C-30-9-1L-R2-6)

Figure 3.14 Cyclic curves for models with different rib size

The amount of strength degradation for each model is compared in Figure 3.15. The strength degradation is calculated using Eq. (3.1).

$$\text{Strength degradation} = \frac{V_{\max} - V_{6\Delta_y}}{V_{\max}} \qquad (3.1)$$

In the expression, V_{max} is the maximum strength of models during the loading history and $V_{6\Delta y}$ is the strength at a lateral displacement of 6*Δ_y. Using a rib size of 50.8 mm resulted in the lowest strength degradation.

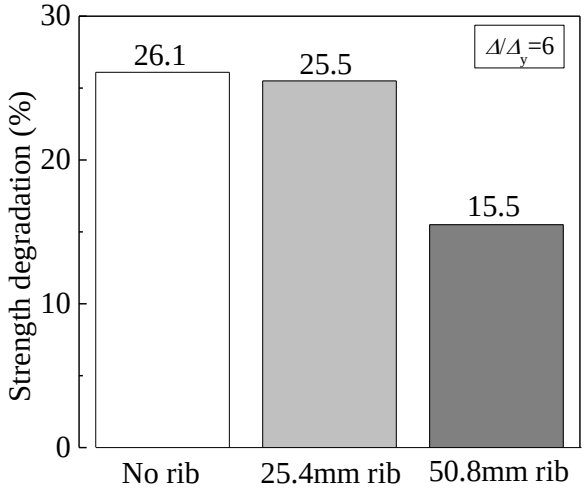

Figure 3.15 Strength degradation for models with different rib size

Figure 3.16 compared the ξ_{eq} values, which was up to the cycle with the drift ratio of approximately 6%. As expected, the model with the rib size of 50.8mm had the highest ξ_{eq} value, which is 22.9% higher than that for the model without rib.

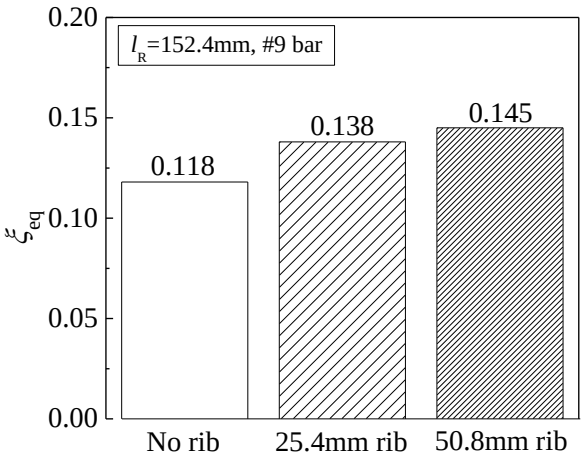

Figure 3.16 Equivalent viscous damping factor (ξ_{eq}) for models with different rib size

Figure 3.17 presents the damage to the concrete fill in the pile and concrete in RC pier with different rib sizes, where the damage of concrete is illustrated by plotting the tensile damage parameter (w_t). In Figure 3.17a, there is extensive damage at the top of the concrete fill in the pile and at the end of the reinforcement. In comparison, there is less concrete damage for the models with rib of 25.4mm and 50.8mm. The rib provides a reaction for the concrete strutting

action originating at the reinforcement and the compression region. These results as well as those above suggest that a rib size of 50.8 mm should be recommended. This rib size was used in the remaining analyses.

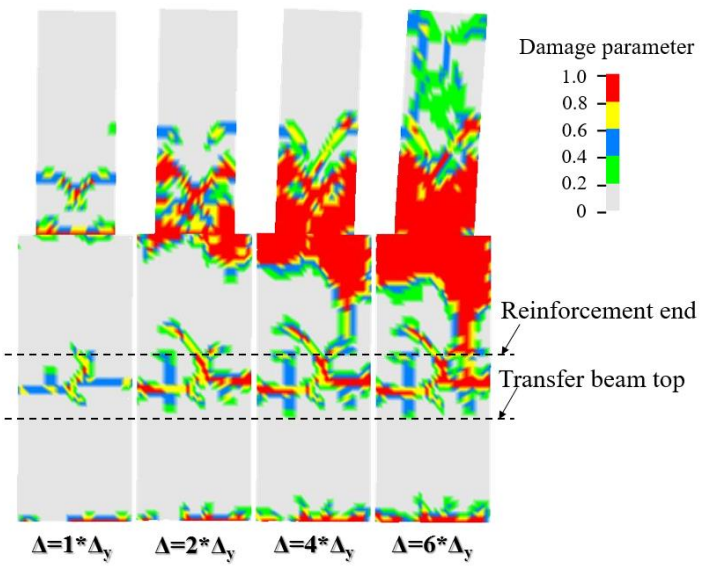

(a) No rib (C-30-9-1L-NR)

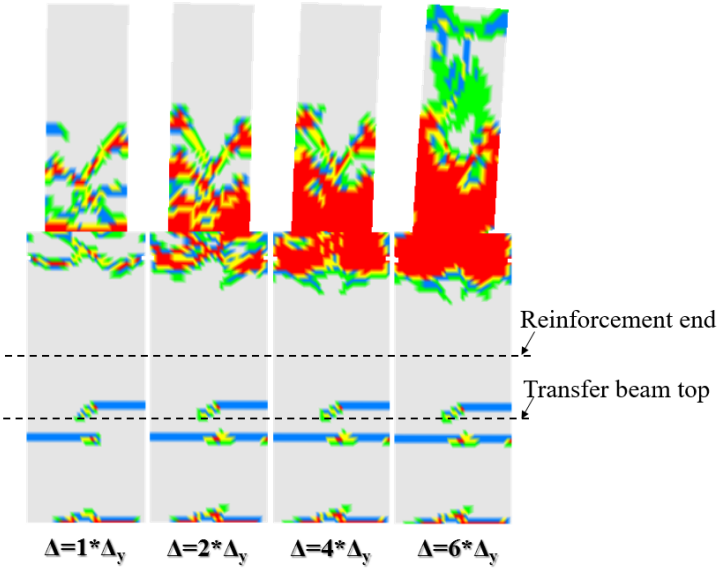

(b) Rib size=25.4mm (C-30-9-1L-R1-6)

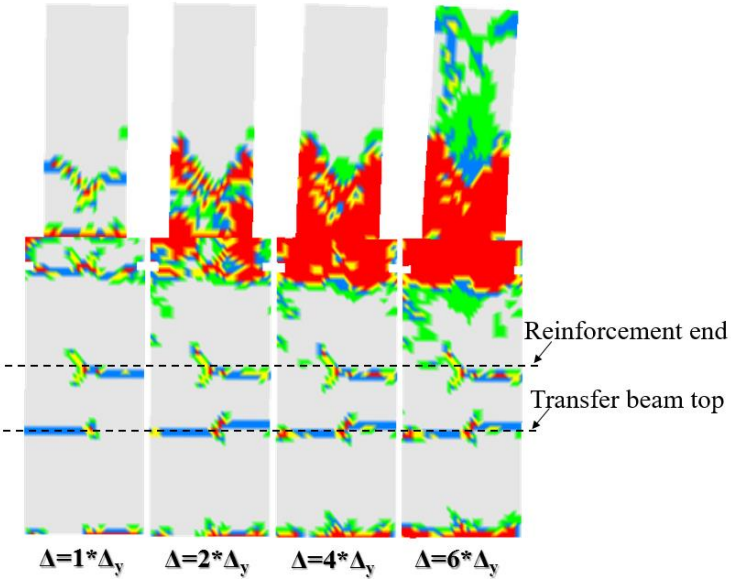

(c) Rib size=50.8mm (C-30-9-1L-R2-6)

Figure 3.17 Comparison of concrete damage pattern for models with different rib size

3.6. Rib location and reinforcement size

The next set of models investigated the placement of the rib relative to the top of the tube. Because the demands on the rib may depend on the size of the reinforcing bar, this was simultaneously studied. The models with larger bars were designed to have the same flexural strength as the models with the smaller bars.

The hysteretic response curves for the models with different rib locations l_R of 50.8 mm, 152.4 mm and 457.2 mm and reinforcing bar sizes of No.7 and No.9 are presented in Figure 3.18. All of the models had similar strengths (324.9 kN–350.8 kN). The models using the No.9 reinforcement sustained more significant strength degradation. It is postulated that the improved response of the models with No.7 reinforcement is attributed to lower local bond demands between the concrete fill and the steel tube in the pile.

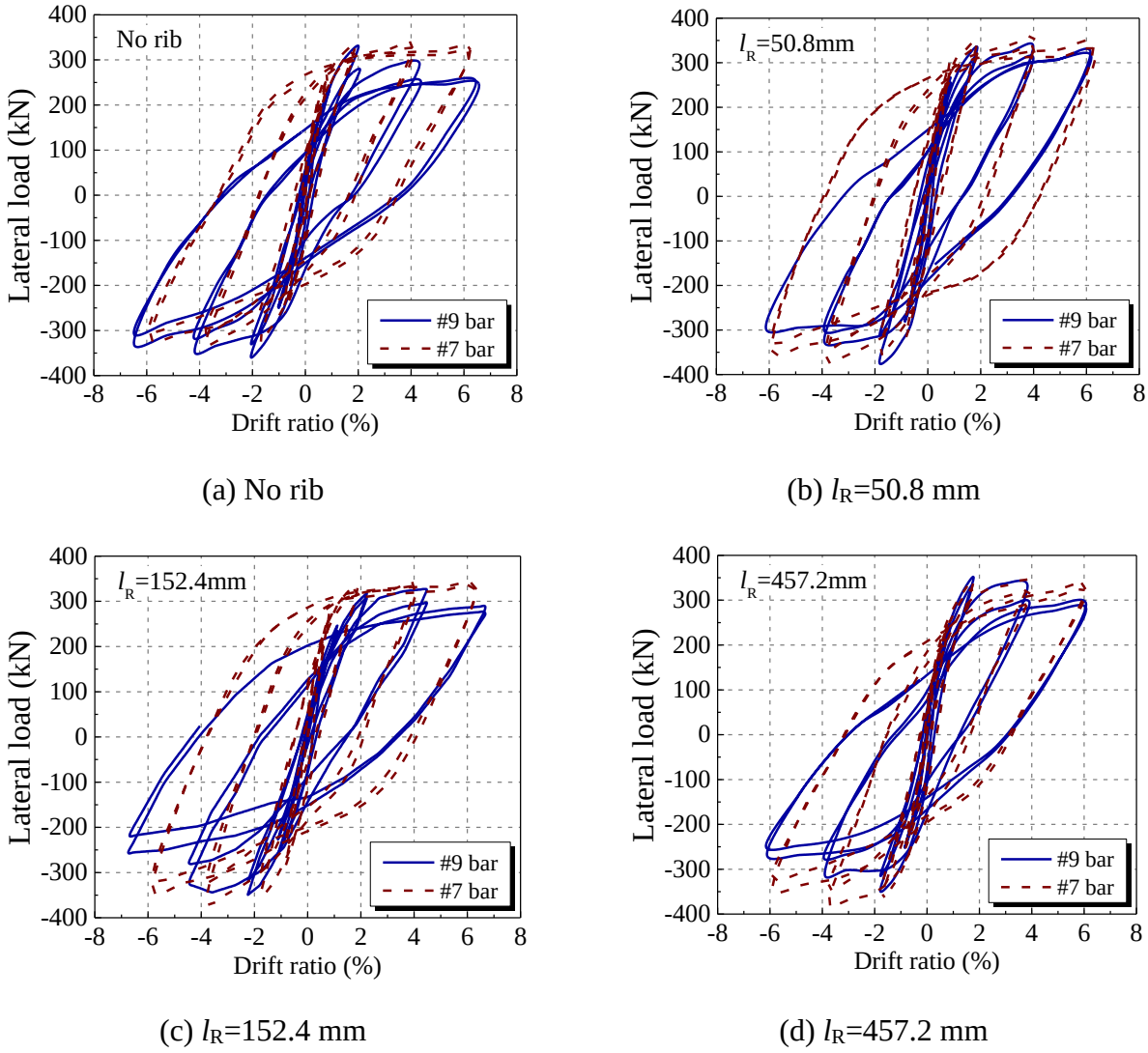

(a) No rib

(b) l_R=50.8 mm

(c) l_R=152.4 mm

(d) l_R=457.2 mm

Figure 3.18 Response curves for models with different rib locations and reinforcing bar sizes

The influence of rib location and reinforcement size on strength degradation are illustrated in Figure 3.19. The steel rib reduces the strength degradation. This influence was more pronounced with the No. 9 reinforcement. The models with the rib located at l_R=50.8mm had acceptable levels of strength degradation for both bar sizes.

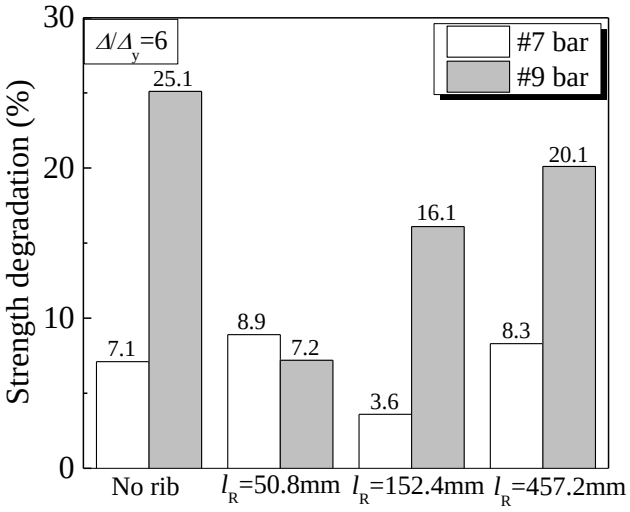

Figure 3.19 Comparison of strength degradation for rib locations and bar size

Fig. 3.20 showed that the results for the models with No. 9 reinforcement generally presented more pinched behavior than the models with No.7 reinforcement. Again, this may also be attributed to the lower bond demand for the No.7 reinforcement, which is included in the bond constitutive model; this reduced local bond demand results in lower concrete damage (note that the embedment depths of the bars are a function of the AASHTO development length, and therefore are not the same value). As such, the energy dissipation is larger for the models with No.7 reinforcement. In addition, ξ_{eq} for a placement of the rib at l_R=50.8 mm was larger as well.

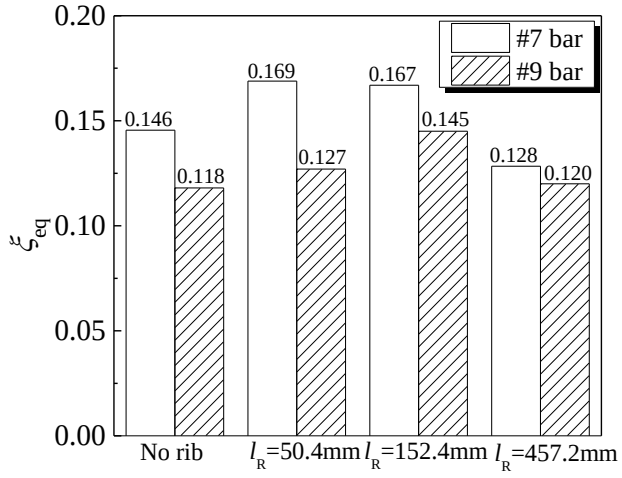

Figure 3.20 Equivalent viscous damping factor (ξ_{eq}) for models with different rib location

The damage patterns of concrete for the models with different rib location and reinforcement types are shown in Figure 3.21. Comparing the results in Figure 3.21 with Figure 3.17a shows that the concrete damage with No. 7 reinforcement is more distributed than the concrete damage for the models with No. 9 reinforcement. This may be the reason there is higher energy dissipation capacity of the model using No.7 reinforcement. Similar to the observations in Fig. 3.17, the inclusion of steel rib decreases the damage to the concrete fill due to the anchoring effect. The models with l_R=50.8mm sustained less damage than that those with l_R=152.4mm and 457.2 mm at lower ductility levels (2 and 4). Taken with the strength degradation data, it is clear there are distinct advantages of placing the rib at 50.8 mm below the top of the tube.

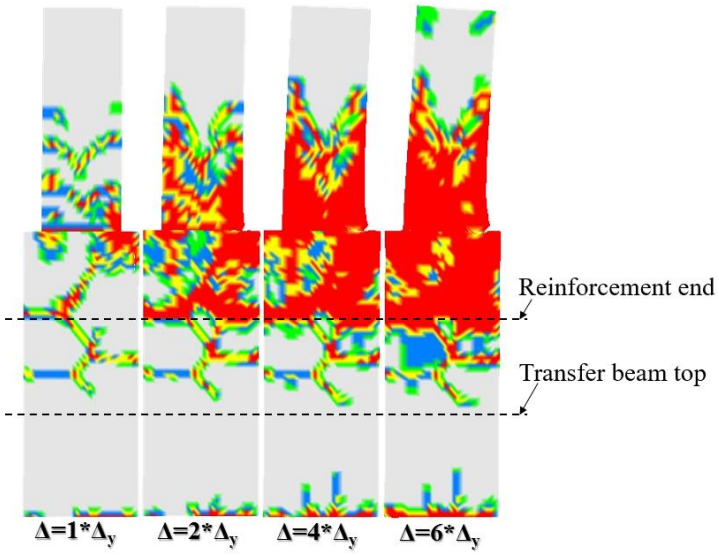

(a) No. 7 reinforcement, no rib

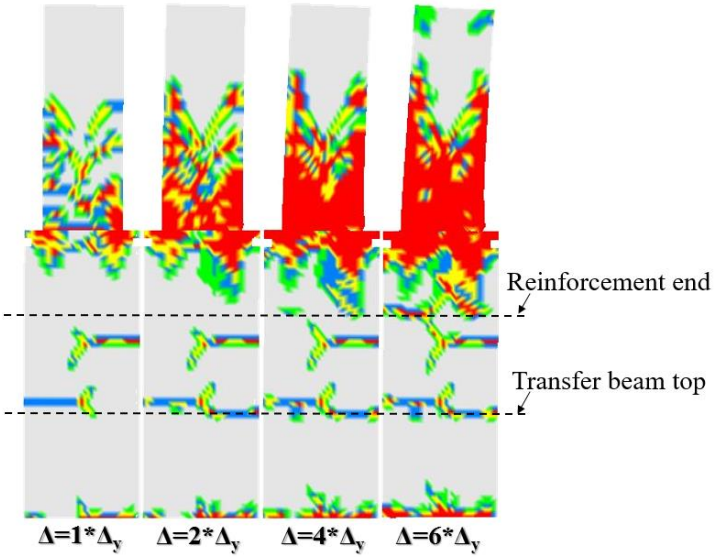

(b) No. 7 reinforcement, l_R=50.8 mm

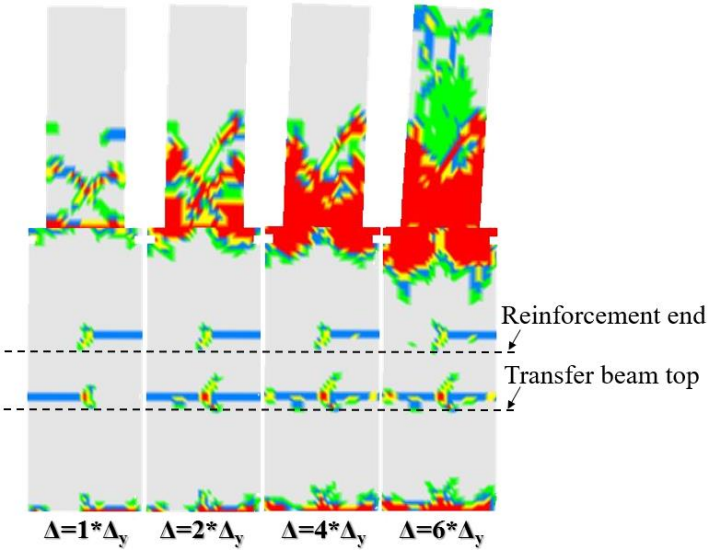

(c) No. 9 reinforcement, l_R=50.8 mm

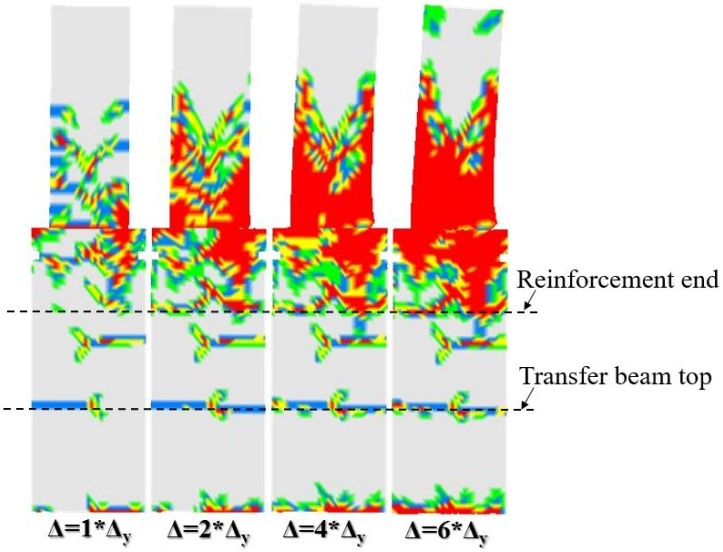

(d) No. 7 reinforcement, l_R=152.4 mm

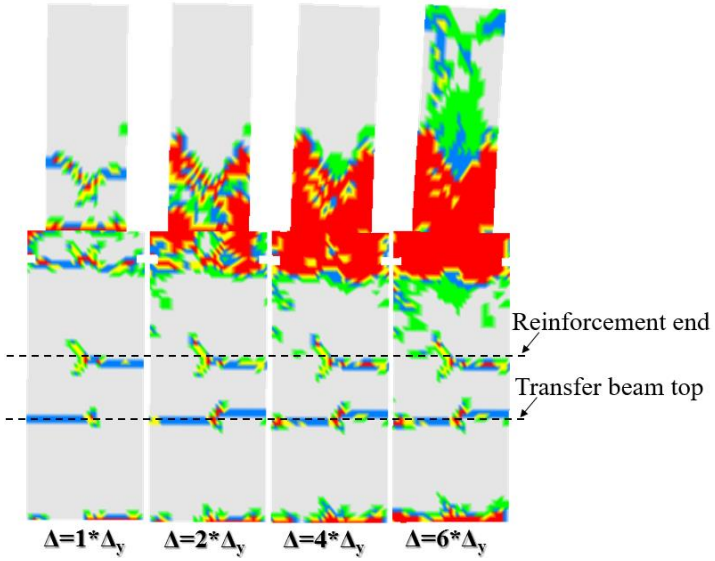

(e) No. 9 reinforcement, l_R=152.4 mm

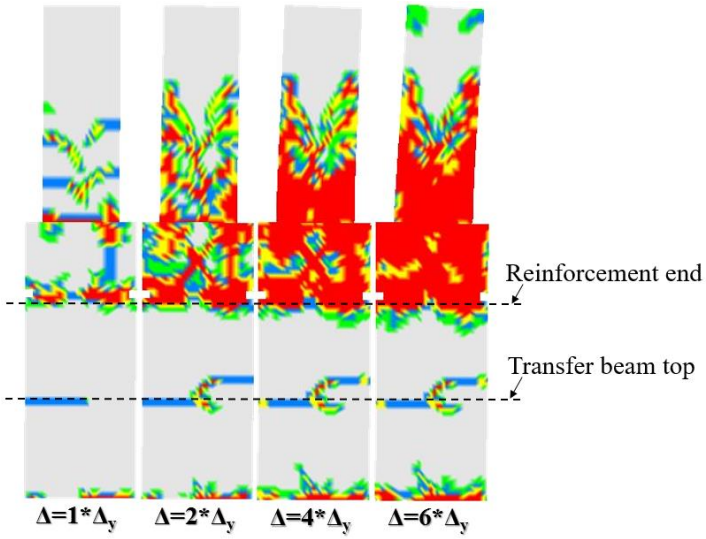

(f) No. 7 reinforcement, l_R=457.2 mm

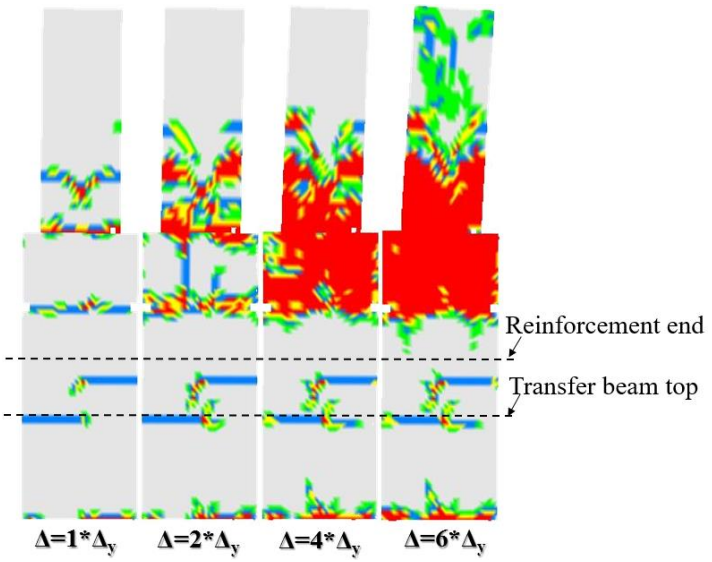

(g) No. 9 reinforcement, l_R=457.2 mm

Figure 3.21 Comparison of concrete damage pattern for models with different rib location and reinforcement type

The anchorage provided by the steel rib is illustrated in Figure 3.22, which illustrates the differences in the minimum principle stress vectors for the models with and without a supplemental rib as well as different location of the rib. In the figure, it is clear that the anchoring effects for the models without rib and with the rib located at l_R=457.2mm are diminished; this is expected because the prior figures indicate that these configurations result in more pronounced damage and strength degradation. Although the response of the models with the rib located at

l_R=50.8mm and l_R=152.4mm are similar, locating the rib l_R=50.8mm provides better restrains and reduces the tensile damage of concrete as shown in Figures 3.21b and c.

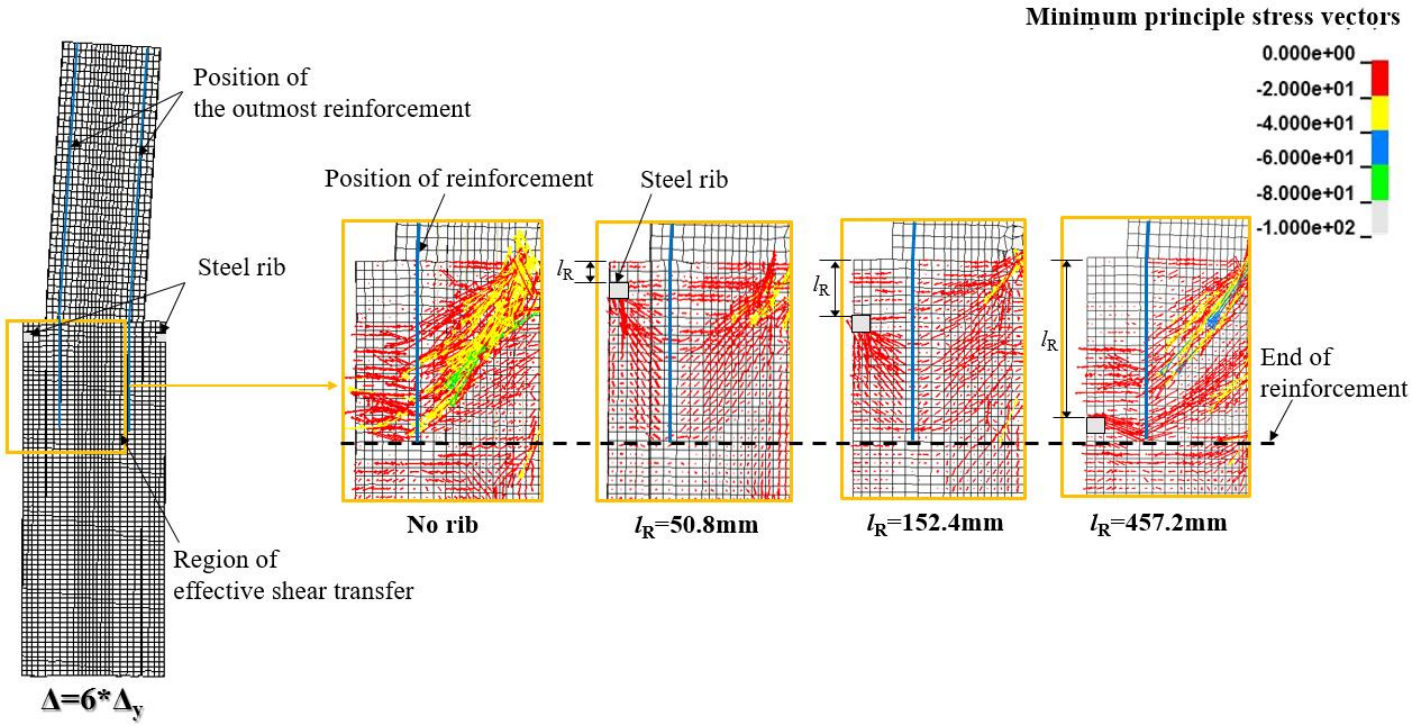

Figure 3.22 Minimum principle stress vectors for models with different rib locations

3.7. Tube diameter

The two different tube diameters were also studied using the supplemental rib. The hysteretic curves are presented in Figure 27 for the pier reinforced with No. 7 bars. As expected, the models had similar strengths of 334.4 kN–368.4 kN because this depends on the reinforcement ratio and placement in the RC pier; the maximum strength difference was 10.2%. The results indicate the fullest response for the models with a rib placed at 50.8mm.

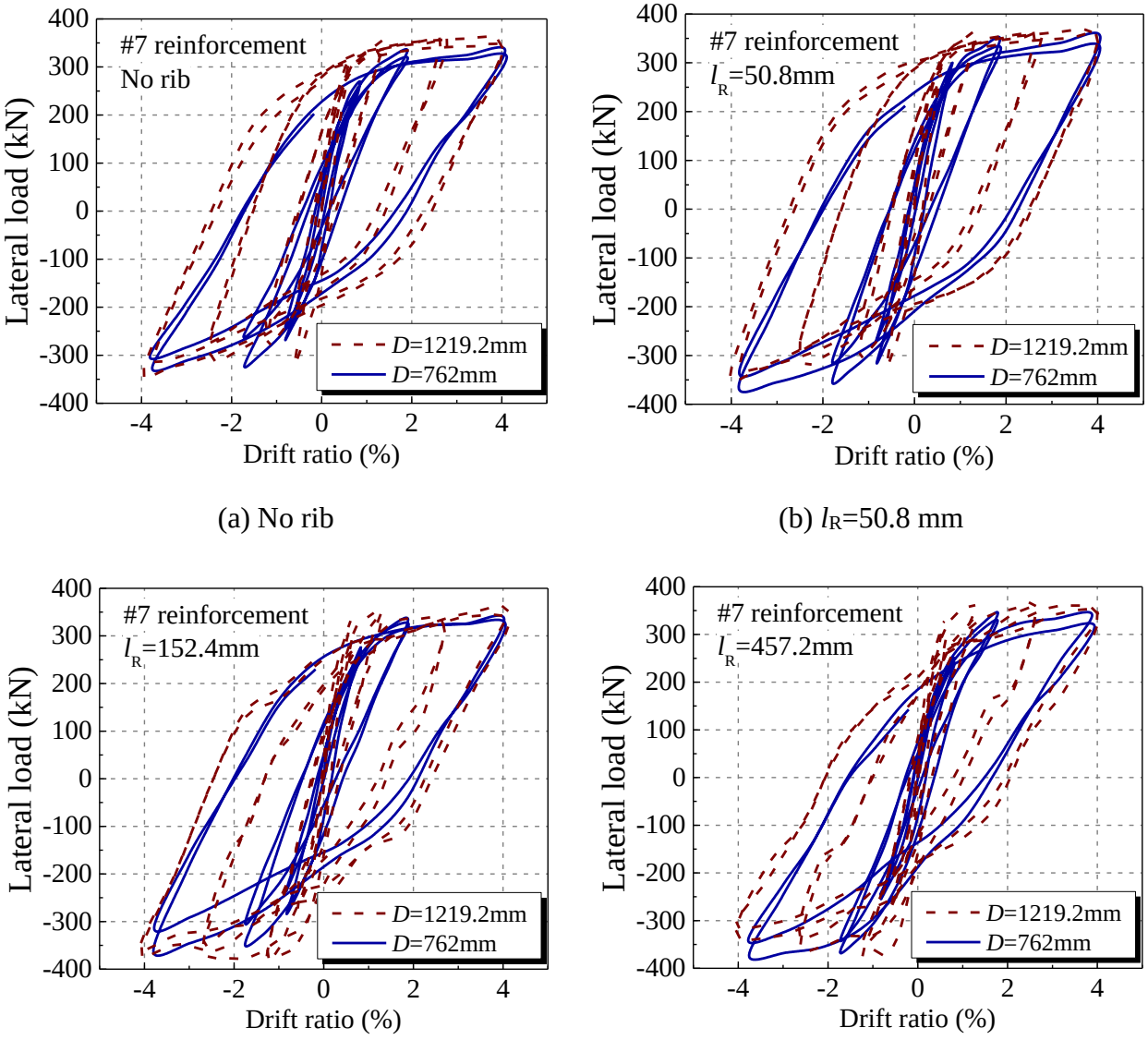

Figure 3.23 Comparison of hysteretic curves for models with different tube diameters and l_R

Figure 3.24 compares the percent of strength degradation at a drift ratio of 4% for the models. The strength degradation of the models with D=1219.2mm was generally lower than those with D=762mm, except for the model with l_R=457.2 mm. Despite of this, all models have the acceptable strength degradation with the maximum value less than 6%.

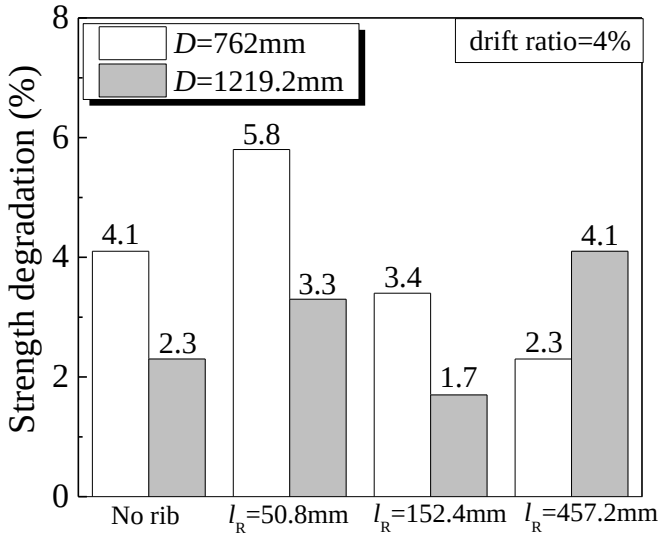

Figure 3.24 Comparison of strength degradation for models with different tube diameters and l_R

Figure 3.25 compares the energy dissipation capacity of models. In all cases it was higher for the larger diameter tube. As expected, the results are similar to Figure 3.24 in that the models with the ribs at 50.8 and 152.4 mm had the highest energy dissipation (and the lowest strength degradation).

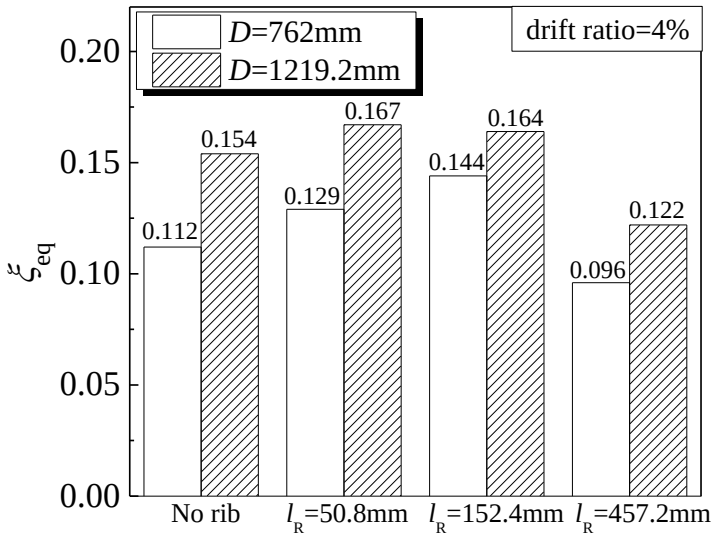

Figure 3.25 Comparison of equivalent viscous damping factor (ξ_{eq}) for models with different tube diameters and l_R

Comparing Figures. 3.21a, b, d, f and Fig. 3.26 clearly demonstrates that increasing the tube diameter reduces the damage to the concrete fill. However, severe concrete damage is sustained in models without a rib (Figure 3.26a). In addition, these models show horizontal cracks at the end of the reinforcement, which might lead to pullout of the reinforcement. The inclusion of steel

rib with l_R=50.8mm reduces this damage and improves the seismic performance of the connection. However, when the l_R increased to 457.2mm, the model exhibits a severe damage pattern, resulting in relative poor seismic behavior, as shown in Figs. 28 and 29. This may be because the anchoring effect of the rib at l_R=457.2 mm is very small (as shown in Fig.26) but the discontinuity in the concrete fill induced by the inclusion of steel rib increases horizontal cracking, leading to more likelihood of reinforcement pullout and more severe damage above the steel rib.

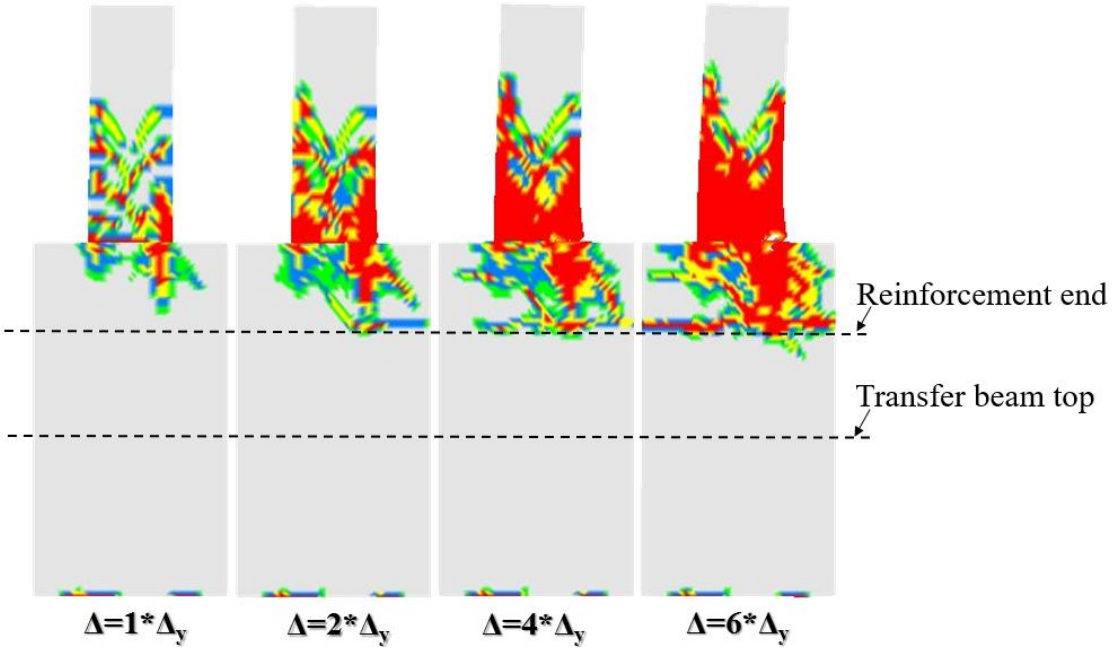

(a) No rib

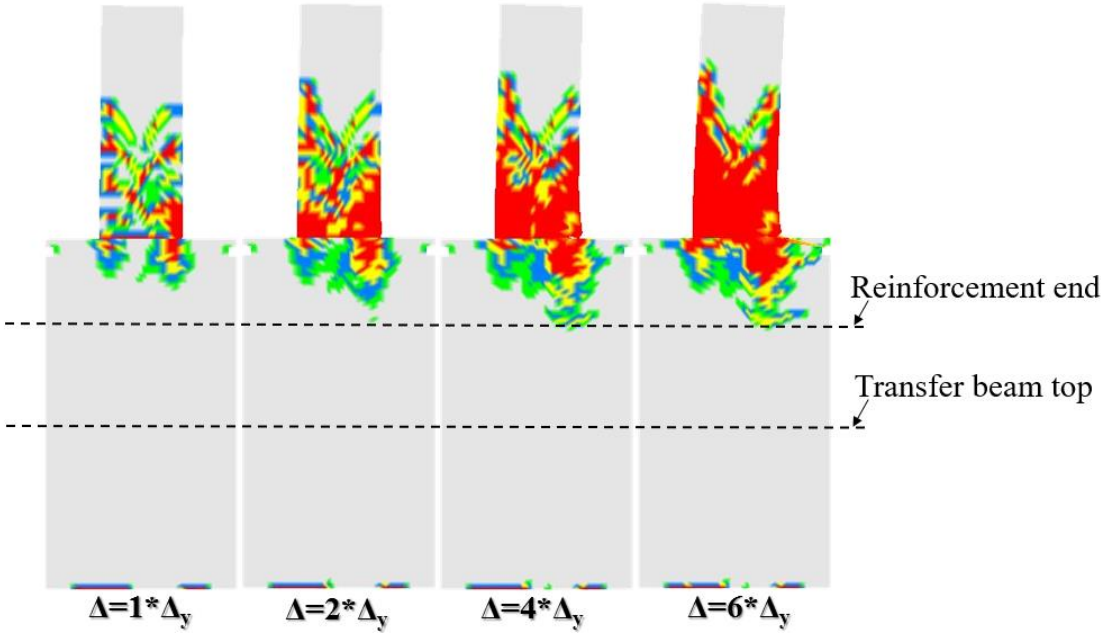

(b) l_R=50.8 mm

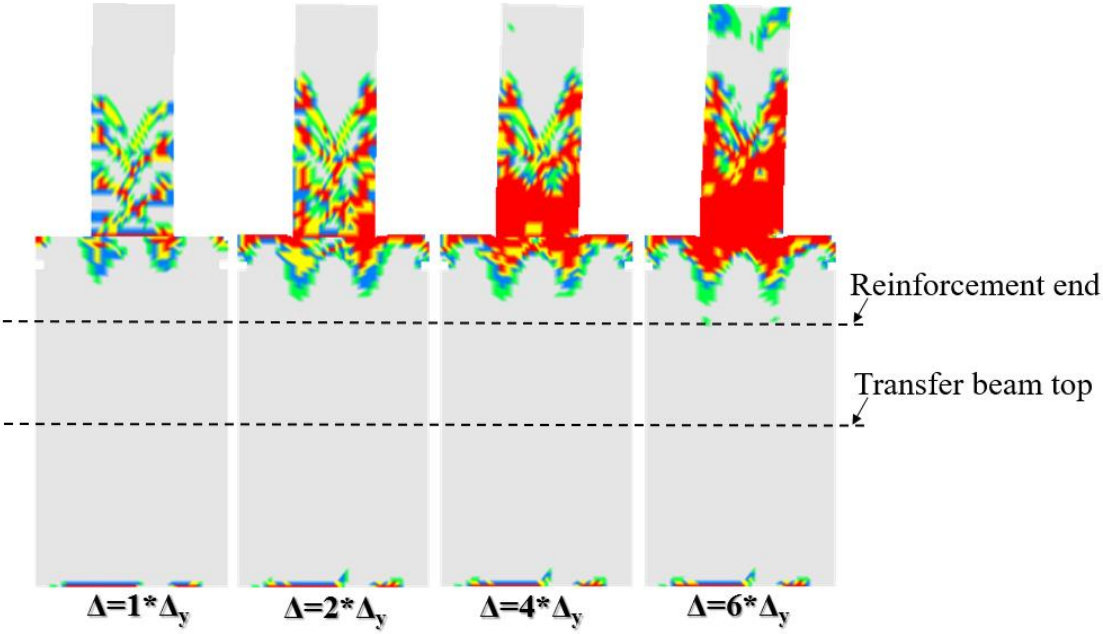

(c) l_R=152.4 mm

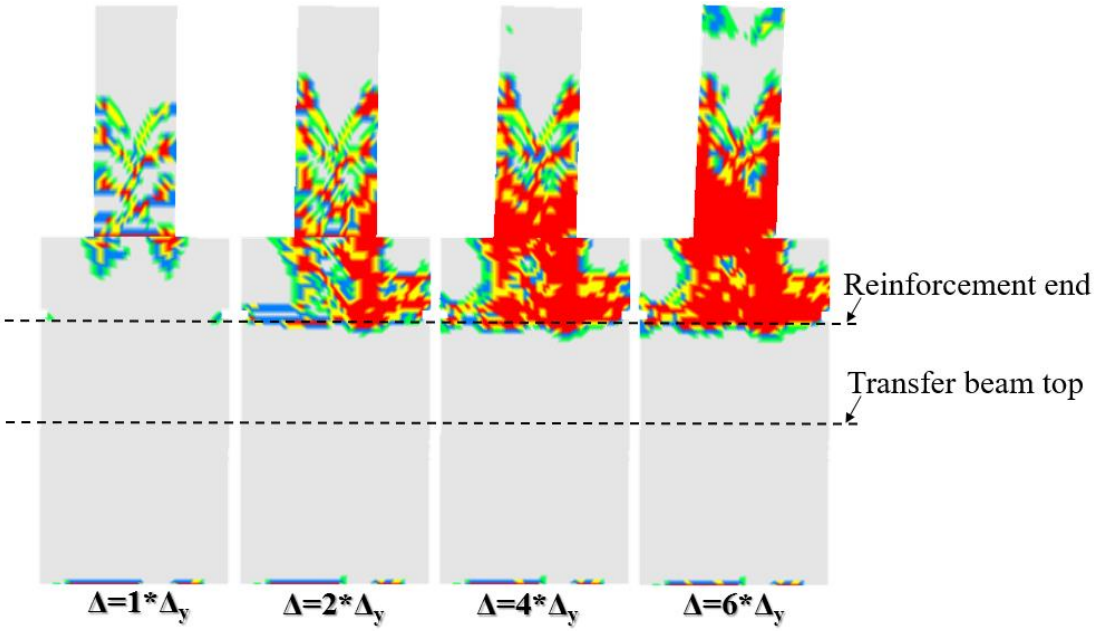

(d) l_R=457.2 mm

Figure 3.26 Concrete damage patterns for models with tube diameter of 1219.2mm

3.8. Chapter 3 References

[1] Stephens M T, Lehman D E, Roeder C W. Seismic performance modeling of concrete-filled steel tube bridges: Tools and case study. Eng Struct. 2018;165:88–105.

[2] Bruneau M, Kenarangi H, Murphy T P. Contribution of steel casing to single shaft fundation structural resistance. Report for National Cooperative Highway Research Program. Report Number 872;2018.

[3] Stephens M T, Berg L M, Lehman D E, Roeder C W. Seismic CFST column-to-precast cap beam connections for accelerated bridge construction. ASCE J Struct Eng 2016.

[4] Lehman D E, Roeder C W. Foundation connections for circular concrete-filled tubes. J Constr Steel Res. 2012;78:212–225.

[5] Moon JH, Lehman DE, Roeder CW, Lee HE, Evaluation of embeded concrete-filled tube (CFT) column-to-foundation connections, Eng Struct 2013;56:22–35.

[6] Moon J, Lehman DE, Roeder CW, Lee HE, Lee TH, Analytical evaluation of reinforced concrete pier and cast-in-steel-shell pile connecion behavior considering steel-concrete interface, Adv Mater Sci Eng 2016, 2016:4159619.

[7] Zhu HQ, Stephens MT, Roeder CW, Lehman DE, Inelastic response prediction of CFST columns and connections subjected to lateral loading, J Constr Steel Res 2017;132:130–140.

[8] American Association of State Highway and Transportation Officials. AASHTO LRFD Bridge Design Specifications. Washington DC, US,2010.

[9] Han LH, Concrete Filled Steel Tubular Structures - Theory and Practice. China: Science Publishing & Media Ltd; 2016 (in Chinese).

[10] Han LH, Flexural behaviour of concrete-filled steel tubes. J Constr Steel Res 2004;60(2):313–337.

[11] L.H. Han, W. Li, Seismic performance of CFST column to steel beam joint with RC slab: experiment. J Constr Steel Res 2010;66(11):1374–1386.

[12] Ding FX, Yu ZW, Bai Y, Gong YZ. Elasto-plastic analysis of circular concrete-filled steel stub columns. J Constr Steel Res 2011;67:1567–1577.

[13] Lai MH, Ho JCM. A theoretical axial stress-strain model for circular concrete-filled-steel-tube columns. Eng Struct 2016;125:124–143.

[14] Ma DY, Han LH, Li W, Zhao XL. Seismic performance of Concrete-encased CFST piers:

analysis. J Bridge Eng 2018;23(1):04017119.

[15] Zhao MZ, Lehman DE, Roeder CW, Modeling recommendation for RC and CFST sections in LS-Dyna including bond slip. Eng Struct 2020. (Under review)

[16] P.Baltay,A.Gjelsvik,Coefficient of friction for steel on concrete at high normal stress, J Mater Civ Eng 1990;2(1):46–49.

[17] LSTC. Keyword User's Manual, Volume I. Livermore, CA, USA: Version 11 R11.0.0; 2019.

[18] Grassl P, Jirasek M, Damage-plastic model for concrete failure, Int J Solids Struct 2006;43:7166–7196.

[19] Grassl P, Xenos D, Uystrom U, Rempling R, Gylltoft K, CDPM2: A damage-plasticity approch to modeling the failure of concrete, Int J Solids Struct 2013;50:3805–3816.

[20] International Federation for Structural Concrete (fib). CEB-FIP model code 2010 (MC2010). Berlin, Germany: Ernst & Sohn; 2013.

[21] British Standards Institution, European Committee for Standardization, BS EN 1992, Eurocode 2: Design of Concrete Structures-Part 1–1: General Rules and Rules for Buildings, BSI standards, London, 2004.

[22] Murcia-Delso J, Stavridis A, Shing B. Modeling the bond-slip behavior of confined large-diameter reinforcing bars. III ECCOMAS Thematic Conference on Computational Methods in Structural Dynamics and Earthquake Engineering, Corfu, Greece. 2011. p. 25–28.

[23] LSTC. Keyword User's Manual, Volume II. Livermore, CA, USA: Version 11 R11.0.0; 2019.

[24] Applied Technology Council (ATC) ATC-24 Guidelines for Testing Steel Components, Applied Technology Council, Redwood City CA, 1992.

[25] Low SS, Moehle JP, Experimental study of reinforced concrete columns subjected to multi-axial cyclic loading, EERC Report 87/14, Earthquake Engineering Research Center, University of California, Berkeley, USA, 1987.

[26] Xiao Y, Martirossyan A, Seismic performance of high-strength concrete columns, J Struct Eng 1998;124(3):241–251.

[27] Xu W, Han LH, Li W, Seismic performance of concrete-encased column base for hexagonal concrete-filled steel tube: experimental study, J Constr Steel Res 2016;121: 352–369.

[28] ASTM A1035 / A1035M-19, Standard Specification for Deformed and Plain, Low-Carbon, Chromium, Steel Bars for Concrete Reinforcement, ASTM International, West Conshohocken, PA, 2019

[29] Acceptance Criteria for Moment Frames Based on Structural Testingand Commentary (ACI

374.1-05), ACI Committee 374, American Concrete Institute, 2005.

[30] Blandon CA, Priestley MJN, Equivalent viscous damping equations for direct displacement based design. J Earthquake Eng 2005;2:257–278.

[31] Specification for seismic test of building (JGJ/T 101-2015), Ministry of Housing and Urban-Rural Development of the People's Republic of China, Beijing, China, China Architecture & Building Press, 2015. (in Chinese)

[32] Washington State Department of Transportation. Bridge Design Manual (LRFD). Washington, US, 2019

[33] Roeder CW, Lehman DE, Thody R, Composite action in CFT components and connections. Eng J 2009;46(4):229–242

[34] Brown NK, Kowalsky MJ, Nau JM, Impact of D/t on seismic behavior of reinforced concrete filled steel tubes. J Constr Steel Res 2015;107:111–123.

[35] Montejo LA, González-Román LA, Kowalsky MJ, Seimic performance evaluation of reinforced concrete-filled steel tube pile/column bridge bents. J Earthq Eng 2012;16(3):401–424.

[36] Aguirre DA, Kowalsky MJ, Nau JM, Gabr M Lucier G, Seismic performance of reinforced concrete filled steel tube drilled shafts with inground plastic hinges. Eng Struct 2018;165:106–119.

[37] Feng YH, Kowalsky MJ, Nau JM, Fiber-based modeling of circular reinforced concrete bridge columns. J Earthq Eng 2014;18(5):714–734.

[38] Han LH, Hou CC, Xu W, Seismic performance of concrete-encased column base for hexagonal concrete-filled steel tube: numerical study, J Constr Steel Res 2018;149:225–238.

[39] Xu W, Han LH, Li W, Seismic performance of concrete-encased column base for hexagonal concrete-filled steel tube: experimental study, J Constr Steel Res 2016;121: 352–369.

[40] Moon JH, Roeder CW, Lehman DE, Lee HE, Analytical modeling of bending of circular concrete-filled steel tubes. Eng Struct 2012;42:349–361.

[41] Lu H, Han LH, Zhao XL, Analytical behaviour of circular concrete-filled thin-walled steel tubes subjected to bending. Thin-Wall Struct 2009;47(3):346–358.

[42] Hajjar JF, Gourley BC. Representation of Concrete-Filled Steel Tube Cross-Section Strength. J Struct Eng 1996:122(11):1327–1336.

[43] L.H. Han, Concrete Filled Steel Tubular Structures - Theory and Practice. China: Science

Publishing & Media Ltd; 2016 (in Chinese)

[44] Lehman DE, Charles CW, Heid A, Yoo JH, Shear response of concrete filled tubes part II: Analytical study. J Constr Steel Res 2019;153:169–178.

[45] Pecce M, Rossi F, The non-linear model of embedded steel-concrete composite column bases. Eng Struct 2013;46:247–263.

[46] Hitaka T, Suita K, Kato M, CFST column base design and practice in Japan. Proc., Int. Workshop on Steel and Concrete Composite Construction (IWSCCC-2003), National Center for Research in Earthquake Engineering, Taipei, Taiwan, 2003.

[47] Hsu H, Lin H, Performance of concrete-filled tube base connections under repeated loading. Proc., Int. Workshop on Steel and Concrete Composite Construction (IWSCCC-2003), National Center for Research in Earthquake Engineering, Taipei, Taiwan, 2003.

[48] Marson J, Bruneau M, Cyclic testing of concrete-filled circular steel bridge piers having encased fixed-base detail. J Bridge Eng 2004;9(1):14–23.

[49] Stephens M T, Berg L M, Lehman D E, Roeder C W. Seismic CFST column-to-precast cap beam connections for accelerated bridge construction. ASCE J Struct Eng 2016.

[50] Stephens MT, Design expression and dynamic evaluation of CFST bridges subjected to seismic hazards, Doctor thesis, Washington, USA: University of Washington; 2016.

CHAPTER 4. CONCLUSIONS AND RECOMMENDATIONS

Direct connection of RC piers/columns to cased (CFST) piles provides economy and is increasingly popular in accelerated bridge construction. However, there are few studies on this connection, especially in high-seismic regions. The research presented here is the first of two-phase study designed to investigate configurations for this connection. The first phase, which was described here, used advanced nonlinear models to conduct a parametric study of the connection. The study parameters included: (a) the effect add a rib and the rib size, (b) location of steel rib (the distance from the top of the steel tube to the top of rib), (c) size of the pier reinforcing bar, (d) tube diameter (D), and (e) the embedment depth of reinforcement (l_d) relative to D. The results of this study are the basis of the second phase of the study, which will use large-scale experimental research methods to investigate the proposed designs.

The modelling method for RC and CFST members developed by the authors was adopted to simulate the nonlinear behavior of the connections. In this study, an accurate modeling approach to simulate the contact between steel rib and concrete fill was also needed. Three approaches were considered: tie-break, shared node, surface to surface. The results showed that the "AUTOMATIC_ SURFACE_ TO_SURFACE" contact with the coefficient of friction (COF) of 0.3 simulated the behavior. The other approaches permitted element penetration or resulted in unexpected tensile stress above the rib and therefore were deemed inaccurate.

The model was used to simulate the inelastic behavior of the connection with a focus on the study parameters. The models were compared based on: (1) strength degradation, (2) energy dissipation capacity to a displacement ductility of 6, and (3) damage to the concrete fill within the CFST component as indicated by the concrete tensile damage parameter. The following summarizes the findings for each study parameter.

Embedment depth as a function of D. A series of analyses were conducted to investigate the relationship of $l_d = \alpha D$ where α ranged from 0.5 to 1.5. The results indicate that without supplemental mechanical bond (i.e., a rib), l_d must be equal to $1.0D$ to maximize strength and energy dissipation as well as to minimize concrete damage.

Rib Size. The addition of a steel rib can greatly improve the structural performance of the connection. Two rib sizes were studied: 25.4 mm and 50.8 mm. The models with a 50.8mm rib had the lowest strength degradation and highest equivalent viscous damping factor (ξ_{eq}) and this size was selected for the remainder of the study.

Size of Pier Longitudinal Reinforcement. Two reinforcing bar sizes were studied. The smaller bar has reduced bond demands and results in less concrete damage, lower strength degradation and higher ξ_{eq} values.

Location of rib. Three different locations of the rib were studied: 50.8, 157.4, and 457.2 mm below the top of the steel tube. The rib is important in resisting the strutting action of the concrete and significant changes in the strength and damage pattern were found if the rib was located at 457.2mm and therefore this distance is not recommended. Mild concrete damage, high energy dissipation capacity and lowest deterioration of strength were measured for l_R=50.8mm. The rib at this location resulted in the largest anchoring region, determined by comparing the minimum principle stress vectors for the models with different rib locations. The rib location could depend on the embedment depth of the reinforcement, however this was not studied.

Diameter of steel tube. Two different diameters of steel tube were studied: 762 mm and 1219.2 mm. The model with higher tube diameter had the general lower strength degradation, higher ξ_{eq} values and reduced damage to the concrete fill.

Based on the numerical analysis results, it is recommended that a 50.8mm rib located at approximately 50.8mm below the top edge of the tube be utilized for this connection and that the reinforcement be embedded to meet the straight-bar development length in AASHTO. The next phase of the research (Cycle 3 project) will experimentally investigate these parameters.